Soft Matter and Biological Physics

Raymond E. Goldstein and Ulrich F. Keyser

Experimental and Theoretical Physics
Part III
Michaelmas 2013

Notes version: v1.00
Release name: see above

Preface

How to use these lecture notes:

Where derivations are written out extensively here, they will probably not be reproduced in class, and vice versa. You will be expected to have understood all of these, and to be able to reproduce these results and variations that use the same methods. Derivations obtained in the exercises on the examples sheets are also part of the course, and worked-out solutions will be made available towards the end of the term.

Dos:

- Use the handout to follow progress through the course material. The structure of the handout is almost the same as the lectures.
- Integrate the lecture overheads and the handout material yourself. There is examinable material that only appears in one place.
- Follow suggestions and think about the questions in the notes. These are distributed through the text to help you spot if you are understanding the material.

Don'ts:

- Expect to study only from these notes. You will need the other primary references. Most of all you will need to understand how to use the material and methods presented, rather than memorising information.
- Expect these notes to be error free. They will contain a higher density of errors than a typical book! (They derive originally from one student's very generous but incomplete work). e-mail us if you think something is wrong or unclear, and the notes will improve.
- Expect these notes to be even in the level of presentation. Some paragraphs are minimal, and some section labels are only place holders for material that will be covered in class. Instead, use these notes to guide you through the books, articles, etc.

Contents

Introduction

1

Soft matter and biological physics are topics very much unlike the more standard subjects such as quantum mechanics or thermal and statistical physics. The latter are in many respects complete, certainly at the level of interest to advanced undergraduate or beginning graduate students. It is safe to say that the core material in these subjects will not change fundamentally in the next decades, if ever. In contrast, soft matter and biological physics are topics which only in the last two decades have become a strong focus in physics departments around the globe. This makes them exciting fields in which to work, but also poses the problem for students and professors in that there is no single standard textbook that covers the field. Thus we have decided to provide some notes in this form, not to replace a textbook, but to help in accessing the material of the course.

These are notes for the Part III 'soft and biological physics' course jointly convened between the Cavendish Laboratory and the Department of Applied Mathematics and Theoretical Physics. They are and will likely remain 'preliminary'. They are neither fully complete, nor fully correct and will be constantly updated. It is very important that you look at other material as well to understand fully the topics covered in the course. It is also important to realize that notes like these can almost never replace a proper textbook. Even more so in an advanced courses replace covering 'hot' topics discussed at the moment in the scientific community it is often necessary to read (very often recent) journal articles. We know that this can be a challenge but you are expected to be able to do this when you start to work on your Part III projects and essays.

Microscopic Physics

2

2.1 Review of molecular physics

The ideal gas law,

$$pV = Nk_BT = nRT \qquad \text{or} \qquad \frac{p}{k_BT} = \rho \ ,$$

where p is the pressure, V is the volume, N is the number of molecules, k_B is the Boltzmann constant, T is the absolute temperature, n is the number of moles, $R = N_A k_B$ is the ideal gas constant (where N_A is Avogadro's number), and $\rho = N/V$ is the density, is only an approximation. At low densities real gases are described by a "virial expansion", a power series in ρ,

$$\frac{p}{k_BT} \simeq \rho + B_2(T)\rho^2 + B_3(T)\rho^3 + \cdots \ .$$

Intuitively, the quadratic term involves 2-body interactions, the cubic term captures 3-body effects, and so on. Experimental measurements (see figure below) of the second virial coefficient B_2 show that it is negative at low temperatures (indicating attraction between pairs) and becomes positive (repulsive) at high temperatures. The temperature T_B at which $B_2 = 0$ is known as the Boyle point.

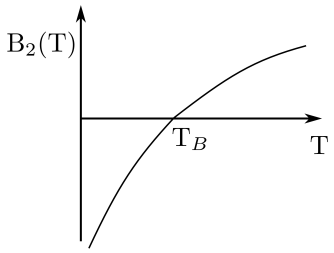

One of the great early triumphs of statistical physics was to show how $B_2(T)$ arises from the underlying intermolecular potential, which typically has a repulsive hard core and an attractive tail due to van der Waals interactions (figure).

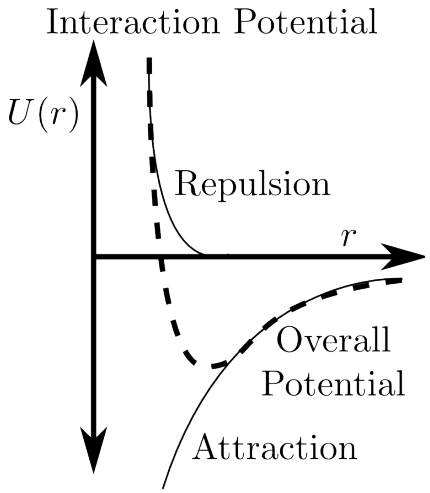

It was van der Waals who had the crucial idea that the potential could be thought of as the sum of a purely repulsive part, which led to excluded volume around each molecule, and a purely attractive part whose effects on the thermodynamics could be estimated by a kind of perturbation theory. In this "mean field" calculation of the latter, we imagine that the density of the gas is uniform throughout space, rather than trying to address the complex form of the radial distribution function (RDF) seen in the figure:

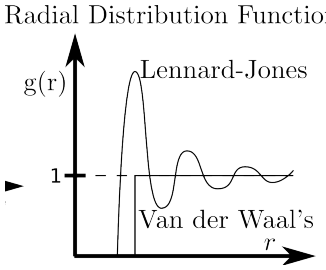

Under this assumption the energy $U_{\rm attr}$ associated with the attractive part of the potential $u_{\rm attr}$ is

$$U_{\rm attr} = \frac{1}{2} N\rho \int d^3 r u_{\rm attr}(r) \ ,$$

where the factor of $1/2$ avoids double-counting. It is convenient to define the quantity a,

$$a = -\frac{1}{2} \int d^3 r u_{\rm attr}({\rm r}) \ ,$$

which is a characteristic constant for a given species. The energy is then $U_{\rm attr} = -aN\rho = -aN^2/V$ and the contribution to the pressure is

$$p_{\rm attr} = -\frac{\partial U_{\rm attr}}{\partial V} = -a\rho^2 \ .$$

Thus, our first guess at a corrected equation of state is

$$p \simeq \rho k_B T - a\rho^2 \ .$$

Further, van der Waals realized that effect of the hard-core interactions could be accounted for by subtracting from the total volume V an amount proportional to the number of particles N, with an effective excluded volume per particle b. Putting these two effects together one has the revised equation of state

$$(p + a\rho^2)(V - Nb) = Nk_BT$$

Expanding for small ρ we find

$$\frac{p}{k_BT} \sim \rho + \left(b - \frac{a}{k_BT}\right)\rho^2 + \dots \ .$$

This shows that $B_2(T) = b - a/k_BT$, a form that is qualitatively like that seen in experiment. At high temperatures it saturates to a positive constant, reflecting entropic effects, whereas at low temperatures it is dominated by the attractive part of the potential. This shows the important point seen in many other contexts (such as polymer physics), that interaction terms quadratic in a density often must be interpreted as free energies (involving energy and entropy) rather than purely energetic.

2.2 Van der Waals interactions

Van der Waals' name is of course also associated with the long-range *fluctuating-dipole* interactions between neutral objects. Let us first get some insight into the physics responsible for the long-range attraction between neutral atoms or molecules. We reproduce essentially verbatim the very nice derivation in the literature (Holstein, 2001) which is based on the picture of two charged harmonic oscillators whose positive charges are fixed in place and whose negative charges can oscillate back and forth under the action of a spring of constant k:

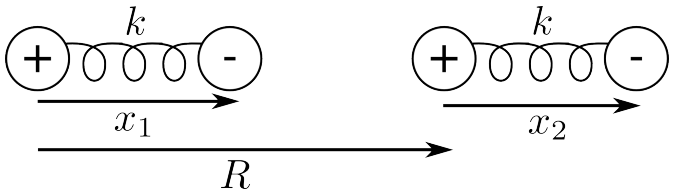

With $\omega_0^2 = k/m$, where m is the electron mass, the Hamiltonian is a sum of the electron kinetic energy, spring energy, and electrostatic interactions,

$$\begin{aligned}
\mathcal{H} &= \mathcal{H}_0 + \mathcal{H}_1 \\
\mathcal{H}_0 &= \frac{p_1^2}{2m} + \frac{1}{2}m\omega_0^2 x_1^2 + \frac{p_2^2}{2m} + \frac{1}{2}m\omega_0^2 x_2^2 \\
\mathcal{H}_1 &= e^2\left[\frac{1}{R} + \frac{1}{R - x_1 + x_2} - \frac{1}{R - x_1} - \frac{1}{R + x_2}\right]
\end{aligned}$$

This is exact but rather cumbersome. If we consider the physically-interesting limit in which the atoms are separated a distance large compared to their size, $|x_1|, |x_2| \ll R$, then

$$\mathcal{H}_1 \sim -\frac{2e^2 x_1 x_2}{R^3},$$

which we recognize as a dipole term from the R^{-3} fall-off with distance. To simplify the situation, a coordinate change is made:

$$x_\pm = \frac{x_1 \pm x_2}{\sqrt{2}} \qquad x_1 = \frac{x_+ + x_-}{\sqrt{2}} \qquad x_2 = \frac{x_+ - x_-}{\sqrt{2}} \ ,$$

and the Hamiltonian becomes

$$\mathcal{H} = \frac{p_1^2}{2m} + \frac{1}{2}\left(m\omega_0^2 - \frac{2e^2}{R^3}\right)x_+^2 + \frac{p_2^2}{2m} + \frac{1}{2}\left(m\omega_0^2 + \frac{2e^2}{R^3}\right)x_-^2 \ .$$

The two terms in parenthesis are modified frequencies,

$$\omega_+^2 = \omega_0^2 - \frac{2e^2}{mR^3} \qquad \omega_-^2 = \omega_0^2 + \frac{2e^2}{mR^3} \ ,$$

and so

$$\mathcal{H} = \frac{p_1^2}{2m} + \frac{1}{2}m\omega_+^2 x_+^2 + \frac{p_2^2}{2m} + \frac{1}{2}m\omega_-^2 x_-^2 \ .$$

Having diagonalized the Hamiltonian, we can easily calculate the change to the ground state energy of the system due to the Coulomb interactions. This interaction potential $u(r)$ is just the shift in zero-point energies,

$$u(r) = \frac{1}{2}\hbar\omega_+ + \frac{1}{2}\hbar\omega_- - 2\cdot\frac{1}{2}\hbar\omega_0 \simeq -\frac{1}{2}\hbar\omega_0\frac{(e^2/m\omega_0^2)^2}{R^6} + \cdots \ ,$$

where we have expanded the frequencies $\omega_\pm$ to the lowest non-vanishing order. In grouping the terms as shown in the final form above we have isolated a characteristic energy ($\hbar\omega_0$) that sets the overall scale for the interaction (it would be typical of an internal excitation energy from an s state to a p state, since fundamentally the interaction is due to virtual transitions to states with dipole moments). Recognizing the R^{-6} dependence, we observe that $e^2/m\omega_0^2$ must be a characteristic volume (remember we are working in cgs units!). To check this we note that the simplest relationship between an induced electric dipole moment $\mathbf{d}$ and an applied electric field $\mathbf{E}$ is

$$\mathbf{d} = \alpha\mathbf{E} \ ,$$

where α is known as the polarizability. As the dimensions of $\mathbf{d}$ are charge×length ($Q\cdot L$), and the units of $\mathbf{E}$ are Q/L^2 (cgs), the dimensions of α are L^3, that is a *volume*. That it is proper to interpret $e^2/m\omega_0^2$ as the polarizability can be seen by generalizing the original Hamiltonian to include an applied electric field of

magnitude E_0 in the x-direction, acting to displace the electrons only (recall that the positive charges are fixed in place),

$$\begin{aligned}\mathcal{H} &= \mathcal{H}_0 + eE_0x_1 + eE_0x_2 \\ &= \frac{1}{2}m\omega_0^2\left(x_1^2 + \frac{2eE_0x_1}{m\omega_0^2} \pm \left(\frac{eE_0}{m\omega_0^2}\right)^2\right) + (1 \leftrightarrow 2) \\ &= \frac{1}{2}m\omega_0^2 z_1^2 + \cdots \\ z_{1,2} &= x_{1,2} + \frac{eE_0}{m\omega_0^2} \ ,\end{aligned}$$

where the $\pm$ term in the second line indicates that we can add the indicated term to complete a square and then subtract it off separately. We thus see that we have a new pair of oscillators whose equilibrium positions are linearly shifted by the field. The induced dipole moment is thus the electron charge times that shift, $e^2E_0/m\omega_0^2$, so the polarizability is indeed

$$\alpha = \frac{e^2}{m\omega_0^2} \ .$$

Finally, in this model the interaction between the two fluctuating dipoles can be written in the simple form

$$u(r) = -\frac{1}{2}\frac{\hbar\omega_0\alpha^2}{r^6} \ .$$

2.2.1 Interaction of extended objects

Now can can use the basic result of the previous section to calculate the interaction energy between atoms and extended objects through a progression of geometries:

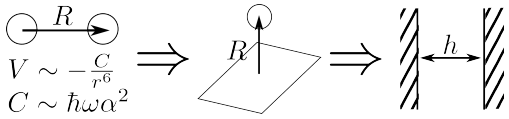

Let us denote the interaction between two point molecules as

$$V_{11}(r) = -\frac{C}{r^6} \ .$$

To calculate the attraction V_{1S} between one such neutral particle (at the origin) and a semi-infinite medium (a "slab") lateral in the $x-y$ plane, and filling the region $z > h$), we use cylindrical coordinates to obtain

$$\begin{aligned}V_{1S}(h) &= \int_h^\infty dz \int_0^{2\pi} d\phi \int_0^\infty r dr \rho V_{11}(\sqrt{z^2+r^2}) \\ &= -2\pi C\rho \int_h^\infty dz \int_0^\infty r dr \frac{1}{(z^2+r^2)^3} \\ &= -\frac{\pi C\rho}{6h^3} \ ,\end{aligned}$$

where ρ is the number density of particles in the slab. Note that the power law r^{-6} of the particle-particle potential has become r^{-3} by three spatial integrals (x, y, z).

With this we can calculate the interaction between two semi-infinite slabs by adding up all the contributions of the particles at varying distances from one slab within the other. Since there are $A\rho dz$ atoms each per thickness dz, the interaction energy is

$$V_{\rm SS}(h) = A\int_h^\infty \rho V_{\rm 1S}(z)dz \Rightarrow \frac{V_{\rm SS}}{A} = -\frac{A_H}{12\pi}\frac{1}{h^2} \ ,$$

where A_H is known as the Hameker constant. In the more general case of atoms of type 1 and 2 in the two slabs, with densities $\rho_{1,2}$ and a cross-interaction constant C_{12} we have

$$A_H = \pi^2\rho_1\rho_2 C_{12} \ .$$

From a scaling point of view, $A_H \sim \pi^2\hbar\omega(\alpha\rho)^2$, so with $\pi^2 \sim 10$, $\hbar\omega_0 \sim$ 3eV and $\alpha\rho \sim 0.1$ (typical of dense liquids), we estimate $A_h \sim 0.3$ eV $\sim 5\times10^{-20}$ J $\sim 5\times10^{-13}$ erg, which is an order of magnitude larger than thermal energy at 300K. Just as importantly, this interaction scales with the inverse square of the distance, which produces a very long-range force.

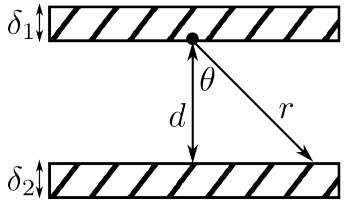

A simple generalization of the previous calculation yields the interaction between two laterally-infinite slabs of *finite* thickness δ_1 and δ_2, relevant to the interaction of pairs of nearby lipid membranes. The interaction of a single atom a distance d from the slab of thickness δ_1 is

$$V_{\rm 1S}(d) = -\frac{\pi C\rho}{6}\left\{\frac{1}{d^3} - \frac{1}{(d+\delta_1)^3}\right\} \ ,$$

which, by integration over slab 2 yields the energy per unit area

$$\frac{V_{\rm SS}(d)}{A} = -\frac{\pi C\rho^2}{12}\left\{\frac{1}{d^2} - \frac{1}{(d+\delta_1)^2} - \frac{1}{(d+\delta_2)^2} + \frac{1}{(d+\delta_1+\delta_2)^2}\right\}$$

At long distances this interaction scales as d^{-4}. On the examples sheet we will examine the sphere-sphere interaction, which is discussed extensively in the book by Verwey and Overbeek.

2.3 Screened electrostatic interactions

Many of the interesting objects in biology interact both through van der Waals forces and (screened) electrostatic interactions. As

the former typically decay as an inverse power of distance, and the latter (as we shall see) decays exponentially, the combined potential is attractive at long distances. Depending on the length scales and amplitudes in a given system, at shorter distances there can be a secondary minimum separated by a potential barrier from the minimum at the very close separations (see figure). This complex interplay between the two contributions can give rise to many interesting phenomena. Our first goal is to understand the electrostatic contribution.

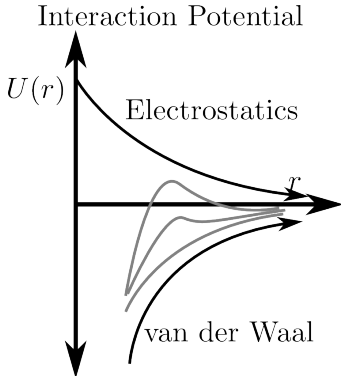

Two charges in vacuum separated by a distance r have an electrostatic energy (in cgs units) of

$$\mathcal{E} = e\phi(r) = \frac{e^2}{r} \ ,$$

where ϕ is the electrostatic potential. If we measure r in the molecule scale of $\mathring{A}$ the ratio of electrostatic to thermal energy is

$$\frac{\mathcal{E}}{k_B T} = \frac{(4.8 \times 10^{-10})^2}{4 \times 10^{-14} \cdot 10^{-8}} = \frac{580}{r[\mathring{A}]}$$

However, the dielectric constant $\epsilon \sim 80$, so even apart from screening the energy is reduced to $e^2/\epsilon r$. Turning this around, we define the *Bjerrum length* λ_B as the point of balance:

$$\lambda_B = \frac{e^2}{\epsilon k_B T} \sim 7\mathring{A}$$

Even pure water has small amounts of ionic species (H^+/OH^-) at equilibrium. These and other ions present will tend to screen the bare electrostatic interactions considered above. Effectively, mobile charges opposite in sign to a given charge will cluster around it in a diffuse cloud, screening it from other distant charges. The standard formalism to compute the ionic distribution and resulting interactions is known as Poisson-Boltzmann theory, or, in its linearized form, as Debye-Hückel theory. PB theory is based on two assumptions.

1. The Poisson equation relating the electrostatic potential ϕ to the charge density ρ:

$$\nabla^2 \phi = -\frac{4\pi\rho}{\epsilon} \qquad \mathbf{E} = -\boldsymbol{\nabla}\phi$$

2. The Boltzmann distribution, relating the ionic concentrations c_s of the species s of valence z_s to the electrostatic potential

$$c_s = c_0 e^{-z_s e\phi/k_B T} \ ,$$

where c_0 is a background concentration.

Combining these into a single self-consistent equation (with $\beta = 1/k_B T$), we obtain the *Poisson-Boltzmann equation*

$$\nabla^2 \phi = -\frac{4\pi}{\epsilon} \sum_{species\ s} z_s e c_0 e^{-\beta z_s e\phi} \ .$$

If we consider the specific case of a $z:z$ electrolyte (1:1, NaCl, 2:2, $CuSO_4$ etc.), we can write this in a more compact form

$$\nabla^2 \phi = \frac{8\pi z e c_0}{\epsilon} \sinh(\beta z e \phi) \ .$$

This is a very nonlinear equation for which analytical solutions can be found only in very simplified geometries. Much of the important physics of screened electrostatics can be seen in the *weak field* limit, when $\beta e\phi \ll 1$. We then linearize the PB equation (using $\sinh(x) \simeq x + \cdots$) to obtain

$$\nabla^2 \phi = \frac{8\pi z^2 e^2 c_0}{\epsilon k_B T} \phi + \ldots$$

Comparing the two sides of this equation we infer on dimensional grounds that there is a characteristic length scale, the Debye-Huckel length λ_{DH}:

$$\lambda_{DH} = \left[\frac{\epsilon k_B T}{8\pi z^2 e^2 c_0} \right]^{1/2} \sim \frac{10 \text{ nm}}{\sqrt{c_0[\text{mM}]}} \ ,$$

where in the final expression we have expressed the concentration in the biologically relevant units of millimolar (mM). Our first important conclusion is that this length scale is nanometric for typical biophysical contexts.

In this Debye-Hückel limit the electostatics is governed by the *modified Helmholtz equation*,

$$\left(\nabla^2 - \lambda_{DH}^{-2}\right) \phi = 0 \ .$$

Solving this problem first for a surface occupying the $y-z$ plane ($x = 0$), we observe that the general solution of

$$\left(\frac{\partial^2}{\partial x^2} - \lambda_{DH}^{-2} \right) \phi = 0$$

is

$$\phi = A e^{x/\lambda_{DH}} + B e^{-x/\lambda_{DH}} \ .$$

In this case, $A = 0$ by the requirement of a bounded solution as $x \to \infty$, and if the surface potential is held at ϕ_0, then

$$\phi = \phi_0 e^{-x/\lambda_{DH}}$$

There is an induced charge density σ on the surface which can be computed in the usual way (Gaussian pillbox),

$$-\hat{\mathbf{n}} \cdot \boldsymbol{\nabla}\phi|_{\text{surf}} = \frac{4\pi\sigma}{\epsilon} \Rightarrow \sigma_0 = \frac{\epsilon}{4\pi\lambda_{DH}}\phi_0 \ ,$$

where $\hat{\mathbf{n}}$ is the *outward* normal to the surface.

It is important to note here that the charge density depends on the screening length in solution. This is a characteristic feature of this problem. In Debye-Hückel theory there is a linear relationship between the induced charge and ϕ_0, while in the more general case the relationship is non-linear, which leads to more interesting problems like Manning condensation (Manning, 1969).

Once we have the potential everywhere and the charge on the surface we should be able to find the (free) energy of the system. Observe that $\nabla^2\phi - \lambda_{DH}^{-2}\phi = 0$ is the Euler-Lagrange equation for the functional

$$\tilde{\mathcal{F}} = \frac{\epsilon}{4\pi}\int d^3r \left[\frac{1}{2}(\boldsymbol{\nabla}\phi)^2 + \frac{1}{2}\lambda_{DH}^{-2}\phi^2\right]$$

where we employ the general Euler-Lagrange formula

$$\frac{\delta\tilde{\mathcal{F}}}{\delta\phi} = -\frac{\partial}{\partial x}\frac{\partial(\cdots)}{\partial\phi_x} + \frac{\partial(\cdots)}{\partial\phi} \ ,$$

where $(\cdots)$ is the integrand of the functional. We recognize the first term as the electrostatic energy density $\epsilon\mathbf{E}^2/8\pi$. The second is the weak-field approximation of an entropic contribution.

Now, here's the crucial point. If we take the original free energy and integrate by parts the term involving $(\nabla\phi)^2$, we obtain a surface term and a new bulk contributiion (that is, using Green's first identity),

$$\tilde{\mathcal{F}} = \frac{\epsilon}{8\pi}\int_S dS\phi\hat{\mathbf{n}}' \cdot \boldsymbol{\nabla}\phi - \frac{\epsilon}{8\pi}\int d^3r\phi\left(\nabla^2\phi - \lambda_{DH}^{-2}\phi\right) ,$$

where σ is the surface charge and here $\hat{\mathbf{n}}'$ is the surface normal pointing *out* of the volume containing the ionic medium, and hence *into* the surface. Noting that the the bulk term vanishes by the DH equation, we are left only with the surface term. Re-expressed in terms of the outward normal of the surface we can rewrite the energy in terms of the surface charge density σ as

$$\tilde{\mathcal{F}} = \frac{1}{2}\int_S dS\sigma\phi \ .$$

This is the appropriate energy for a system in which the surface charge is specified.

For situations with fixed surface potential rather than fixed charge, the surface free energy must be Legendre transformed, which is equivalent to accounting for the work done against the battery that held the potential fixed. This new free energy F is

$$\mathcal{F} = \tilde{\mathcal{F}} - \int_S dS\sigma\phi = -\frac{1}{2}\int_S dS\sigma\phi \quad \text{or} \quad -\int_S dS \int^{\phi_0} \sigma(\phi')d\phi' \ ,$$

the latter relation holding in the more general case of a nonlinear relationship between charge and potential.

2.3.1 Interaction between surfaces

Now we move on to calculate the interaction of two surfaces, noting some distinctions between the cases of fixed potential and fixed charge. For two surfaces held at the same potential ϕ_0, located at $x = \pm d/2$ (see figure),

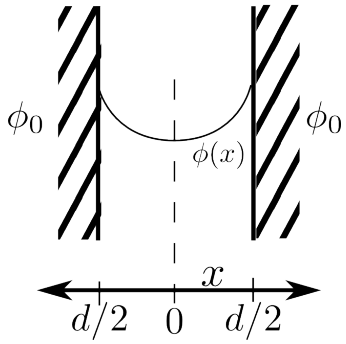

the potential is the symmetric combination of the fundamental exponential solutions found previously,

$$\phi = \phi_0 \frac{\cosh(x/\lambda)}{\cosh(d/2\lambda)} \ ,$$

where the denominator is chosen to enforce the boundary conditions, and we write λ for the DH screening length. Using this we find the charge density at the plate at $z = d/2$. Here, $-\hat{\mathbf{n}} \cdot \boldsymbol{\nabla} = d/dz$, so

$$\sigma(d/2) = \frac{\epsilon\phi_0}{4\pi\lambda} \tanh(d/2\lambda) \ .$$

At the left-hand surface we have $-\hat{\mathbf{n}} \cdot \boldsymbol{\nabla} = -d/dz$, but with $\sinh(-d/2\lambda) = -\sinh(d/2\lambda)$ the charge density is the same. As the charge and potential do not vary with position over these flat surfaces the surface integration will just give a factor of the surface area A. Normalizing by the area of the *two* surfaces the free energy is

$$\frac{\mathcal{F}(d)}{2A} = -\frac{1}{4}\sigma\phi_0 = -\frac{\epsilon\phi_0^2}{8\pi\lambda} \tanh(d/2\lambda)$$

The interesting quantity is the difference between this and the energy at infinite separation,

$$\frac{\mathcal{F}(d)-\mathcal{F}(\infty)}{2A}=\frac{\epsilon\phi_0^2}{8\pi\lambda}\left[1-\tanh\left(\frac{d}{2\lambda}\right)\right]$$

At large arguments tanh approaches unity from below, so this is clearly a repulsion, as expected. In detail, if $d/\lambda \gg 1$ we note that $\tanh(z) \simeq 1 - 2\mathrm{e}^{-2z} + \cdots$, so

$$\frac{\Delta\mathcal{F}(d)}{2A}\simeq\frac{\epsilon\phi_0^2}{4\pi\lambda}\mathrm{e}^{-d/\lambda}\ ,$$

so the repulsive free energy has the same exponential decay as the electrostatic potential. The second point of interest is that the potential is bounded as $d \to 0$, as the induced charge density decreases monotonically.

Now we consider the case of two surfaces with fixed charge density σ_0. Since we require that the derivative of the potential be a given value on the surface it is easy to see that the required potential has a normalizing denominator that is the derivative of the numerator,

$$\phi(x)=\frac{4\pi\lambda\sigma_0}{\epsilon}\frac{\cosh(x/\lambda)}{\sinh(d/2\lambda)}\ .$$

The potential at the surface is

$$\phi(d/2)=\frac{4\pi\lambda\sigma_0}{\epsilon}\coth(d/2\lambda)\ ,$$

and finally the interaction energy per unit area is

$$\frac{\tilde{\mathcal{F}}(d)-\tilde{\mathcal{F}}(\infty)}{2A}=\frac{2\pi\sigma_0^2\lambda}{\epsilon}\left[\coth\left(\frac{d}{2\lambda}\right)-1\right]\ .$$

The function coth approaches its asymptote from above, so we again have a repulsive interaction, but this time there is a divergence at short distances due to the condition that the charge density is fixed.

To put the scale of energies involved in perspective, we examine typical values of the charge density. A typical lipid has a cross sectional area of about $50 - 100\ \mathring{A}^2$. If each head group holds a single charge, and the Debye-Hückel length λ_{DH} is about 1 nm, then the typical energy is:

$$\frac{\tilde{\mathcal{F}}}{A}\sim 50\frac{\mathrm{erg}}{\mathrm{cm}^2}$$

Remembering that the surface tension of water is about 80 erg/cm^2 we see that these electrostatic effects can be large.

2.3.2 An aside on quadratic energy functionals

We will see a number of situations in which quadratic energy functionals show up in soft and biological systems, so it is worthwhile to remind ourselves of other places they occur. A good example is found in the computation of the shape of a liquid meniscus that meets a solid wall at some contact angle θ (figure below). The shape of the meniscus is a compromise between the effects of surface tension and gravity.

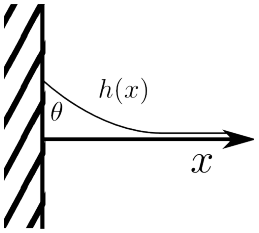

We assume that this three-dimensional system has translational invariance in the direction normal to the page, and formulate the energy per unit length in that orthogonal direction,

$$\frac{E}{L} = \int dx \left[\gamma \sqrt{1 + \left(\frac{\partial h}{\partial x} \right)^2} + \frac{1}{2} \Delta \rho g h^2 \right]$$

where σ is the surface tension and $\delta\rho$ is the density difference between the fluid below the meniscus and above. The first term represents the arclength of the curve $h(x)$, while the second is the gravitational potential energy of the meniscus relative to $h = 0$. It is quadratic because it accounts for the potential energy in the infinitesimal *columns* of fluid of height h, rather than the linear-in-h form for a point mass in a gravitational field.

As usual, the pedagogically interesting limiting case is the one in which the local slope of the interface is small, so we expand the square root assuming $|h_x(x)| \ll 1$, with $\sqrt{1 + h_x^2} \simeq 1 + (1/2)h_x^2 + \ldots$ and consider the difference in energy $\Delta E = E(h) - E(0)$ between that for a given function $h(x)$ and the flat state,

$$\frac{\Delta E}{L} \approx \frac{1}{2} \int_0^\infty dx \left[\frac{1}{2} \sigma h_x^2 + \Delta \rho g h^2 \right] \ .$$

Again we will find that there is a characteristic length scale in the system, which is the capillary length l_c,

$$\frac{1}{l_c^2} \sim \frac{\Delta \rho g}{\sigma} \quad \Rightarrow \quad l_c \sim \sqrt{\frac{\sigma}{\Delta \rho g}}$$

which, for water/air, is about 3mm ($\sqrt{100/1/1000}$).

2.3.3 Long, linear, charged objects (e.g. DNA)

We will present a very brief discussion of the unusual statistical physics associated with charged linear objects, such as DNA. now

try to merge the two concepts, surface tension and wetting on the one hand, and electrostatics on the other. We will investigate this by considering a flexible, charged object like DNA or a biological membrane. In equilibrium this object is flat, however, here we will try to see what happens when we are bending it.

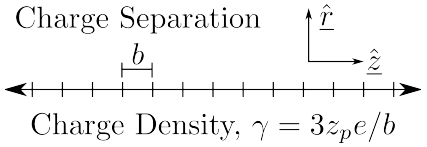

Let us imagine there is a linear object of uniform charge density γ (Manning, 1969):

$$\gamma = \frac{z_p e}{b}$$

where z_p is the valence, e is the charge of an electron, and b the typical charge spacing. In cylindrical coordinates, the energy of a test charge of valence z_i is

$$U_{ip} = -z_i e \frac{2\gamma}{\epsilon} \ln(r) \ .$$

If we assume a probability density that is based on this electrostatic energy we find the power-law form

$$e^{-\beta U_{ip}(r)} = \exp(2z_i z_p e^2/\epsilon b k_B T) = r^{2z_i z_p \lambda_B/b}$$

where λ_B is the Bjerrum length we previously introduced. If we try to normalize this charge density we are confronted with an integral of the form

$$\int 2\pi dr e^{-\beta U_{ip}(r)} \sim \int dr r^{1+2z_i z_p \lambda_B/b}$$

If the test charge is a counterion ($z_i z_p < 0$) and $\lambda_B/b \geq |z_i z_p|^{-1}$ then the normalization will fail at the origin. This is the origin of what is known as *Manning condensation*, where counter-ions collapse to the linear polymer (Manning, 1969), canceling the bare charge and reducing γ to the point of convergence.

2.4 Geometrical aspects of screened electrostatics

The problem now is to quantify the contribution of charges to the stiffness of an object. Here, we will use various methods to solve this problem within an approximation that takes advantage of a small parameter. We have already identified the screening length λ which characterizes the width of the electric double layer. This can be compared to the radius of curvature R of a bent object, whether a filament or a membrane. In most situations the bending radius is much larger than λ, so that $\lambda/R \ll 1$ serves as a dimensionless small parameter.

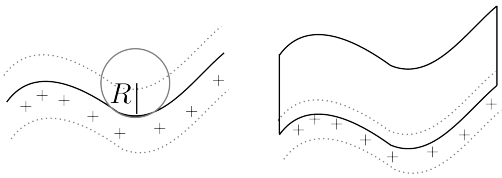

Our calculations will be based on the membrane problem, and we recall that at every point of a surface there are two principal radii R_1 and R_2 and from these we can construct two geometric quantities. One is the *mean curvature* $H = (1/2)(1/R_1 + 1/R_2)$ and the second is the *Gaussian curvature* $K = 1/(R_1 R_2)$. With the help of these curvatures we can now write down the energy function of a membrane, which is a quadratic form

$$\varepsilon = \int dS \left[\frac{1}{2} k_c (H - H_0)^2 + \frac{1}{2} \overline{k}_c K \right] .$$

This was introduced by Helfrich and others for a non-stretching, bending membrane. There are two elastic constants that describe the energy cost to produce bends. The quantity H_0 is known as the *spontaneous curvature* and represents the possibility of a preferred curvature in the ground state. It is often a constant, but can vary from place to place if the membrane composition is spatially variable, for instance.

Our goal is to find the electrostatic contributions to the elastic constants and the spontaneous curvature. This can be done three ways.

1. Dating back to work by Winterhalter and Helfrich (Winterhalter and Helfrich, 1988) and others, we can compare the energy of different simple geometries where the various curvatures are constant. For the plane we have $R_1 = R_2 = \infty$. For a cylinder we have one vanishing curvature, and for the sphere $R_1 = R_2$. Comparing the results with the terms in the Helfrich energy in an expansion in powers of λ_{DH}/R we can find the elastic constants and the spontaneous curvature.
2. Construct a perturbation theory around a flat surface. This provides a good context to understand "boundary perturbation theory".
3. Use a variant of *multiple scattering theory*. This is very complicated and not covered in this course, but it is described in the references.

We will now start with the geometric comparison method and consider the geometries described above.

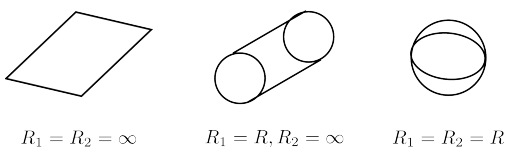

To simplify notation we use $\kappa = 1/\lambda_{DH}$. Since we already solved the electrostatic problem for a plane, we next consider the cylinder. We wish to solve the modified Helmholtz equation,

$$(\nabla^2 - \lambda_{DH}^{-2})\phi = 0 \ ,$$

with the radial part of the Laplacian

$$\nabla^2\phi = \frac{1}{r}\frac{\partial}{\partial r}\left(r\frac{\partial\phi}{\partial r}\right) = \phi'' + \frac{1}{r}\phi' \ .$$

Rearranging, we obtain

$$\left(r^2\partial_{rr} + r\partial_r - (\kappa r)^2\right)\phi = 0.$$

As this is homogeneous in powers of r the solution is only a function of κr. The two solutions to this are $K_0(\kappa r)$ for the outer problem (decaying at infinity) and $I_0(\kappa r)$ for the inner problem (well-behaved at the origin). These are *modified Bessel functions*

In the case of a fixed charge, the inner problem has a solution of the form

$$\phi = \frac{4\pi\sigma}{\epsilon\kappa}\frac{I_0(\kappa r)}{I_1(\kappa R)}$$

and the free energy will involve a ratio of the form

$$\tilde{\mathcal{F}} \sim \frac{I_0(\kappa r)}{I_1(\kappa R)} \ .$$

This is very naturally set up for an expansion in inverse powers of κR, using the asymptotic results

$$I_\nu(z) = \frac{\mathrm{e}^z}{\sqrt{2\pi z}}\left\{1 - \frac{\mu-1}{8z} + \frac{(\mu-1)(\mu-9)}{2!(8z)^2} + \cdots\right\}$$

where $\mu = 4\nu^2$. We see that the prefactors in front of the large brackets cancel in the ratio I_0/I_1, leaving the desired expansion.

We leave it to the student to complete the calculation given in the examples sheet.

Next, we sketch the basic features of a perturbative approach to finding the energetics of electric double layers near a non-flat boundary. In the simplest case we imagine a surface that has some non-trivial height function $h(x)$ in one direction only, and the surface is held at a fixed potential ϕ_0. That is

$$\phi(x, h(x)) = \phi_0.$$

The mathematical problem is centered around the fact that in general we do not know the Green's function of the modified Helmholtz operator for the domain bounded by some arbitrary height function $h(x)$. But, we can perturbatively connect the solutions at finite $h(x)$ to those at $h = 0$, where we know the solution.

Hence, we introduce a dimensionless small parameter ϵ as a counting device. The boundary condition can then be expanded as

$$\phi(x, \epsilon h(x)) \simeq \phi(x,0) + \epsilon\phi_y(x,0) + \frac{1}{2}\epsilon^2\phi_{yy}(x,0) + ...$$

where the subscript denotes a partial derivative with respect to y, $\phi_y = \partial\phi/\partial y$.

Now, we expect that the solution itself (in the bulk) also has an expansion in powers of ϵ,

$$\phi(x,y)) \simeq \phi^{(0)}(x,y) + \epsilon\phi^{(1)}(x,y) + \epsilon^2\phi(2)(x,y) + \cdots \ .$$

The governing equation does not depend on ϵ, so at every order we will have

$$(\partial_{xx} + \partial_{yy} - \kappa^2)\phi^{(n)}(x,y) = 0 \ .$$

Merging the expansion of the boundary condition with the expansion of the solution we arrive at a sequence of boundary conditions for each order of solution. Up to second order in ϵ we have

$$\begin{aligned}\phi_0 = \phi^{(0)}(x,0)) + \epsilon\phi^{(1)}(x,0) + \epsilon^2\phi(2)(x,0) + \cdots \\ +\epsilon h(x)\left[\phi_y^{(0)}(x,0)) + \epsilon\phi_y^{(1)}(x,0) + \cdots\right] \\ +\frac{1}{2}\epsilon^2 h^2(x)\left[\phi_{yy}^{(0)}(x,0)) + \cdots\right] + \cdots\end{aligned}$$

At order ϵ^0 we simply recover the boundary condition at a flat surface:

$$\mathcal{O}(\epsilon^0): \qquad \phi^{(0)}(x,0) = \phi_0 \ ,$$

and we can immediately write down the solution for all (x,y) as

$$\phi^{(0)}(x,y) = \phi_0 \mathrm{e}^{-\kappa y} \ .$$

At the next order we find the boundary condition

$$O(\epsilon^1): \qquad \phi^{(1)}(x,0) = -h(x)\phi_y^{(0)}(x,0) = \kappa h(x)\phi_0 \ .$$

Thus, the problem with a boundary condition on a curved surface has become one with a flat boundary but an inhomogeneous potential. At quadratic order we have a similar kind of result,

$$O(\epsilon^2): \qquad \phi^{(2)}(x,0) = -\frac{1}{2}h^2(x)\phi_{yy}^{(0)}(x,0) - h(x)\phi_y^{(1)}(x,0) \ .$$

A convenient way to solve these boundary-value problems is to work in Fourier space. Let us define

$$\hat{\phi}^{(m)}(k,y) = \int dx \mathrm{e}^{ikx}\phi^{(m)}(x,y) \quad \text{and} \quad \hat{h}(q) = \int dx \mathrm{e}^{iqx}h(x) \ .$$

The modified Helmholtz equation $(\partial_{xx} + \partial_{yy} - \kappa^2)\phi = 0$ then becomes

$$\left(\partial_{yy} - \kappa_q^2\right) \hat{\phi}^{(n)}(q, y) = 0 \ , \qquad \text{where} \qquad \kappa_q^2 = \kappa^2 + q^2 \ .$$

This is easily solved, as

$$\hat{\phi}^{(n)}(q, y) = \hat{\phi}^{(n)}(q, 0)\mathrm{e}^{-\kappa_q y} \ .$$

Thus, we need to know the Fourier transform of the functions at $y = 0$, but this can be determined directly from the order-by-order boundary conditions. For example, at order ϵ^1 we have

$$\phi^{(1)}(x, 0) = \kappa\phi_0 h(x) \ ,$$

so

$$\hat{\phi}^{(1)}(q, 0) = \kappa\phi_0 \hat{h}(q)$$

This we must do order by order. In addition, depending on the boundary conditions, we may need to expand the surface normal vector,

$$\hat{\mathbf{n}} = -\frac{-h_x \hat{\mathbf{e}}_x + \hat{\mathbf{e}}_y}{\sqrt{1 + h_x^2}} \ ,$$

in order to compute the surface charge as

$$\sigma(x) = -\frac{\epsilon}{4\pi} \hat{\mathbf{n}} \cdot \boldsymbol{\nabla}\phi(x, \epsilon h(x)) \ .$$

We leave the details for the problem in the example sheet.

Fluctuations and Fluctuation-Induced Forces

3

3.1 Review of Statistical Physics

We will not present a complete review of classical statistical physics, but instead will simply highlight a few key points relevant to the applications in this course. The fundamental relation is that the probability $p(E)$ of finding a system in a state of energy E is

$$p(E) = \frac{e^{-\beta E}}{Z} \ ,$$

where $\beta = 1/k_B T$, and the partition function Z is

$$Z = \sum_i e^{-\beta E_i}$$

where the index i runs over all possible states of the system. The expectation value of a physical quantity A of the system is

$$\langle A \rangle = \sum_i A(E_i) \frac{e^{-\beta E_i}}{z} \ .$$

We will typically deal with system for which the energy is simply the sum of kinetic and potential contributions. For a single particle this might look like

$$E = \frac{p^2}{2m} + U(q)$$

where q is some generalized coordinate.

The classical partition function for a system of N particles is simply

$$Z = \frac{1}{N! h^{3N}} \int d^3p^N \int d^3q^N \exp\left(-\beta \left[\sum_i \frac{p_i^2}{2m} + \exp\left(U(q^N)\right) \right] \right)$$

where we use the notation p^N and q^N to stand for the whole set of variables. The prefactor is appropriate for indistinguishable particles, and there is a phase space normalization factor of h (Planck's constant) for every pair of p and q.

Since there is no issue of the non-commutation of positions and momenta we can perform the momentum integrals exactly, yielding

$$Z = \frac{1}{N!} \frac{1}{\Lambda^{3N}} \int d^3q^N \exp\left(-\beta U(q^N)\right)$$

where the thermal de Broglie wavelength Λ is

$$\Lambda = \frac{h}{\sqrt{2\pi m k_B T}} \ .$$

Note that h appears only as a prefactor, and thus will play no role in almost all observables.

When the configurational energy is qudratic in the generalized coordinate,

$$E = \frac{1}{2}kx^2 \ ,$$

then the theorem of equipartition holds. Observe that

$$\left\langle \frac{1}{2}kx^2 \right\rangle = \frac{\int dx \frac{1}{2}kx^2 e^{-\beta k x^2/2}}{\int dx e^{-\beta k x^2/2}} = -\frac{\partial \ln Z}{\partial \beta}$$

. This means that we can view $\ln Z$ as a *generating function*. Now change variables in Z, pulling the constants out in front,

$$Z = \int dx e^{-\beta k x^2/2} \sqrt{\frac{\beta k}{2}} \sqrt{\frac{2}{\beta k}} = \sqrt{\frac{2}{\beta k}} \int dq e^{-q^2} \ ,$$

and so

$$\ln Z = -\frac{1}{2}\ln\beta + \text{terms independent of } \beta \qquad -\frac{\partial \ln Z}{\partial \beta} = \frac{1}{2\beta} = \frac{1}{2}k_B T \ .$$

Thus, the energy per mode or degree of freedom is

$$\left\langle \frac{1}{2}kx^2 \right\rangle = \frac{1}{2}k_B T \ .$$

3.2 Polymers and Entropic Forces

In this section we will develop basic concepts of polymer physics, with emphasis on the concept of an *entropic spring*. Polymers are defined as long chain molecules with repeating sub-units. Examples include

(1) DNA: A covalently bonded polymer with nucleotide units

(2) Microtubules: Aggregates of protein monomers, held together with electrostatics and van der Waals forces. Due to the weak bonding these polymers fluctuate in length.

(3) Linear/branched: Most proteins are single chains, but molecules with multiple attachments are possible.

(4) Cross-linked networks: interlocked chains of polymers are necessary for many cellular functions.

3.2.1 Simplest model of polymers

The simplest model of a polymer is one in which there are N identical links of length b, each of which can be oriented up or down. Consider the case in which it is stretched by a mass pulled down by gravity.

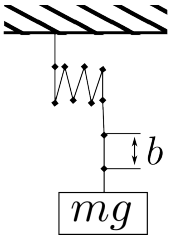

With a reference point at zero extension, the energy is $E = -mgz$, where the extension z is

$$z = \sum_{n=1}^{N} b s_n \ ,$$

where $s_n = \pm 1$ denotes the orientation of the nth link. The partition function is thus

$$Z = \sum_{s_1} ... \sum_{s_2} \exp\left(\beta mgb \sum s_n\right) \ ,$$

which, by the independence of the s_n, can be simplified to

$$Z = \prod_{n=1}^{N} \sum_{s_n=\pm 1} \mathrm{e}^{\beta mgb s_n} = [2\cosh(\beta mgb)]^N \ .$$

From this we can calculate the mean extension as a function of the force $F = mg$,

$$\langle z \rangle = \langle b \sum_n s_n \rangle = -\frac{\partial \ln Z_n}{\partial(\beta F)} = Nb \tanh(\beta F b) = L \tanh(\beta F b) \ ,$$

where L is the fully-extended polymer length.

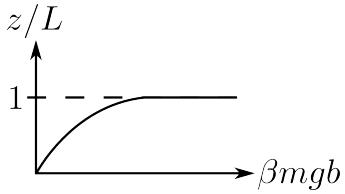

For a weak force, the average length z can be Taylor expanded

$$\langle z \rangle = \frac{Nb^2}{k_B T} F + \dots \ .$$

This is nothing but a Hookean spring relationship (force proportional to extnesion), with a spring constant.

$$k = \frac{k_B T}{Nb^2}$$

This result is especially interesting because the restoring force stems entirely from entropy. Work is done to reduce the entropy when the chain is extended. For example, at full extension there is only one configuration, so a minimum in entropy.

3.2.2 The freely-jointed chain

Now we examine a more realistic model in which every link is freely-jointed. Applying a force F to this look like this:

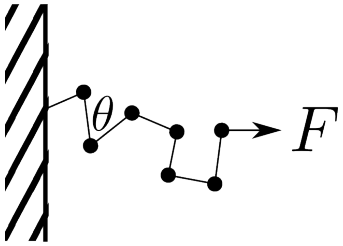

The extension x and energy E are

$$x = \sum_{n=1}^{N} b\cos\theta_N \qquad E[\{\theta_n\}] = -Fb\sum_{n=1}^{N}\cos\theta_n \ .$$

The partition function is then

$$\begin{aligned} Z &= \prod_{n=1}^{N} 2\pi \int d\theta_n \sin\theta_n \mathrm{e}^{f\cos\theta_n} \qquad f = \frac{Fb}{k_B T} \\ &= \left[\frac{4\pi\sinh(f)}{f}\right]^N \ . \end{aligned}$$

The average extension follows by differentiation,

$$\langle x\rangle = b\frac{\partial \ln Z}{\partial f} = Nb\mathcal{F}(f) \qquad \mathcal{L}(f) = \coth(f) - \frac{1}{f} \ ,$$

where $\mathcal{L}$ is the Langevin function. The spring constant for this new chain is

$$k = \frac{3k_B T}{Nb^2}$$

which reflects the three degrees of freedom per link.

3.3 Fluctuating continuous objects

No we consider how to generalize these kinds of analyses to fluctuating continuous objects such as membranes and biofilaments. of filaments like microtubules or a membrane. A simple place to being is with a 1D string stretched by two hanging masses, and thereby under tension:

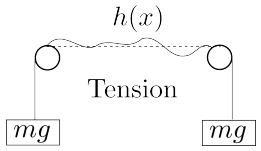

The energy of this object, relative to that of a straight string, is the product of the line tension γ and the excess arclength,

$$\Delta E = \gamma \left[\int_0^L dx \sqrt{1 + h_x^2} - L \right] ,$$

Where $h_x = \partial h / \partial x$. Expanding the squre root under the assumption of a weakly-sloping curve we have

$$\Delta E \sim \frac{\gamma}{2} \int_0^L dx h_x^2 + \dots$$

In this form we can not apply equipartition directly as there are no identifiable independent modes. But, if we note the pinned boundary conditions at $x = 0$ and $x = L$ we can use a Fourier series,

$$h(x) = \sum_{n=1}^{\infty} A_n \sin\left(\frac{n\pi x}{L}\right) .$$

By the orthogonality of the modes, a little algrebra show that

$$\Delta E = \frac{\gamma L}{4} \sum_{n=1}^{\infty} \left(\frac{n\pi}{L}\right)^2 A_n^2 .$$

This decomposition holds for any particular realization of the Fourier coefficients A_n. Note the explicit appearance of the system size L. If the string is in thermal equilibrium (e.g. connected to a heat bath), then the probability distribution of the A_n is just a Gaussian, with a mean of

$$\langle A_n \rangle = 0$$

and an energy per mode of

$$\langle E_n \rangle = \frac{k_B T}{2} = \frac{\gamma \pi^2 n^2}{4L} \langle A_n^2 \rangle \quad \rightarrow \quad \langle A_n^2 \rangle = \frac{2 k_B T}{\gamma \pi^2 n^2} L .$$

The average variance of the string can then be calculated:

$$\begin{aligned} \langle h^2(x) \rangle &= \sum_m^{\infty} \sum_n^{\infty} \langle A_m A_n \rangle \sin\left(\frac{m\pi x}{L}\right) \sin\left(\frac{n\pi x}{L}\right) \\ &= \frac{2 k_B T L}{\gamma \pi^2} \sum_{n=1}^{\infty} \frac{\sin^2\left(N\pi x/L\right)}{n^2} . \end{aligned}$$

As a check, γ has units of Energy/Length, so that the sum has units of Length^2. Note again the interesting dependence on the system size. The variance is linear in L, which should remind you of a random walk.

3.3.1 Energy Calculations in Fourier Space

Rather than doing summations over discrete modes, in many cases we would like to consider a system large enough that a continuum of modes is reasonable. To that end, we return to the string energy and write

$$E = \frac{\gamma}{2}\int dx h_x^2 \qquad\qquad h_x = \sum_q e^{-iqx}\hat{h}(q)$$

where $\hat{h}(q)$ is the discrete Fourier transform of $h(x)$. Substituting, we have

$$E = \frac{\gamma}{2}\int dx \sum_q \sum_{q'} (-iq)(-iq')e^{-i(q+q')x}\hat{h}(q)\hat{h}(q') \ .$$

This can be simplified with

$$\int_0^L dx e^{-ipx} = L\delta_{p,0} \rightarrow E = \frac{\gamma L}{2}\sum_q q^2|\hat{h}(q)|^2$$

where $\delta_{p,0}$ s the Kronecker δ.

We are now able to use the equipartition theorem:

$$\left\langle |\hat{h}(q)|^2 \right\rangle = \frac{k_B T}{\gamma L}\frac{1}{q^2}$$

We denote the thermal average by $\langle h^2\rangle$. A second average of interest is the *system average*, denoted by $\overline{\langle h^2\rangle}$,

$$\overline{h^2} = \frac{1}{L}\int_0^L dx h^2 \ .$$

The thermal average fo the system average has a very compact form,

$$\overline{\langle h^2\rangle} = \sum_q \langle |\hat{h}(q)|^2\rangle \ .$$

This is still a discrete sum. In the continuum limit, we use the fundamental relation

$$\frac{1}{L}\sum_q \rightarrow \int dq/2\pi \ ,$$

so

$$\overline{\langle h^2\rangle} = \frac{k_B T}{2\pi\gamma}\int \frac{dq}{q^2} \ .$$

For this and other integrals of this type we may need to introduce integration cutoffs. These usually occur in either of two forms:

(1) Small scale: Molecular lengths a limit small scale fluctuations.

(2) Large scale: Limited system size L prevents long wavelength fluctuations.

Accounting for such cutoffs:

$$\overline{\langle h^2 \rangle} = \frac{k_B T}{2\pi\gamma}\left(\frac{1}{q_{\min}} - \frac{1}{q_{\max}}\right) \qquad q_{\min} = \frac{\pi}{L} \qquad q_{\max} = \frac{\pi}{a} \ .$$

Considering the basic object in the energy, we have

$$\overline{\langle h_x^2 \rangle} \sim \frac{k_B T}{\gamma}\int \frac{dq}{q^2} q^2 \sim \frac{k_B T}{\gamma}(q_{\max} - q_{\min}) \ .$$

As we let $L \to \infty, q_{min} \to 0$, and $a \to 0, q_{max} \to \infty$, so that

$$\overline{\langle h_x^2 \rangle} \approx \frac{k_B T}{\gamma}\frac{\pi}{a}$$

If we generalize this calculation to d dimensions of space and hence $d-1$ dimensions of the surface we find

$$\begin{aligned}
\langle \overline{h^2} \rangle &\sim \int \frac{d^{d-1}q}{(2\pi)^{d-1}} \frac{k_B T}{\gamma q^2} \sim \frac{k_B T}{\gamma}\int dq \frac{q^{d-2}}{q^2} \\
&\sim \frac{k_B T}{\gamma}\frac{q^{d-3}}{d-3}\Big|_{\mathrm{q_{min}}}^{\mathrm{q_{max}}} \qquad (d>3) \\
&\sim \frac{k_B T}{\gamma}\ln\left(\frac{\mathrm{q_{max}}}{\mathrm{q_{min}}}\right) \sim \frac{k_B T}{\gamma}\ln\left(\frac{L}{a}\right) \qquad (d=3)
\end{aligned}$$

3.3.2 Fluctuations of an interface in a gravitational field

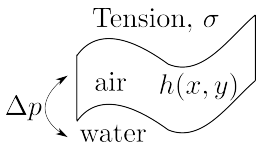

Now we consider a two-dimensional interface endowed with surface tension and in a gravitational field, with a density difference $\Delta\rho$ between the fluids on either side. Once again we expand the surface deformation

$$h(\mathbf{r}) = \sum_q \mathrm{e}^{-i\mathbf{q}\cdot\mathbf{r}}\hat{h}(\mathbf{q})$$

The quadratic energy functional is

$$\begin{aligned}
E &= \frac{1}{2}\int\int dxdy\left[\sigma(\nabla h)^2 + \Delta\rho g h^2\right] \\
&= \frac{\sigma A}{2}\sum_{\mathbf{q}}(q^2 + l_c^{-2})|\hat{h}(\mathbf{q})|^2
\end{aligned}$$

where l_c is once again the capillary length. Again by equipartition we find

$$\langle|\hat{h}(\mathbf{q})|^2\rangle = \frac{k_B T}{\sigma A}\frac{1}{l_c^{-2} + q^2} \ .$$

This shows that the capillary length provides a cutoff on what would otherwise be divergent fluctuation amplitudes as $q \to 0$.

Introducing both large-scale and small-scale cutoffs, the average variance of the displacement field is

$$\begin{aligned}\overline{\langle h^2 \rangle} =& \frac{k_B T}{2\pi\sigma} \int \frac{qdq}{l_c^{-2} + q^2} \\ & \frac{k_B T}{4\pi\sigma} \ln \left[\frac{1 + 2\left(\pi l_c / l\right)^2}{1 + 2\left(\pi l_c / L\right)^2} \right]\end{aligned}$$

In the thermodynamic limit ($L \to \infty$), which is now possible at finite g,

$$\langle \overline{h^2} \rangle \sim \frac{k_B T}{4\pi\sigma} \ln \left[1 + 2 \left(\frac{\pi l_c}{l} \right)^2 \right]$$

It is clear, with $k_B T \sim 10^{-14}$ erg and $\sigma \sim 50$ erg/cm^2 that even if $l_c / l \sim 10^7$ the fluctuations are still on the molecular scale.

3.4 Brownian Motion and Diffusion

3.4.1 Brownian particle in harmonic force field

Brownian motion can be investigated in modern laser trapping systems, first invented in the 1970's at Bell Labs (Ashkin, 1970) The focus beam naturally converges on a small diffraction limited region:

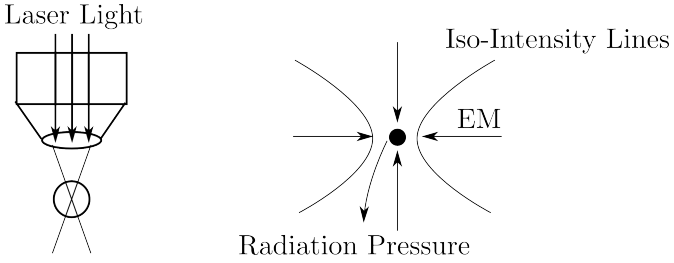

Radiation pressure acts to push the dielectric particle along the optical path, while gradients in the electric field magnitude all point toward the beam waist. If those gradients are sufficiently large there will be a stable trapping potential, which will be harmonic for small displacements. Note that the general result that a dielectric object moves to regions of higher electric field is applicable here as long as one recognizes that the typical microspheres have higher dielectric constants than water *at optical frequencies*, while their DC values are smaller than that of water.

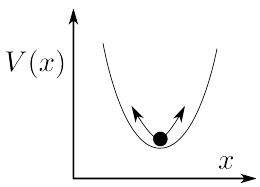

Assuming that the trapping potential is quadratic in lateral displacements x, the overdamped equation of motion of a microsphere in the trap is

$$\zeta \dot{x} = -kx + \eta(t) \ ,$$

where $\eta(t)$ is a random force. For μm sized spheres and moderate lasers, $k \sim 10$ fN/nm, and the relaxation time scale τ in the well comes from the spring constant and drag coefficient:$\tau = \zeta/k \sim 4$ ms (see below). The scale of the trap stiffness implies that submicron displacements correspond to pN forces. Thus, attaching spheres onto motor proteins allows the stall force (typically several pN) of the motor to be determined from a *force clamp*.

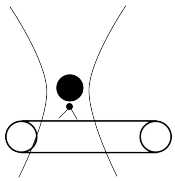

There are two levels at which we can "solve" the Langevin equation. For any particular realization of the random noise $\xi(t)$ we can write down $x(t)$ directly. But we are also interested in *averages over realizations* of the noise, suitable to compare with experimental observations. In the first case, if we rescale the noise term the equation is

$$\dot{x} + \frac{1}{\tau} x = \xi(t)$$

We recognize an integrating factor:

$$e^{t/\tau} \left(\dot{x} + \frac{1}{\tau} x \right) = e^{t/\tau} \xi(t)$$

This allows a direct solution for any particular noise

$$x(t) - x_0 e^{-t/\tau} = \int_0^t dt' e^{-(t-t')/\tau} \xi(t')$$

Now we find averages over realizations of the noise.

$$\langle x(t) - x_0 e^{-t/\tau} \rangle = \int_0^t dt' e^{-(t-t')/\tau} \langle \xi(t') \rangle = 0 \ .$$

Clearly, the average of the noise must vanish for an unbiased system, so we conclude

$$\langle x(t) \rangle = x_0 e^{-t/\tau} \ .$$

Now we consider the square of the deviation from simple relaxation:

$$\langle (x(t) - x_0 e^{-t/\tau})^2 \rangle = \int_0^t dt' \int_0^t dt'' e^{-(t-t'')/\tau} e^{-(t-t')/\tau} \langle \xi(t') \xi(t'') \rangle$$

The crucial assumption of the Langevin approach is that the correlation inside the integral is a sharply-peaked function of $|t' - t''|$, decaying much faster than any relevant timescale of the particle. Calling this function $\phi(t' - t'')$, we make the change of variables ($J = 1/2$)

$$s = t' + t'' \qquad\qquad q = t' - t''$$

The right hand side of the previous equation will then be (extending limits to $\pm\infty$)

$$\int_0^t dt' \int_0^t dt'' e^{-(t-t'')/\tau} e^{-(t-t')/\tau} \langle \xi(t')\xi(t'') \rangle$$
$$= \frac{1}{2} e^{-2t/\tau} \int_0^{2t} ds e^{s/\tau} \int_{-\infty}^{\infty} dq \phi(q) \ ,$$

where the final integral is just a number (Γ). The average deviation squared is then

$$\langle (x(t) - x_0 e^{-t/\tau})^2 \rangle = \frac{\Gamma\tau}{2}(1 - e^{-2t/\tau})$$

In the long time limit ($t/\tau \to \infty$)

$$\langle (x(t) - x_0 e^{-t/\tau})^2 \rangle = \langle x(t)^2 \rangle = \frac{\Gamma\tau}{2}$$

However, using the equipartition argument

$$\frac{1}{2} k \langle x^2 \rangle = \frac{1}{2} k_B T \qquad\qquad \Rightarrow \qquad\qquad \Gamma = \frac{2k_B T}{\zeta}$$

Logically, we assume that there is a δ correlation for the noise:

$$\langle \xi(t)\xi(t') \rangle = \frac{2k_B T}{\zeta} \delta(t - t')$$

A further test of the result is to examine the short-time behaviour of the variance in the displacement. If we assume $x_0 = 0$ and $t/\tau \ll 1$, then

$$\langle x^2(t) \rangle \sim \frac{\Gamma\tau}{2} \left(\frac{2t}{\tau} + \dots \right) \sim \frac{2k_B T}{\zeta} t + \cdots$$

which is just a random walk in 1D ($\langle x^2 \rangle = 2Dt$). Thus

$$D = \frac{k_B T}{\zeta}$$

and the Stokes-Einstein relation is recovered. The fun calculation is to do this in the presence of inertia (see examples sheet).

The diffusion coefficient is just the average

$$D = \lim_{t \to \infty} \frac{1}{6t} \langle (\mathbf{r}(t) - \mathbf{r}(0))^2 \rangle$$

$$\text{where} \quad \mathbf{r}(t) = \mathbf{r}(0) + \int \mathbf{u}(t')dt'$$

This holds provided that the correlation of velocities ($\langle \mathbf{u}(t') \cdot \mathbf{u}(t'') \rangle$ falls off fast enough. If τ is the time scale for that decay and u is a typical velocity, then

$$D = \frac{1}{3} \int_0^\infty dt \langle \mathbf{u}(t) \cdot \mathbf{u}(0) \rangle \sim u^2 \tau$$

We can apply this to the run-and-tumble locomotion of bacteria. For *E. coli* the average velocity is about 20 μm/s, and the bacteria executes 1s of movement before randomly changing direction. This yields a diffusion coefficient of $4 \times 10^{-6} \text{cm}^2/\text{s}$, which is approximately the diffusion coefficient of a small molecule in water.

3.5 Brownian Motion and Polymer Statistics

Consider an arbitrary free polymer with each segment labeled as $\mathbf{r}_n$. Each segment is followed by another random segment of equal length ($|\boldsymbol{\zeta}_n| = b$)

$$\mathbf{r}_{n+1} = \mathbf{r}_n + \boldsymbol{\zeta}_n$$

The end-to-end displacement of the polymer is

$$\mathbf{r}_N - \mathbf{r}_0 = \sum_{n=1}^{N} \boldsymbol{\zeta}_n \qquad \langle \mathbf{r}_N - \mathbf{r}_0 \rangle = \sum_{n=1}^{N} \langle \boldsymbol{\zeta}_n \rangle = 0$$

by symmetry. The average of the displacement squared is

$$\langle (\mathbf{r}_N - \mathbf{r}_0)^2 \rangle = \sum_{m=1}^{N} \sum_{n=1}^{N} \langle \boldsymbol{\zeta}_m \cdot \boldsymbol{\zeta}_n \rangle = \sum_{m=1}^{N} \sum_{n=1}^{N} \delta_{mn} b^2 = Nb^2$$

The similarity with the Langevin formalism is apparent.

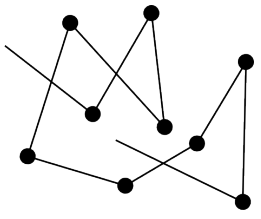

Let us try to formulate the problem more generally. defining the probability that a polymer will have segment positions at $\{\mathbf{r}_k\}$ as

$$p = \frac{1}{Z} G(\{\mathbf{r}_k\}) \qquad G = \mathrm{e}^{-\beta U(\{\mathbf{r}_k\})}$$

Let us suppose that the energy is a sum of near-neighbor interactions plus a contribution from some external potential,

$$U(\{\mathbf{r}_k\}) = \sum_{j=1}^{N} U_j(\mathbf{r}_{j-1}, \mathbf{r}_j) + W(\{\mathbf{r}_k\})$$

When $W = 0$, this is just a random flight model. Either way, this is a local model for the total energy, as it only relies on nearest neighbor interactions. We then introduce

$$\tau_j(\mathbf{R}_j) = \exp[-\beta U_j(\mathbf{R}_j)] \quad \text{where} \quad \mathbf{R}_j = \mathbf{r}_j - \mathbf{r}_{j-1}$$

and we can take it to be normalized ($\int d\mathbf{R}_j \tau(\mathbf{R}_j) = 1$).

We now define the fixed end-to-end-vector partition function as an integral over all degrees of freedom for which the end position is $\mathbf{R}$ (start at origin):

$$G(\mathbf{R}; N) = \int d\{\mathbf{R}_k\} G(\{\mathbf{R}_k\}) \delta(\mathbf{r}_N - \mathbf{R}) = \int d\{\mathbf{R}_k\} \prod_{j=1}^{N} \tau(\mathbf{R}_j) \delta\left(\sum_{j=1}^{N} \mathbf{R}_j - \mathbf{R}\right)$$

We shall see that molecular-level details will be coarse-grained away...

As an example, consider τ for a fixed-length segment:

$$\tau(\mathbf{R}_j) = \frac{1}{4\pi\ell^2} \delta\left(|\mathbf{R}_j| - \ell\right)$$

Now we use an integral representation of a delta function,

$$\delta\left(\sum_{j=1}^{N} \mathbf{R}_j - \mathbf{R}\right) = \int \frac{d^3k}{(2\pi)^3} \mathrm{e}^{i\mathbf{k}\cdot(\sum \mathbf{R}_j - \mathbf{R})}$$

The distribution function is then

$$G = \int \frac{d^3k}{(2\pi)^3} e^{-i\mathbf{k}\cdot\mathbf{R}} \left[\int d\mathbf{R}_j \tau(\mathbf{R}_j) \exp(i\mathbf{k}\cdot\mathbf{R}_j)\right]^N$$

The bracketed term is a characteristic function $K(\mathbf{k}; N)$, and in this particular case is

$$K(\mathbf{k}; N) = \left(\frac{\sin(k\ell)}{k\ell}\right)^N$$

We expect N to be on the order of R^2 if dominated by diffusive behavior, and thus quite large. In the limit of large N (small k)

$$K(\mathbf{k}; N) \approx \left(1 - \frac{k^2\ell^2}{6} + \dots\right)^N \sim \exp(-Nk^2\ell^2/6)$$

Inverse Fourier transforming,

$$\begin{aligned} G(\mathbf{R}; N) &= \int \frac{d^3k}{(2\pi)^3} \exp(-i\mathbf{k}\cdot\mathbf{R}) \exp(-N\ell^2k^2/6) \\ &= \left(\frac{3}{2\pi\ell^2 N}\right)^{3/2} \exp\left(\frac{-3R^2}{2N\ell^2}\right) \end{aligned}$$

This Gaussian distributiion is nearly universal - its existence depends primarily on the underlying bond length distribution having a finite second moment, so the central limit theorem holds. In the more general case, the characteristic length ℓ derives from the second moment of that distribution.

3.5.1 Self-avoidance

We saw previously that the probability distribution of the end-to-end vector $\mathbf{R}$ has the Gaussian form

$$P(R) \sim \mathrm{e}^{-3R^2/2N\ell^2} \ .$$

We are free to interpret the argument of the exponential as the Boltzmann factor of an effective free energy $F(R)$,

$$F(R) = -k_B T \ln P(R) = k_B T \frac{3R^2}{2N\ell^2}$$

which has the form of a (Hookean) entropic spring, with a minimum at $R = 0$. It costs entropy to extend the chain.

Let us now consider how excluded-volume interactions change this free energy. We imagine that there is a pairwise interaction of the form

$$\frac{1}{2} v k_B T \int_0^N dn \int_0^N dm \ \delta(\mathbf{R}_n - \mathbf{R}_m)$$

where we have called the amplitude of the interaction vk_BT for convenience, and abstracted it into a delta function potential.

3.5.2 Flory Theory

Using the mean-field arguments of van der Waals, we estimate the contribution of these interactions to the free energy as

$$v k_B T \cdot N \cdot \frac{N}{R^3} \sim k_B T \frac{v N^2}{R^3}$$

where the local segment concentration is N/R^3 (in three dimensions). The total free energy in this *Flory theory* is thus

$$F_{\mathrm{tot}} = k_B T \left[\frac{3R^2}{2N\ell^2} + \frac{vN^2}{R^3} \right]$$

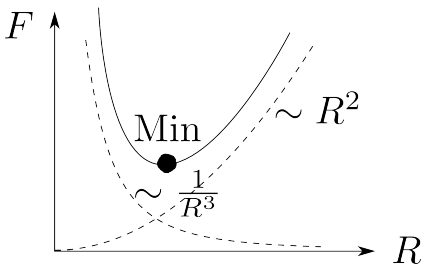

We see a competition between entropy, which favours the smallest R, and excluded-volume effects that tend to swell the chain. Differentiating to find the optimum, R^*, we obtain

$$R^* \sim N^{3/5}$$

Note: $3/5 > 1/2$, so excluded-volume interactions
have swollen the chain from its ideal random-walk size.

Generalizing this to d-dimensions, the only change is that the local concentration is N/R^d, so the balance of terms is

$$\frac{R^2}{N} \sim \frac{N^2}{R^d} \Rightarrow R^{d+2} \sim N^3 \Rightarrow R \sim N^{3/(d+2)}$$

Thus, Flory theory predicts the exponent values

$$R \sim N^{\nu} \qquad \nu = \frac{3}{d+2}$$

This relation is remarkably accurate:

$d = 1$	$R \sim N$	correct
$d = 2$	$R \sim N^{3/4}$	exact (solved)
$d = 3$	$R \sim N^{3/5}$	numerical solution (0.589)
$d = 4$	$R \sim N^{1/2}$	correct
$d > 4$	$R \sim N^{3/(d+2)}$	wrong (should be $N^{1/2}$)

Geometry and Elasticity

4

4.1 Curve Dynamics

In this section we will study some elementary aspects of the motion of curves and learn how to describe elastically-driven motions of filamentary objects in a viscous fluid. First, some differential geometry. Consider a curve $\mathbf{r}(\alpha)$ in a plane that is parameterized by $\alpha \in (0,1)$. The differential of arclength is

$$ds = |d\mathbf{r}| = \sqrt{g}d\alpha \qquad g = \mathbf{r}_\alpha \cdot \mathbf{r}_\alpha$$

with $\mathbf{r}_\alpha \equiv \partial\mathbf{r}/\partial\alpha$ and g is the metric.

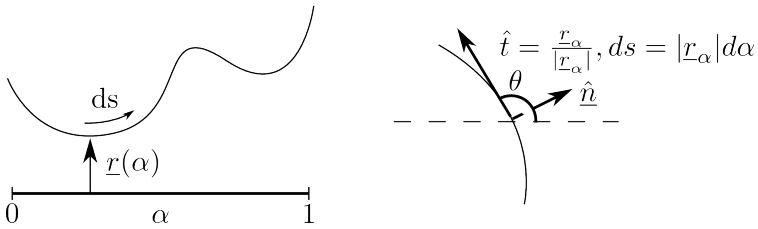

The unit tangent to the curve is

$$\hat{\mathbf{t}} = \frac{\mathbf{r}_\alpha}{\sqrt{g}}$$

The tangent and normal vectors rotate as we move along the curve according to the *Frenet-Serret* equations

$$\frac{\partial}{\partial s}\begin{pmatrix}\hat{\mathbf{t}}\\ \hat{\mathbf{n}}\end{pmatrix} = \begin{pmatrix}0 & -\kappa\\ \kappa & 0\end{pmatrix}\begin{pmatrix}\hat{\mathbf{t}}\\ \hat{\mathbf{n}}\end{pmatrix}$$

where κ is the curvature.

If the tangent vector makes an angle θ with respect to a fixed axis (e.g., the x-axis), then it is easy to show that

$$\kappa = \frac{\partial\theta}{\partial s} \quad \text{where in general} \quad \frac{\partial}{\partial s} = \frac{1}{\sqrt{g}}\frac{\partial}{\partial\alpha}$$

In the "Monge representation", where we have a function $h(x)$ with no overhangs as a function of an external parameter x,

$$\begin{aligned}\mathbf{r}(x) &= x\hat{\mathbf{e}}_\mathbf{x} + h(x)\hat{\mathbf{e}}_\mathbf{y}\\ \mathbf{r}_x &= \hat{\mathbf{e}}_\mathbf{x} + h_x\hat{\mathbf{e}}_\mathbf{y}\\ \hat{\mathbf{t}} &= \left[\hat{\mathbf{e}}_\mathbf{x} + h_x\hat{\mathbf{e}}_\mathbf{y}\right]/\sqrt{1+h_x^2}\end{aligned}$$

$$\text{so} \qquad \theta = \tan^{-1} h_x$$

and the curvature is

$$\kappa = \frac{h_{xx}}{(1+h_x^2)^{3/2}} \simeq h_{xx}$$

Let us look at the example of an elastic filament, weakly deformed, to understand a bit more about curvature and variational principles. The simplest elastic energy is (Landau & Lifshitz, etc.)

$$E = \frac{A}{2}\int_0^L ds\kappa^2$$

where A is an elastic modulus and s is arclength. Note that the units of A are energy·length, so we can always express A as k_BTL_p, where L_p is the *persistence length*. This has physical meaning in that if the curvature $\kappa \sim 1/R \sim 1/L$ then $E \sim A \cdot L \cdot 1/L^2 \sim A/L$, and if we ask that such bending cost k_BT, then the length scale is on which this occurs is $L \sim A/k_BT$. Thus the persistence length is the length over which thermal energy can induce a filament-length bend.

DNA	$L_p \sim 50$ nm (~ 150 base pairs)
actin	$L_p \sim 10 - 15$ μm
microtubules	$L_p \sim 5$ mm

Note the definition of the Young's modulus:

$$\frac{\text{Force}}{\text{area}} = E\frac{\Delta L}{L}$$

and a force/area is an energy/volume. Since $[A] = \text{energy} \cdot \text{length}$, we conclude

$$A \sim E \cdot \text{radius}^4$$

Returning to the elastic energy if the slope is small everywhere, we can approximate this as

$$E \simeq \frac{A}{2}\int_0^L dx h_{xx}^2$$

To find equilibria of this energy functional we need to look at the variation δE when h is changed by δh. Repeatedly integrating by parts,
we find

$$\delta E = A\int dx h_{xx}\delta h_{xx} = A\left\{h_{xx}\delta h_x\Big|_0^L - \int dx h_{3x}\delta h_x\right\}$$
$$= A\left\{h_{xx}\delta h_x\Big|_0^L - h_{xxx}\delta h\Big|_0^L + \int dx h_{4x}\delta h\right\}$$

This implies that the functional derivative of E is

$$\frac{\delta E}{\delta h} = Ah_{4x}$$

If the "surface" terms vanish for arbitrary δh and δh_x then we require

$$\begin{aligned} h_{xx}(0) = h_{xx}(L) = 0 \qquad & [Ah_{xx}] = \text{energy} = \text{torque} \\ h_{3x}(0) = h_{3x}(L) = 0 \qquad & [Ah_{3x}] = \text{energy/length} = \text{force} \end{aligned}$$

These are the *natural boundary conditions* of no torque and no force at the (free) ends. If this is the case, the ∂_{4x} is a self-adjoint operator and its eigenfunctions are real. These are eigenfunctions satisfying

$$AW_{4x} = k^4 W$$

just as $\sin qx$ and $\cos qx$ are eigenfunctions satisfying $f_{xx} = -q^2 f$.

A simple superposition of $\sin kx$ and $\cos kx$ will not work, as this can not allow successive derivatives to vanish. Instead,

$$W(x) = A \sin kx + B \cos kx + D \sinh kx + E \cosh kx$$

An exercise for the student is to show that the boundary conditions imply

$$\cos kL \cosh kL = 1$$

This yields an infinite discrete set of wavenumbers k analogous to the trigonometric numbers $n\pi/L$.
If we express $h(x)$ as a sum of biharmonic eigenfunctions

$$h(x) = \sum_n a_n W^{(n)}(x) \qquad \text{then} \qquad h_{4x} = \sum_n a_n \lambda_n W^{(n)}(x)$$

where λ_n is the nth eigenvalue.

This impliest that the bending energy can be separated into modes:

$$\begin{aligned} \frac{A}{2} \int dx h_{xx}^2 = \frac{A}{2} \int dx h h_{4x} = \frac{A}{2} \int dx \sum_m \sum_n a_m a_n \lambda_n W^{(m)} W^{(n)} \\ = \frac{A}{2} \sum_n \lambda_n a_n^2 \end{aligned}$$

by the orthogonality of the Ws (and their assumed normalization). And we can compute the variance:

$$h^2(x) = \sum_m \sum_n a_m a_n W^{(m)}(x) W^{(n)}(x)$$

and, since the a_m are independent, Gaussianly distributed variables,

$$\langle h^2(x) \rangle = \frac{k_B T}{A} \sum_n \frac{W^{(n)}(x)^2}{\lambda_n}$$

Here is a graph of the first few normalized eigenfunctions.

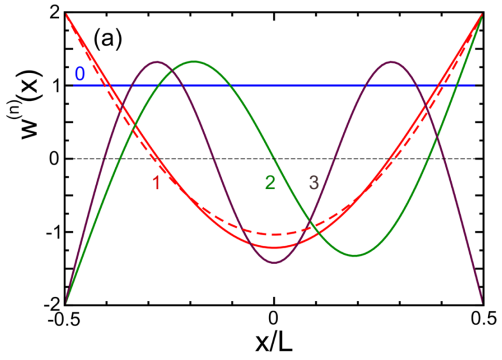

The above result on fluctuations has recently been tested in experiments on actin filaments in microfluidic devices. As shown below, a cross-flow geometry can be used to trap individual filaments at the stagnation point. Under extensile flow the filament is stable and its fluctuations are decreased by tension created in the filament.

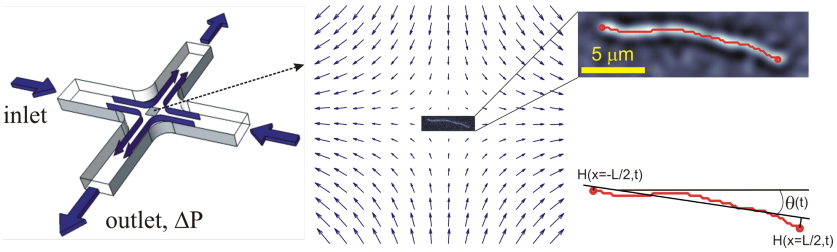

The variance, normalized by its endpoint values, displays a 'W' shape that is just the square of the first mode, the minima associated with the zeroes of that function.

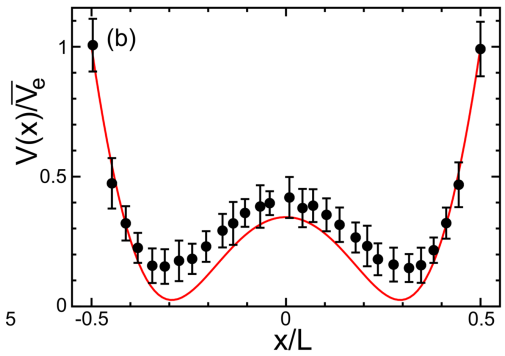

Under compression the filament buckles and reorients to the stable direction. As a function of increasing tension one finds higher-order buckling modes:

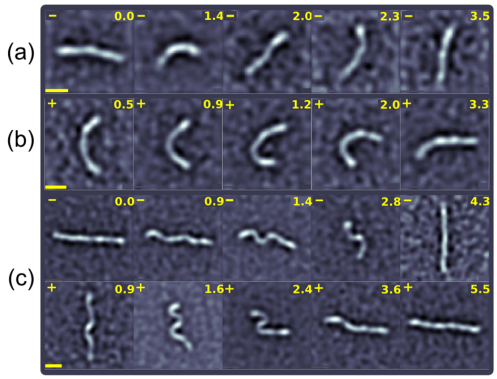

4.1.1 Dissipation

We need first to incorporate dissipative contributions into the usual Lagrangian formulation of classical dynamics. Assume the Lagrangian is

$$\mathcal{L}(q,\dot{q}) = T - V$$

The minimum action principle is

$$\delta S = 0, \quad S = \int dt\mathcal{L} \quad \Rightarrow \quad \frac{d}{dt}\frac{\partial \mathcal{L}}{\partial \dot{q}} - \frac{\partial \mathcal{L}}{\partial q} = 0$$

With a kinetic energy term $T = (1/2)m\dot{q}^2$ the Euler-Lagrange equation is

$$m\ddot{q} = -\frac{\partial V}{\partial q} \ .$$

In the limit of zero inertia (vanishing Reynolds number), simply dropping the kinetic energy term leaves us with no dynamics at all, so we need to introduce a *generalized force* associated with dissipation. If the viscous force is $\zeta\dot{q}$, the rate of dissipation is $\zeta\dot{q}^2$. So, we introduce the *Rayleigh dissipation function*

$$\mathcal{R} = \frac{\zeta}{2}\dot{q}^2 \ ,$$

proportional to the rate of dissipation. The new variational principle is

$$\frac{d}{dt}\frac{\partial \mathcal{L}}{\partial \dot{q}} - \frac{\partial \mathcal{L}}{\partial q} = -\frac{\partial \mathcal{R}}{\partial \dot{q}} = -\zeta\dot{q}$$

In the overdamped limit we then have the Aristotelian law

$$\zeta\dot{q} = -\frac{\partial U}{\partial q}$$

The simplest generalization of this to a moving curve involves a local drag coefficient, call it Γ, such that

$$\mathcal{R} = \frac{\Gamma}{2}\int d\alpha\sqrt{g}\mathbf{r}_t^2 \quad \text{with} \quad -\frac{\delta \mathcal{R}}{\delta \mathbf{r}_t} = -\Gamma\sqrt{g}\mathbf{r}_t \ ,$$

and by recognizing that the potential energy function V is really our generalized energy functional E for the curve we arrive at the equation of motion

$$\Gamma \mathbf{r}_t = -\frac{1}{\sqrt{g}} \frac{\delta \mathcal{E}}{\delta \mathbf{r}} \ .$$

The simplest example of an energy functional is the length L of a curve,

$$L = \int_0^1 d\alpha \sqrt{g}$$

This is a function of $\mathbf{r}_\alpha$ alone, so

$$-\frac{1}{\sqrt{g}} \frac{\delta L}{\delta \mathbf{r}} = \frac{1}{\sqrt{g}} \frac{\partial}{\partial \alpha} \left[\frac{1}{2} \frac{1}{\sqrt{g}} 2\mathbf{r}_\alpha \right] = \frac{\partial}{\partial s} \hat{\mathbf{t}} = -\kappa \hat{\mathbf{n}} \ ,$$

so restoring force from line tension is proportional to the curvature.

A second calculation involves the area A enclosed by a (closed) curve,

$$A = \frac{1}{2} \int_0^1 d\alpha \mathbf{r} \times \mathbf{r}_\alpha$$

where the cross product is here interpreted as a scalar: $(\mathbf{a} \times \mathbf{b})_i = \epsilon_{ij} \mathbf{a}_i \mathbf{b}_j$. A short calculation shows that

$$-\frac{1}{\sqrt{g}} \frac{\delta A}{\delta \mathbf{r}} = \hat{\mathbf{n}}$$

4.2 Elastohydrodynamics

We recall that the viscous drag on a sphere of radius a in low Reynolds number flow is given by the Stokes formula

$$\mathbf{F} = \zeta \mathbf{r}_t \quad \zeta = 6\pi\eta a$$

For a long, slender object of length L and radius a, the calculation of the drag is a complicated nonlocal problem, but often the dominant behaviour is well-described by the introduction of local drag coefficients (so-called *Resistive Force Theory*) $\zeta_\perp$, $\zeta_\parallel$, and ζ_r for motion perpendicular and parallel to the rod axis, and for rotational motion. These are

$$\zeta_\perp = 2\zeta_\parallel = \frac{4\pi\eta}{\ln(L/2a) + c} \quad \zeta_r = 4\pi\eta a^2$$

where for rotation motion there is a balance between the moment m and angular frequency of the form $m = \zeta_r \omega$. With this anisotropic drag law, the equation of motion of the filament would be

$$\left(\zeta_\perp \hat{\mathbf{n}}\hat{\mathbf{n}} + \zeta_\parallel \hat{\mathbf{t}}\hat{\mathbf{t}} \right) \cdot \mathbf{r}_t = -\frac{1}{\sqrt{g}} \frac{\delta \mathcal{E}}{\delta \mathbf{r}}$$

These are two pedagogical problems involving viscous fluids driven by the motion of a boundary parallel to itself. Starting with the Navier-Stokes equation

$$\rho\left(\mathbf{u}_t + \mathbf{u}\cdot\nabla\mathbf{u}\right) = -\nabla p + \eta\nabla^2\mathbf{u}$$

we recognize for wall-driven flow that the nonlinear term vanishes by symmetry, and we can ignore the pressure gradient. As the velocity will be of the form $\mathbf{u} = u(y)\hat{\mathbf{e}}_x$, the problem boils down to the solution of the diffusion equation

$$u_t = \nu u_{yy}$$

We will consider two situations:

(1) Starting at $t = 0$, the wall begins to move with velocity U in the x-direction. Only length scale is $\sqrt{\nu t}$.

(2) The wall's velocity oscillates, as $U\mathrm{e}^{i\omega t}$. Only length scale is $\sqrt{\nu/\omega}$.

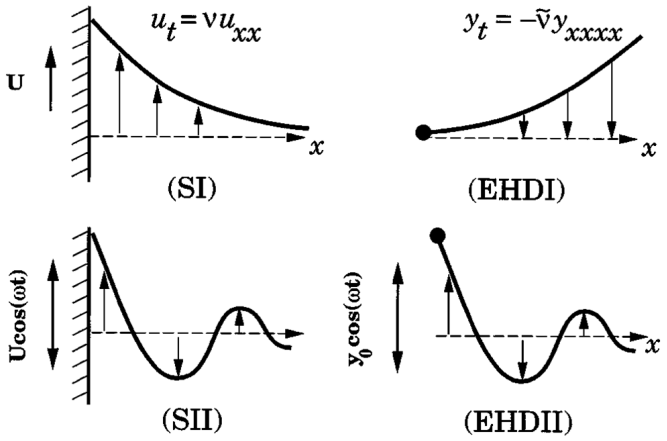

Searching for a similarity solution of the form

$$u = Uf\left(\frac{y}{\sqrt{\nu t}}\right) \quad u_{yy} = Uf_{\xi\xi}(\xi)\left(\frac{1}{\nu t}\right) \quad u_t = Uf_\xi(\xi)\left(\frac{-1}{2t}\xi\right)$$

$u_t = \nu u_{yy}$ then becomes an ODE in ξ

$$f_{\xi\xi} = -\frac{1}{2}\xi f_\xi$$

Boundary conditions: $f(0) = 1$, $f(\infty) = 0$. Letting $g = f_\xi$

$$g_\xi \frac{-1}{2}\xi g \qquad \Longrightarrow \qquad g = Ae^{-\xi^2/4}\ .$$

Invoking boundary conditions we obtain

$$f(\xi) = 1 - \frac{1}{\sqrt{\pi}}\int_0^\xi d\xi' e^{-\xi'^2/4}$$

and thus the similarity solution exists. The velocity is

$$\frac{u}{U} = 1 - \mathrm{erf}\left(y/2\sqrt{\nu t}\right)$$

For the oscillating Stokes problem, we consider the situation post-transients, where we expect a similarity solution of the form

$$u = U\mathrm{e}^{i\omega t}F\left(\frac{y}{\sqrt{\nu/\omega}}\right)$$

and the PDE becomes an ODE in $\xi = y/\sqrt{\nu/\omega}$

$$F_{\xi\xi} = iF$$

Looking for exponential solutions, $F \sim \mathrm{e}^{\lambda\xi}$ gives

$$\lambda^2 = i \qquad \lambda_\pm = \pm\frac{(1+i)}{\sqrt{2}}$$

$$\text{So} \qquad F = \mathrm{e}^{-\xi/\sqrt{2}}\mathrm{e}^{-i\xi/\sqrt{2}} \ .$$

And we take the real part, giving the damped traveling-wave solution

$$u = U\mathrm{e}^{-\xi/\sqrt{2}}\cos\left(\frac{\xi}{\sqrt{2}} - \omega t\right) \ .$$

For the oscillating EHD problem, the PDE governing small-amplitude deviations of the filament is

$$\zeta_\perp h_t = -Ah_{xxxx}$$

and we will consider the situation post-transient in which the left-hand side is forced as $h(0,t) = h_0\cos(\omega t)$, $h_{xx}(0,t) = 0$ and the distant end is free. Dimensional analysis shows there is a new elastohydrodynamic penetration length

$$\ell(\omega) = \left(\frac{A}{\zeta\omega}\right)^{1/4} \ .$$

We expect a similarity solution of the form

$$h = h_0\mathrm{Re}\left\{\mathrm{e}^{i\omega t}F\left(\frac{x}{\ell(\omega)}\right)\right\} \qquad \rightarrow \qquad F_{\xi\xi\xi\xi} = -iF$$

Looking for exponential solutions, $F \sim \mathrm{e}^{\lambda\xi}$ gives $\lambda^4 = -i$, and when the dust settles we have ($C_8 = \cos(\pi/8)$, $S_8 = \sin(\pi/8)$),

$$h(x,t) = \frac{1}{2}h_0\left\{\mathrm{e}^{-C_8\xi}\cos\left(\omega t + S_8\xi\right) + \mathrm{e}^{-S_8\xi}\cos\left(\omega t - C_8\xi\right)\right\}$$

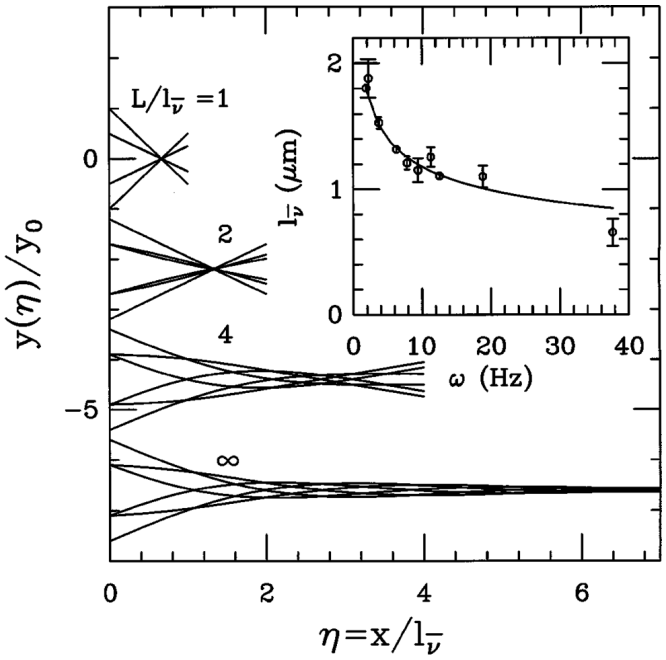

Let us estimate the EH penetration length. Writing $A = k_B T L_p$ and taking $L_p \sim 10$ μm (actin), and measuring frequency in Hz, we find

$$\ell(\omega) \sim \left(\frac{4 \times 10^{-14} \cdot 10^{-3}}{4\pi \cdot 10^{-2} \cdot 1} \right)^{1/4} \sim \frac{\text{a few microns}}{\omega^{1/4}}$$

So, if we oscillate an actin filament at many Hz we will create undulations on a scale smaller than L_p. This can be done by optical trapping.

A second point (Machin, 1958), is that if we examine the shapes of undulating filaments that are end-actuated, the amplitudes of the subsequent peaks of the waveform are very small, totally unlike what is seen with e.g. sperm cells. This led Machin to the conclusion that eukaryotic flagella must not be actuated simply at their ends, but throughout their length. This is true!

Returning to our two-dimensional problems of curve motion, we observe that the general equation of motion can be written as

$$\mathbf{r}_t = U\hat{\mathbf{n}} + W\hat{\mathbf{t}}$$

where $U = U(\mathbf{r}, \kappa, \ldots)$ and $W = W(\mathbf{r}, \kappa, \ldots)$ are the normal and tangential velocities. This is an *intrinsic* equation of motion. If we calculate the time derivative of the tangent vector we obtain

$$\frac{\partial \hat{\mathbf{t}}}{\partial t} = \frac{\partial}{\partial t}\frac{1}{\sqrt{g}}\mathbf{r}_\alpha = \frac{\mathbf{r}_{\alpha t}}{\sqrt{g}} - \frac{1}{2g^{3/2}} 2\mathbf{r}_\alpha \cdot \mathbf{r}_{\alpha t} = \partial_s \mathbf{r}_t - \hat{\mathbf{t}}\hat{\mathbf{t}} \cdot \partial_s \mathbf{r}_t$$

Now, writing

$$\hat{\mathbf{t}} = \cos\theta \hat{\mathbf{e}}_x + \sin\theta \hat{\mathbf{e}}_y$$
$$\hat{\mathbf{n}} = \sin\theta \hat{\mathbf{e}}_x - \cos\theta \hat{\mathbf{e}}_y$$

we see that $\partial\hat{\mathbf{t}}/\partial t = -\theta_t\hat{\mathbf{n}}$, so

$$\theta_t = -U_s + \kappa W$$

With a bit more work it is straightforward to show that the curvature itself obeys the PDE

$$\kappa_t = -\left(\partial_{ss} + \kappa^2\right) U + \kappa_s W \ .$$

These two results indicate that there are intrinsic *geometrical nonlinearities* due to the fact that the vector $\mathbf{r}$ and the arclength s are not independent. Note also that in many ways the tangential velocity is something we can choose (like a gauge), as it corresponds to a particular time-dependent parameterization.

Now consider *motion by mean curvature* in the simplest case of 2-D motion,

$$U = -\gamma\kappa \quad \text{and} \quad W = 0 \ .$$

This corresponds to an energy functional $\mathcal{E} = \gamma L$, for which the tangent angle and curvature evolve as

$$\theta_t = -U_s + \kappa W = \gamma\theta_{ss} \ , \quad \kappa_t = \gamma\left(\kappa_{ss} + \kappa^3\right) \ .$$

Since we derived this by a variational principle from the energy functional E, it stands to reason that E is driven downhill. To check this we compute

$$\frac{\partial\mathcal{E}}{\partial t} = \gamma\int d\alpha \frac{1}{2}\frac{1}{\sqrt{g}} 2\mathbf{r}_\alpha \cdot \mathbf{r}_{\alpha t} = \gamma\int ds\hat{\mathbf{t}} \cdot \partial_s\mathbf{r}_t$$

Since $\mathbf{r}_t = -\gamma\kappa\hat{\mathbf{n}}$, $\partial_s\mathbf{r}_t = -\gamma\kappa_s\hat{\mathbf{n}} - \gamma\kappa^2\hat{\mathbf{t}}$, so

$$\frac{\partial\mathcal{E}}{\partial t} = -\gamma^2\int ds\kappa^2 \leq 0$$

Thus, the length is driven downhill (the "curve-shortening equation"). It is easy to show that the area A enclosed by a curve evolves as

$$A_t = \int dsU \quad \text{so, here} \quad A_t = -\gamma\int ds\kappa = -2\pi\gamma \ .$$

So the area vanishes in a finite time!

4.3 Euler Buckling

Here we consider the classic problem of *Euler buckling*, in which an elastic filament subject to thrusting forces at its ends deforms at a critical force.

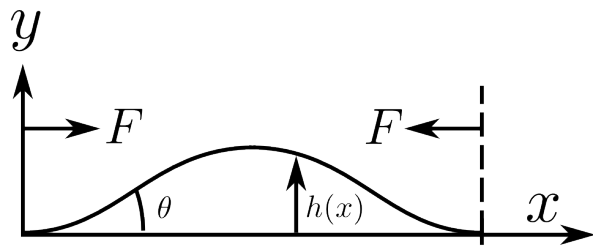

A nice experimental realization of this is the work of Fygenson, *et al.*, in which microtubules were grown inside lipid vesicles and buckled due to the membrane surrounding them:

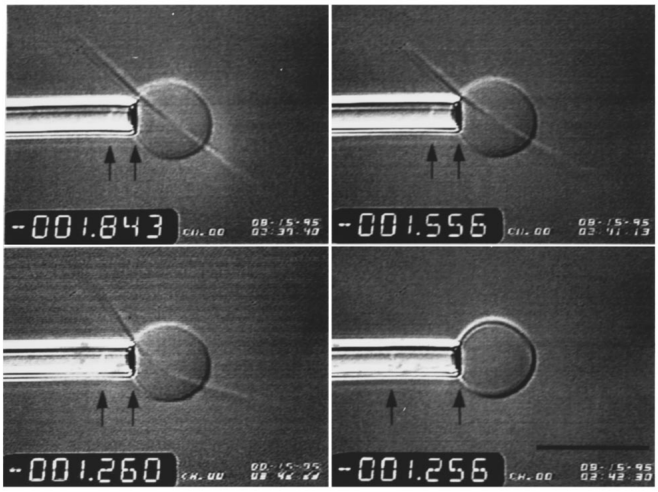

The energy functional associated with this configuration is just

$$\mathcal{E}[\theta] = \int_0^L ds \left[\frac{A}{2}\theta_s^2 + F\cos\theta \right]$$

where the second term represents the work done by the force in moving the end,

$$X(L) - X(0) = \int_0^L \frac{dx}{ds} ds = \int_0^L \cos(\theta(s))$$

where the components of the curve in the x, y directions are just

$$\begin{pmatrix} dx/ds \\ dy/ds \end{pmatrix} = \begin{pmatrix} \cos(\theta(s)) \\ \sin(\theta(s)) \end{pmatrix}$$

The equilibrium condition is

$$\frac{\delta\mathcal{E}}{\delta\theta} = 0 = -\frac{d}{ds}\frac{\partial\cdots}{\partial\theta_s} + \frac{\partial\cdots}{\partial\theta} \quad \rightarrow \quad A\theta_{ss} + F\sin\theta = 0 \ ,$$

otherwise known as the pendulum equation. [Think of $\mathcal{L} = \mathcal{T} - \mathcal{V}$, with $\mathcal{T} = (1/2)m\dot{q}^2$ and $\mathcal{V} = mg(1 - \cos q)$.] Let us consider *clamped* boundary conditions, $\theta(0) = \theta(L) = 0$. We expect a shape with a single bump in the middle, which is a sin function for θ,

$$\theta(s) \simeq a\sin\left(\frac{2\pi s}{L}\right) \ .$$

This will only solve the linearized Euler-Lagrange equation $\theta_{ss} \simeq -(F/A)\theta$ provided

$$\frac{F}{A} = \frac{4\pi^2}{L^2} \quad \text{or} \quad F = F_c = \frac{4\pi^2 A}{L^2} = 4\pi^2 \left(\frac{k_B T}{L_p}\right)\left(\frac{L_p}{L}\right)^2 .$$

Consider microtubules. $L_p \sim 0.1$ cm, and take $L \sim 20$ μm $= 2 \times 10^{-3}$ cm (as in expt). Then $L_p/L \sim 50$ and

$$F_c \sim 40 \cdot \left(\frac{4 \times 10^{-14}}{0.1}\right) \cdot (50)^2 \simeq 0.5 \text{ pN}$$

Near the bifurcation, we expect that nonlinearities will stabilize the buckled shape at some finite amplitude. If we continue with the single-mode approximation and variational approach we seek an energy functional of higher-than-quadratic order to achieve this. Expand the force near F_c and the geometric term in the energy,

$$F = F_c(1+f) \qquad \cos\theta = 1 - \frac{1}{2}\theta^2 + \frac{\theta^4}{24} + \dots$$

The energy functional is then

$$\begin{aligned}\mathcal{E}[\theta] &\simeq \int_0^L \left[\frac{A}{2}\theta_s^2 + F_c(1+f)\left(1 - \frac{1}{2}\theta + \frac{\theta^4}{24} + \dots\right)\right] \\ &\simeq \mathcal{E}_c + F_c(1+f)L + \frac{F_c L}{2}\left[\frac{-fa^2}{2} + \frac{a^4}{32} + \dots\right]\end{aligned}$$

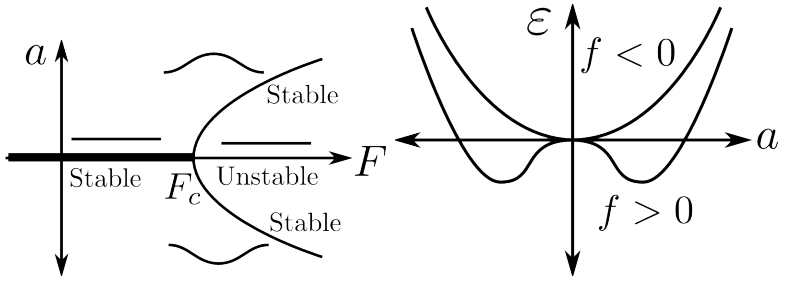

Thus, we have a *Landau theory* for the bifurcation, in which the relevant part of the energy functional has the form

$$\mathcal{E}[\theta] \simeq \frac{F_c L}{2}\left[\frac{-fa^2}{2} + \frac{a^4}{32} + \dots\right]$$

When $f < 0$ (below the bifurcation), there is a single minimum at $a = 0$, while above ($f > 0$) there are two minimum at

$$a = \pm\sqrt{8f}$$

the characteristic of a *pitchfork bifurcation.*

After buckling, the deformed rod behaves like a Hookean spring, whose properties we can find by comparing the compression length to the applied force. The difference in length (from before) is just

$$X(L) - X(0) = \int_0^L ds \cos\theta \simeq \int_0^L ds \left(1 - \frac{1}{2}\theta^2 + \dots\right) \simeq L - \frac{La^2}{4} + \dots$$

So, the displacement due to a force beyond F_c is $La^2/4$. With the knowledge that $a = \sqrt{8f}$,

$$\Delta x \simeq \frac{L}{4} 8f = 2L \left(\frac{F - F_c}{F_c} \right) \qquad \Longrightarrow \qquad F - F_c = \frac{F_c}{2L} \Delta x$$

Thus, beyond the critical force the rod behaves as a spring with effective spring constant $F_c/2L$. Solutions farther from the bifurcation are possible through a numerical approach. For clamped ends (left) and hinged ends (right) we obtain

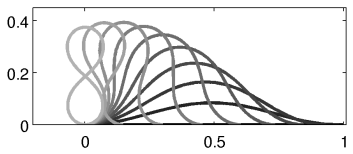

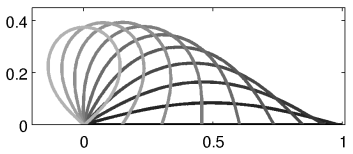

Chemical Kinetics and Pattern Formation

5

The key article on pattern formation that started the field in its modern direction was by Alan Turing (Turing, 1990). He showed that the combination of nonlinear chemical kinetics and diffusion can produce spatio-temporal patterns. These were finally observed experimentally decades after the prediction (**?**). To understand these remarkable results we need first to appreciate the basic laws of mass action for chemical reactions.

5.1 Michaelis-Mentin kinetics

The essential idea behind this simple model of enzyme-substrate dynamics is the reaction scheme

$$E + S \underset{k_{-1}}{\overset{k_1}{\rightleftharpoons}} ES \xrightarrow{k_2} E + P$$

where E is the enzyme, S is the substrate, P is the product, and ES is the enzyme-substrate complex. k_1, k_{-1}, k_2 are the rate constants (empirically measured quantities). For notation, let $s = [S], e = [E], c = [ES], p = [P]$. The concentration is defined as the average concentration (for a CSTR - continuously-stirred tank reactor). The law of mass action is then that the reaction rate is proportional to the concentration or products of concentrations for bilinear reactions. Thus, the differential equations for the time-evolution of the various species are

$$\begin{aligned}
\frac{de}{dt} &= -k_1 es + k_{-1} c + k_2 c \\
\frac{ds}{dt} &= -k_1 es + k_{-1} c \\
\frac{dc}{dt} &= k_1 es - k_2 c - k_{-1} c \\
\frac{dp}{dt} &= k_2 c \ .
\end{aligned}$$

It is worth noting that we have neglected the back-reaction of the product to the complex. One can imagine many different types of initial conditions, but the simplest is that in which the substrate and enzyme concentrations are given, but the complex

and products are zero:

$$s(0) = s_0 \qquad c(0) = 0 \qquad e(0) = e_0 \qquad p(0) = 0 \ .$$

Note that p is completely decoupled from the other reactions, so that

$$p(t) = k_2 \int_0^t c(t')dt' \ .$$

Hence, it is not necessary to consider the dynamics of p any further.

The structure of the reaction scheme is such that no enzyme is destroyed, so the total amount is conserved in time. That is, the quantity $e + c$ must be conserved,

$$\frac{de}{dt} + \frac{dc}{dt} = 0$$

which is indeed satisfied. Given our initial conditions, $e+c = e_0$ at all times. The system of reactions thus reduces from four coupled differential equations to just two

$$\begin{aligned} \frac{ds}{dt} &= -k_1 e_0 s + (k_1 s + k_{-1})c & s(0) &= s_0 \\ \frac{dc}{dt} &= k_1 e_0 s - (k_1 s + k_{-1} + k_2)c & c(0) &= 0 \end{aligned}$$

As in all problems of this type, it is useful to identify appropriate scalings. The concentration of the enzyme/catalyst is generally much smaller than the concentration of the substrate, so that a small parameter is $\epsilon = e_0/s_0$. Let the rescaled time be $\tau = k_1 e_0 t$, and

$$\begin{aligned} u(\tau) &= s(t)/s_0 & \lambda &= \frac{k_2}{k_1 s_0} \\ v(\tau) &= c(t)/e_0 & k &= \frac{k_{-1} + k_2}{k_1 s_0} \end{aligned}$$

Then we have the final equations for the substrate and complex,

$$\begin{aligned} \frac{du}{d\tau} &= -u + (u + k - \lambda)v & u(0) &= 1 \\ \epsilon\frac{dv}{d\tau} &= u - (u + k)v & v(0) &= 0 \end{aligned}$$

Although ϵ is small, neglecting it would remove the highest time derivative in one equation, and is thus a singular perturbation.

Here we refer to the Matlab program Michaelis-Menten.m available on the website, which shows the nature of the solution, namely, a kind of boundary layer at early times when the complex concentration rapidly rises, followed by slow evolution afterwards. It is this slow evolution we study in the next section.

5.1.1 Naive method of solution

Suppose that $\epsilon \ll 1$. Then we can assume the second equation (for the complex) will rapidly reach a quasi-equilibrium in which $dv/d\tau \sim 0$, and so

$$0 = u - (u+k)v \quad \text{or} \quad v = \frac{u}{u+k} \ .$$

In unscaled units this is

$$k_1 es \sim (k_{-1} + k_2)c \qquad e = e_0 - c \qquad c = e_0 \frac{s}{s + K_m}$$

where $K_m = (k_2 + k_{-1})/k_1$. However, this only works if there is a large separation in time scales between the two reactions. The "fast" variable is then coupled to the slow one, which obeys a nonlinear relation. The rate of reaction would then be

$$\frac{dp}{dt} \equiv V = k_2 c = k_2 e_0 \frac{s}{s + K_m} = V_{\max} \frac{s}{s + K_m} \ .$$

The unknown constants K_m and $V_{\max}$ are determined from a plot of $1/V = (1 + K_m/s)/V_{max}$ vs $1/s$. This is the so-called Lineweaver-Burk plot.

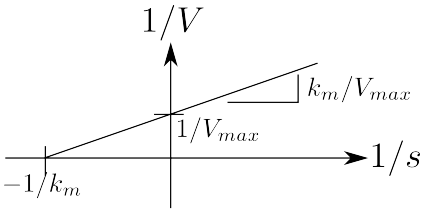

However, this only works if there is a large separation in time scales between the two reactions. The "fast" variable is then "slaved" to the slow variable, which obeys a nonlinear relation. That is the saturating curve giving the production rate (basically, the complex concentration) in terms of the substrate concentration

$$\frac{dp}{dt} = k_2 c \quad \text{with} \quad c = e_0 \frac{s}{s + K_m} \ ,$$

as in the figure below.

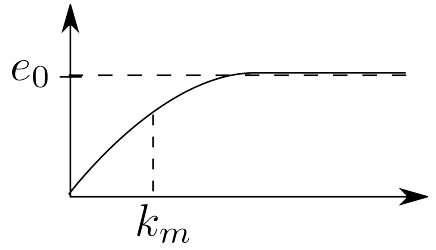

5.1.2 Cooperativity in Reaction Rates

This Michaelis-Menten scheme is an example of a "non-cooperative" reaction. Cooperativity arises from e.g. initial binding effects

altering the probability/kinetics of subsequent binding, as with oxygen and hemoglobin. The binding of oxygen to hemoglobin involves a tetramer of four proteins that each bind oxygen. The binding of each site is linked to the number of bound oxygens, so that the second oxygen is easier to bind than the first, and so on. This allows for cooperativity and very large change in absorbed oxygen over a relatively small shift in oxygen concentration (perfectly tuned for lungs).

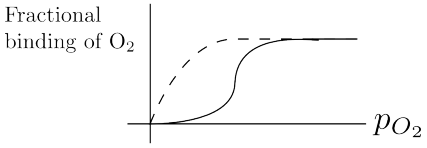

This is essentially as *switch*.

Consider another reaction network

$$E + S \underset{k_{-1}}{\overset{k_1}{\rightleftharpoons}} C_1 \xrightarrow{k_2} E + P$$

$$C_1 + S \underset{k_{-3}}{\overset{k_3}{\rightleftharpoons}} C_2 \xrightarrow{k_4} C_1 + P$$

The reduced equations are

$$\frac{du}{d\tau} = f(u, v_1, v_2) \qquad \epsilon\frac{dv_1}{d\tau} = g_1(u, v_1, v_2) \qquad \epsilon\frac{dv_2}{d\tau} = g_2(u, v_1, v_2)$$

where $v_1 = c_1/e_0, v_2 = c_2/e_0$. Then,

$$\left.\frac{ds}{dt}\right|_{t=0} = e_0 s_0 \frac{(\alpha + \beta s_0)}{\gamma + \delta s_0 + s_0^2}$$

with a general result of a rate

$$rate \sim \frac{s^n}{K_m + s^n}$$

which is known as the *Hill equation*, with n being the *Hill coefficient*. The larger is n, the more sigmoidal and cooperative the reaction.

5.1.3 Slaving

Suppose that there are two degrees of freedom p, q, with a slow reaction and a fast one:

$$\frac{dq}{dt} = \alpha q - \beta pq \qquad \text{slow}$$

$$\epsilon\frac{dp}{dt} = \gamma p - \delta q^2 \qquad \text{fast}$$

where γp is an autocatalytic term. In the steady state

$$\gamma p \sim \delta q^2 \qquad p \sim \frac{\delta}{\gamma} q^2$$

so that

$$\frac{dq}{dt} = \alpha q - \frac{\beta\delta}{\gamma} q^3 = -\frac{\partial V(q)}{\partial q} \qquad V(q) = -\frac{1}{2}\alpha q^2 + \frac{\beta\delta}{4\gamma} q^4 \ ,$$

which looks like a potential. This corresponds to the physical scenario of overdamped dynamic, and in fact produces a bifurcation as a function of α, from a function with a single minimum for $\alpha < 0$ to the double-well potential shown below for $\alpha > 0$.

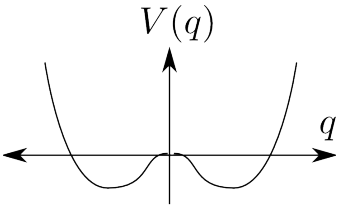

The key point to understand here is that by slaving fast variables to slow ones we can end up with very strong nonlinearities in the effective equations of motion for the slow degrees of freedom, which can exhibit bifurcations, bistability, or even multistability.

5.1.4 Front Propagation

There are many many examples in biological physics in which problems of pattern formation are defined by the boundaries between regions of different behaviour of some generalized *field*, a chemical concentration, population level, etc. A classic example is provided by the spread of the plague in the middle ages, as shown by the advancing contour lines in the figure below.

Fig. 20.2. Approximate chronological spread of the Black Death in Europe from 1347–50. (Redrawn from Langer 1964)

There are many examples in reaction-diffusion systems in which multiple boundaries occur, as shown schematically below

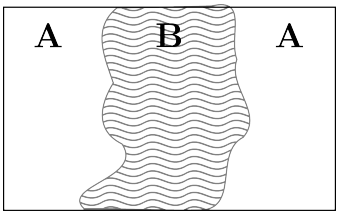

To understand the general problem of *front propagation* we add diffusive effects to the nonlinearities considered so far. The simplest class of one-dimensional models takes the form

$$u_t = mu_{xx} + f(u) \ , \qquad \text{where} \qquad f(u) = -\frac{\partial F}{\partial u}$$

The function $F(u)$ is shown below.

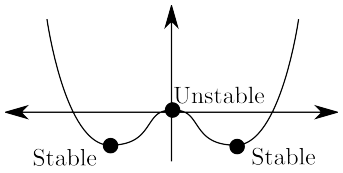

In this case, we can have a kink or front between two locally-stable states, or a stable and an unstable state:

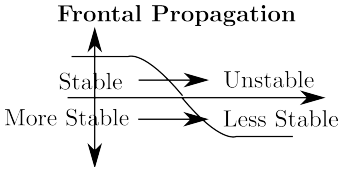

The fundamental question is: *How fast does the front move?* A simple pedagogical model for $f(u)$ involves the cubic nonlinearity

$$f(u) = -F'(u) = -u(u-r)(u-1) \quad \text{for} \ \ 0 < r < 1$$

The function $f(u)$ is shown below

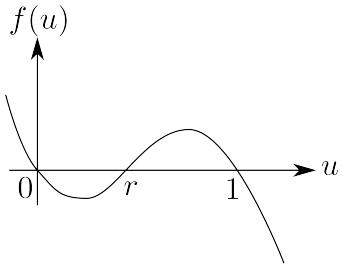

Here, r is a control parameter that will tune the properties of the front, and

$$F(u) = \frac{1}{4}u^2(1-u)^2 + \left(r - \frac{1}{2}\right)\left(\frac{1}{2}u^2 - \frac{1}{3}u^3 - \frac{1}{12}\right)$$

in which an integration constant has been chose to symmetrize the potential so that $F(0) = -(r-1/2)/12$ and $F(1) = (r-1/2)/12$ and the energy difference between the two minima is

$$\Delta F = F(1) - F(0) = \frac{1}{6}\left(r - \frac{1}{2}\right)$$

For $r < 1/2$ the state $u = 1$ is the more stable, and for $r > 1/2$ the state $u = 0$ is more stable.

We first need to establish some terminology and methods that will be useful for many subsequent discussions. The chief technique is a *linear stability analysis* of a steady state (or stationary state). Let us examine in turn the three states that are zeros of the function $f(u)$, since these will satisfy $u_t = 0$.

Near $u = 0$,

$$u_t = mu_{xx} - ru + \dots$$

and let $u = e^{ikx}e^{\sigma t}$. If $\sigma < 0$, u is stable, while if $\sigma > 0$ u is unstable. Substituting for u, we deduce that

$$\sigma = -r - mk^2 \ .$$

Graphically,

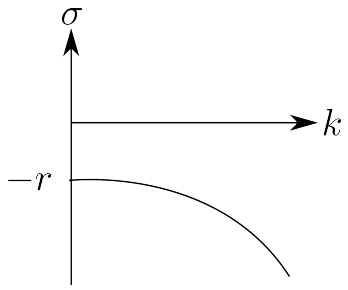

Thus, σ is always negative, regardless of r (thus, stable).

Near $u = 1$, let $u = 1 + \hat{u}$. Then

$$\hat{u}_t \sim m\hat{u}_{xx} - (1 - r)\hat{u}$$
$$\sigma = -(1 - r) - mk^2$$

which is also always stable. Thus, both global minima are stable for all k.

Near $u = r$, we let $u = r + \tilde{u}$ and find

$$\tilde{u}_t = m\tilde{u}_{xx} + r(1 - r)\tilde{u}$$
$$\sigma = r(1 - r) - mk^2$$

and thus there is a band of unstable modes below a critical k. The obvious question is what happens between $u = 0$ and $u = 1$ when $r \sim 1/2$.

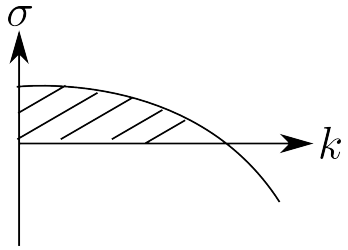

Stationary front (r=1/2)

$$mu_{xx} - u\left(u - \frac{1}{2}\right)(u - 1) = 0$$

Multiplying through by u_x and integrating we find

$$\frac{1}{2}mu_x^2 - F(u) + C = 0$$

where the constant C can be seen to vanish from the boundary conditions ($u \to 1$ as $x \to -\infty$, $u \to 0$ as $x \to \infty$). This yields

$$u = \frac{1}{2}\left[1 - \tanh\left(\frac{x}{2\sqrt{2m}}\right)\right]$$

yielding a transition with a width controlled by m.

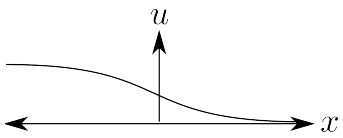

To determine the behavior of the case $r \neq 1/2$, a systematic perturbation theory is necessary. Here, instead, our goal is to derive heuristically the front motion of a 1D PDE with a generic nonlinearity. Consider

$$u_t = mu_{xx} - F'(u)$$

Imagine, after some transient period, a steady uniformly moving solution exists. We then seek a traveling solution of the form

$$u(x,t) = U(x - vt)$$

for some unknown v. The simplest case is for an $F(u)$ like that below.

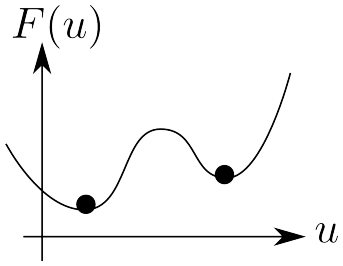

From the traveling-wave ansatz, we have

$$mU_{zz} + vU_z = -(-F'(U))$$

which is similar to Newton's second law ($m\ddot{q} + b\dot{q} =$ force) with m being the "mass" of a fictitious particle, U its "position", and z the "time", and with an effective potential $-F(U)$.

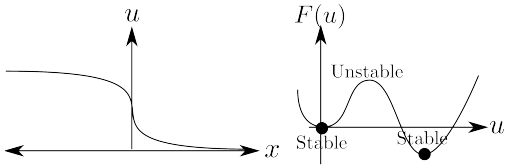

Now, looking at $-F$ instead of F, the situation can be viewed as a ball moving down a hill. The key point is that there exists a *unique* front speed v (a unique damping coefficient in the mechanical analogy), to achieve $u \to 0$ as $t \to \infty$.

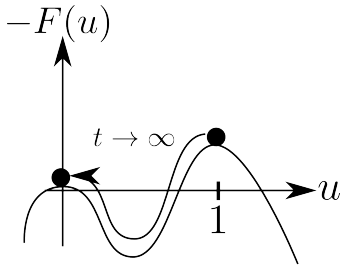

If instead the front consists of a *stable-to-unstable* situation, the analogy will be In this case, any damping coefficient v greater than a critical value v_c will ensure $u \to 0$ as $t \to \infty$.

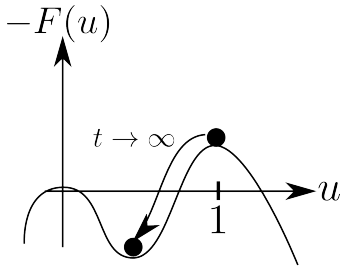

In this case, any damping coefficient v greater than a critical value v_c will ensure $u \to 0$ as $t \to \infty$.

Unfortunately, not every class of problems in pattern formation can be reduced to a system as simple as this one, but from a pedagogical point of view this is very instructive.

We now seek a first integral to the differential equation

$$\begin{aligned} mU_{zz} + vU_z &= -(-F'(U)) \\ mU_zU_{zz} + vU_z^2 &= F'(U)U_z \\ \frac{1}{2}mU_z^2\Big|_{-\infty}^{\infty} + v\int_{\infty}^{\infty} dzU_z^2 &= \int_{-\infty}^{\infty} \frac{dF}{dU}\frac{dU}{dz}dz = F(0) - F(1) \end{aligned}$$

which is precisely the energy difference $-\Delta F$ between the two locally stable minima. We can then formally solve for the front velocity:

$$v = \frac{-\Delta F}{\int_{-\infty}^{\infty} dzU_z^2}$$

The denominator is like a drag coefficient, and is dominated by the front region.

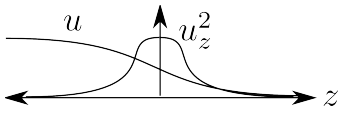

If we approximate the solutions using $U_{stationary}$, which holds when $\Delta F = 0$, we can then approximate the velocity. Note that for the stationary solution $\Delta F = 0, v = 0$

$$mU_{zz} = F'(u)$$

which is just the Euler-Lagrange equation for

$$\int dz \left\{ \frac{1}{2} m U_z^2 + F(u) \right\}$$

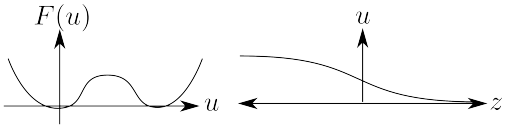

We can understand that the front shape is a compromise between two types of energetic penalties. The first is that for gradients, which would be minimized by making U constant, but this is inconsistent with the far-field boundary conditions. But it would tend to spread out the width of the front to be arbitrarily large. On the other hand, the function $F(u)$ will be minimized by keeping the function U at either of the competing minima of F, thus tending to shrink the transition zone to zero. The balance is what we have found above.

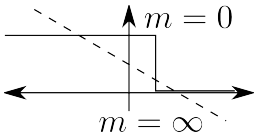

5.2 Phenomenology of Reaction-Diffusion Systems

We consider equations of the form

$$u_t = \mathcal{L}u + \mathcal{N}(u) \ , \qquad \mathcal{L}u = \alpha u + D u_{xx}$$

For solutions of the form $u \propto e^{ikx+\sigma t}$, $\sigma(k) = \alpha - Dk^2$. In k-space, the graph is simple (left) and corresponds to excitations of long wavelength. A more interesting possibility is when both long and short wavelength are damped (see the second plot). In this case, there is a well defined k^* corresponding to the fastest growing mode, leading to a pattern on that scale.

This leads to a fundamental question: *How can diffusion (governed by a second derivative) produce a k-dependence other than k^2?*.

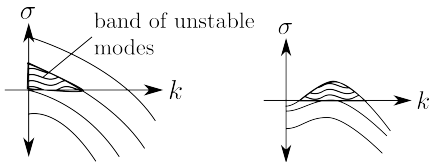

Since $\sigma = \sigma(k^2)$ (by left-right symmetry), we would require

$$\sigma(k) \sim \alpha + \beta k^2 - \gamma k^4 + \dots$$
$$u_t = \alpha u - \beta u_{xx} - \gamma u_{4x} + \dots$$

but such higher-order derivative theories for a single degree of freedom are rare. Instead, two *coupled* reaction-diffusion equations can produce this behavior.

The FitzHugh-Nagumo model. The FHN model was first developed as a simplification neuronal dynamics. Two chemical species are involved: u, the *activator*, and v, the inhibitor. Under suitable rescalings it typically takes the form

$$u_t = D\nabla^2 u + f(u) - \rho v$$
$$\epsilon v_t = \nabla^2 v + \alpha u - \beta v \ .$$

Notice that the inhibitor diffusion constant has been rescaled to unity. We may be interested in a whole range of values for ϵ, not necessarily small. The various terms on the RHS of the equations are:

$f(u)$	Autocatalysis & bistability
ρv	Inhibition
αu	Stimulation
βv	Self-limitation

The presence of the relative diffusion constant D can produce *lateral inhibition* for $D \ll 1$ (different length scales).
Depending on the terms f, D, ϵ, the FHN model can produce homogeneous states, strips, or other periodic patterns, spiral waves, etc.

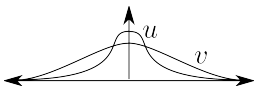

It is sometimes useful to write the FHN model in a more symmetric form

$$u_t = D\nabla^2 u + f(u) - \rho(v - u)$$
$$\epsilon v_t = \nabla^2 v + u - v$$

Does this model have any definite variational structure? Many of the terms conform to a gradient flow:

$$u_t = -\frac{\delta E_u}{\delta u} - \rho v$$
$$\epsilon v_t = -\frac{\delta E_v}{\delta v} + u$$

The remaining terms are actually Hamiltonian!

$$u_t = -\rho v \qquad \epsilon v_t = u$$

Consider the simplest regime (like in Michaelis-Mentin kinetics), the *fast inhibitor limit*. Here we set $\epsilon = 0$ and obtain a local in time but nonlocal in space relationship between v and u:

$$(\nabla^2 - 1)v = -u$$

Given a Green's function for the operator $(\nabla^2 - 1)$, we can solve this:

$$v(\mathbf{x}) = \int d\mathbf{x}' G(\mathbf{x} - \mathbf{x}')u(\mathbf{x}')$$

For example, in one dimension,

$$G(x - x') = \frac{1}{2}\mathrm{e}^{-|x-x'|}$$

and in two dimensions,

$$G(\mathbf{x} - \mathbf{x}') = \frac{1}{2\pi}K_0(|\mathbf{x} - \mathbf{x}')$$

So, in the fast inhibitor limit we have

$$u_t = D\nabla^2 + f(u) + \rho u - \rho \int d\mathbf{x}' G(\mathbf{x} - \mathbf{x}')u(\mathbf{x}')$$

which is a closed, nonlocal equation of motion. In fact, u is variational,

$$u_t = -\frac{\delta E}{\delta u}, \quad E = \int d\mathbf{x} \left\{ \frac{1}{2}D|\boldsymbol{\nabla} u|^2 + F(u) - \frac{1}{2}\rho u^2 \right\} + \frac{1}{2}\rho \int d\mathbf{x} \int d\mathbf{x}' u(\mathbf{x})G(\mathbf{x} -$$

The nonlocal term reminds us of electrostatics. In a later paper (Lee et al., 1993), a non-locality was observed where interfaces don't cross and the action of inhibitor fronts are also sharp.

5.3 The Turing Instability

Consider a 2-species model, with concentrations $u(\mathbf{x}, t)$ and $v(\mathbf{x}, t)$ in a bounded domain $\mathcal{D}$. We assume Neumann boundary conditions of no flux in or out, so $\hat{\mathbf{n}} \cdot \boldsymbol{\nabla} u\Big|_{\partial\mathcal{D}} = \hat{\mathbf{n}} \cdot \boldsymbol{\nabla} v\Big|_{\partial\mathcal{D}} = 0$

The pair of reaction-diffusion equations is

$$\begin{aligned} u_t &= D_u \nabla^2 u + f(u, v) \\ v_t &= D_v \nabla^2 v + g(u, v) \ , \end{aligned}$$

where f and g are some smooth functions of their arguments, representing, for example, autocatalysis, feedback inhibition, etc. We suppose that f and g are such that there exists a *stable*, uniform steady state (so $f(u_0, v_0) = g(u_0, v_0) = 0$), i.e. the Jacobian

$$J = \begin{pmatrix} f_u & f_v \\ g_u & g_v \end{pmatrix}$$

has

$$\mathrm{Tr} = f_u + g_v < 0 \quad \text{and} \quad \mathrm{Det} = f_u g_v - f_v g_u > 0$$

at (u_0, v_0).

These requirements arise from linearizing the equations of motion via $u = u_0 + \delta u$, $v = v_0 + \delta v$, to obtain the dynamics

$$\partial_t \begin{pmatrix} \delta_u \\ \delta_v \end{pmatrix} = \begin{pmatrix} f_u & f_v \\ g_u & g_v \end{pmatrix} \begin{pmatrix} \delta_u \\ \delta_v \end{pmatrix}$$

As this is a linear equation it has solutions of the form $\mathrm{e}^{\sigma t}$, and σ will be determined by the determinental condition

$$\begin{vmatrix} f_u - \sigma & f_v \\ g_u & g_v - \sigma \end{vmatrix}$$

This is just $\sigma^2 - \mathrm{Tr}\sigma + \mathrm{Det}$, with solutions $\sigma_\pm = (1/2)\left\{\mathrm{Tr} \pm \sqrt{\mathrm{Tr}^2 - 4\mathrm{Det}}\right\}$. For stability, we require the real part of both roots of σ to be negative. So, if $\mathrm{Tr} < 0$ the root in which we choose the negative sign in front of the square root is clearly negative. There are two cases that will allow the second root to be negative. If $0 < \mathrm{Det} < \mathrm{Tr}^2/$ the square root is real but less then $|\mathrm{Tr}|$ and the root is negative, while for larger values of Det the square root yields an imaginary contribution, and still the real part of σ is negative.

Now we examine what happens when we perturb this *homogeneous* steady state with spatial-temporal variations, $u = u_0 + p(\mathbf{x}, t)$, $v = v_0 + q(\mathbf{x}, t)$, to obtain the dynamics

$$\begin{aligned} p_t &= f_u p + f_v q + D_u \nabla^2 p \\ q_t &= g_u p + g_v q + D_v \nabla^2 q \ , \end{aligned}$$

It is always possible to expand a function of $\mathbf{x}$ in the domain $\mathcal{D}$ as an infinite series of eigenfunctions of the (Helmholtz) equation

$$\begin{aligned} \nabla^2 w_k + \lambda_k^2 w_k &= 0 \quad (\text{in } \mathcal{D}) \\ \hat{\mathbf{n}} \cdot \boldsymbol{\nabla} w_k &= 0 \quad (\text{on } \partial\mathcal{D}) \end{aligned}$$

For example, in $d = 1$ with $\mathcal{D} = [0, L]$, we have $w_k = \cos(k\pi x/L)$ and $\lambda_k = k\pi/L$. More generally, if we write

$$\begin{aligned} p &= \sum_k \hat{p}_k \mathrm{e}^{\sigma_k t} w_k(\mathbf{x}) \\ q &= \sum_k \hat{q}_k \mathrm{e}^{\sigma_k t} w_k(\mathbf{x}) \end{aligned}$$

and substitute (and drop the suffix "k") for convenience, Then the new equation governing the growth rate will be similar to the homogeneous case, but with the diffusive contributions on the diagonal.

$$\begin{vmatrix} (f_u - D_u\lambda^2 - \sigma) & f_v \\ g_u & (g_v - D_v\lambda^2 - \sigma) \end{vmatrix} .$$

This will have a nontrivial solution if and only if

$$\sigma^2 + \left[(D_u + D_v)\lambda^2 - f_u - g_v\right]\sigma + (D_u\lambda^2 - f_u)(D_v\lambda^2 - g_v) - f_v g_u = 0$$

Now we note that the sum of the roots satisfies

$$\sigma_1 + \sigma_2 = -(D_u + D_v)\lambda^2 + f_u + g_v < 0 \ ,$$

where this negativity arises from the fact that the assumption of a stable *homogeneous* state already required $f_u + g_v < 0$, and the new diffusive contributions are clearly negative. The product of the two roots satisfies

$$\sigma_1\sigma_2 = D_u D_v\lambda^4 - (D_v f_u + D_u g_v)\lambda^2 + \mathrm{Det} \ ,$$

where Det is that of the homogeneous system.

To repeat:

$$\sigma_1\sigma_2 = D_u D_v\lambda^4 - (D_v f_u + D_u g_v)\lambda^2 + \mathrm{Det} \ ,$$

Now, since the sum is < 0, one root can have a positive real part only if the product is < 0 (actually, then both roots are real). Thus, a *necessary* condition for instability is the possibility of a negative product, and since the λ^4 term is clearly positive and Det is positive, we require the overall coefficient of λ^2 be negative, or

$$D_v f_u + D_u g_v > 0 \ .$$

Without loss of generality, we can take $D_v > D_u > 0$. But if $f_u + g_v < 0$, we need f_u and g_v to have opposite signs, with $f_u > 0$ and $g_v < 0$. The condition above is not a sufficient condition for instability, since it must be possible to find a permitted λ that makes $\sigma_1\sigma_2 < 0$. That is, the equation (with $x = \lambda^2$)

$$h(x) = D_u D_v x^2 - (D_v f_u + D_u g_v)x + \mathrm{Det} = 0$$

must have positive roots. This requires

$$(D_v f_u + D_u g_v)^2 > 4\mathrm{Det}\cdot D_u D_v \ .$$

Our sufficient condition is so provided one of the permitted λs lies between λ_- and λ_+,

$$\lambda_\pm^2 = \frac{1}{2D_u D_v}\left\{Dv f_u + D_u g_v \pm \sqrt{(D_v f_u + D_u g_v)^2 - 4D_u D_v \mathrm{Det}}\right\}$$

So our sufficient condition is

$$D_v f_u + D_u g_v > 2\sqrt{\mathrm{Det}}\sqrt{D_u D_v}$$

Now define $d = D_v/D_u > 1$. Then

$$d f_u - 2\sqrt{\mathrm{Det}}\sqrt{d} + g_v > 0 \ .$$

This will clearly be true if d is sufficiently large. Looking at the crossing point (LHS=0) we find

$$\sqrt{d} = \frac{\sqrt{\text{Det}} + \sqrt{\text{Det} - f_u g_v}}{f_u}$$

So finally we can write the inequality (recall $f_u g_v < 0$)

$$\sqrt{d} \geq \frac{1}{f_u}\left(\sqrt{\text{Det}} + \sqrt{\text{Det} - f_u g_v}\right) > 0 \ .$$

Finally, we can examine the typical length scale of the instability. At onset, $\lambda = \lambda_c$, where $h(\lambda_c^2) = 0$ is a double root. Then

$$D_v f_u + D_u g_v = 2\sqrt{\text{Det}}\sqrt{D_u D_v} \quad \text{and} \quad \lambda_c^2 = \frac{\sqrt{\text{Det}}}{\sqrt{D_u D_v}}$$

And then the unstable wavelength is

$$\ell_c = \frac{2\pi}{\lambda_c}$$

Let's look at an example (Murray, 1st edition, §14.2). Autocatalytic chemical reactions

$$\begin{aligned} u_t &= D_u \nabla^2 u + k_1 - k_2 u + k_3 u^2 v \\ v_t &= D_v \nabla^2 v + k_4 - k_3 u^2 v \ . \end{aligned}$$

This can be simplified by suitable rescalings. We can always find P, Q, R, S such that

$$\frac{\partial}{\partial t} \to P\frac{\partial}{\partial t} \ , \quad u \to Qu \ , \quad v \to Rv \ , \quad \boldsymbol{\nabla} \to S\boldsymbol{\nabla} \ .$$

The result is the system

$$\begin{aligned} u_t &= \nabla^2 u + a - u + u^2 v \\ v_t &= d\nabla^2 v + b - u^2 v \ . \end{aligned}$$

where as usual $d = D_v/D_u > 1$. With $f(u,v) = a - u + u^2 v$ and $g(u,v) = b - u^2 v$ the homogeneous fixed point is

$$u_0 = a + b \ , \quad v_0 = \frac{b}{(a+b)^2} \ .$$

The Jacobian of the linear stability problem is then

$$\begin{pmatrix} (-1 + 2u_0 v_0) & u_0^2 \\ -2u_0 v_0 & -u_0^2 \end{pmatrix} \ .$$

Thus, $\text{Tr} = -1 - u_0^2 + 2u_0 v_0$ and $\text{Det} = u_0^2 > 0$. Substituting, we find

$$\text{Tr} = \frac{b - a - (a+b)^3}{a+b} \ .$$

Thus, the spatially uniform system is linearly stable is $b - a < (a + b)^3$. The *necessary* conditions are

$$f_u > 0 \rightarrow -1 + 2u_0v_0 > 0 \rightarrow b > a$$
$$df_u + g_v > 0 \rightarrow d(b - a) > (b + a)^3 \ .$$

The sufficient condition is

$$df_u + g_v > 2\sqrt{\mathrm{Det}}\sqrt{d} \quad \text{or} \quad \sqrt{d} > \frac{(b+a)^2}{(b-a)}\left(1 + \sqrt{\frac{2b}{b+a}}\right)$$

Exercise: construct a stability diagram in a-b space.

In the 1990s there were two independent discoveries of true Turing instabilities in chemical systems. Here is the abstract from the Austin group's famous paper and examples of the patterns they found:

Transition from a uniform state to hexagonal and striped Turing patterns

Q. Ouyang & Harry L. Swinney

Center for Nonlinear Dynamics and Department of Physics, The University of Texas, Austin, Texas 78712, USA

CHEMICAL travelling waves have been studied experimentally for more than two decades[1–5], but the stationary patterns predicted by Turing[6] in 1952 were observed only recently[7–9], as patterns localized along a band in a gel reactor containing a concentration gradient in reagents. The observations are consistent with a mathematical model for their geometry of reactor[10] (see also ref. 11). Here we report the observation of extended (quasi-two-dimensional) Turing patterns and of a Turing bifurcation—a transition, as a control parameter is varied, from a spatially uniform state to a patterned state. These patterns form spontaneously in a thin disc-shaped gel in contact with a reservoir of reagents of the chlorite–iodide–malonic acid reaction[12]. Figure 1 shows examples of the hexagonal, striped and mixed patterns that can occur. Turing patterns have similarities to hydrodynamic patterns (see, for example, ref. 13), but are of particular interest because they possess an intrinsic wavelength and have a possible relationship to biological patterns[14–17].

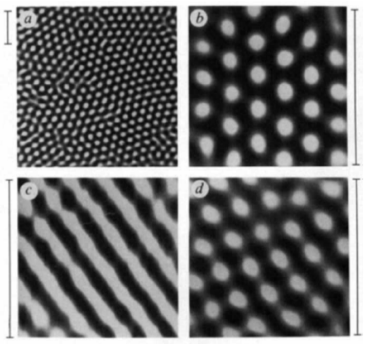

5.4 Phenomenology of *Dictyostelium discoideum*

One of the most well-studied pattern-forming systems in biology is the slime mould *Dictyostelium discoideum*, which can exhibit both unicellular and multicellular lifestyles (see diagram below, from Wikipedia). In the former the cells feed on bacteria in the enviroment and have little if any communication with each other. When a population is starved for some hours, it transitions to a multicellular form by emitting propagating waves of cyclic AMP (cAMP) which engender chemotaxis toward the wave centers and the formation of a dense multicellular body.

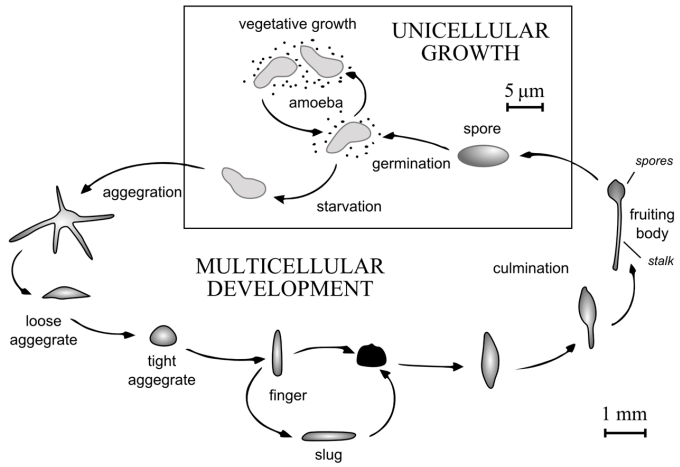

That object can move around on the substrate and eventually settles, forming a base with a stalk supporting spores. The latter can be carried by wind, water, or larger organisms to more fertile environs, where the life cycle begins again.

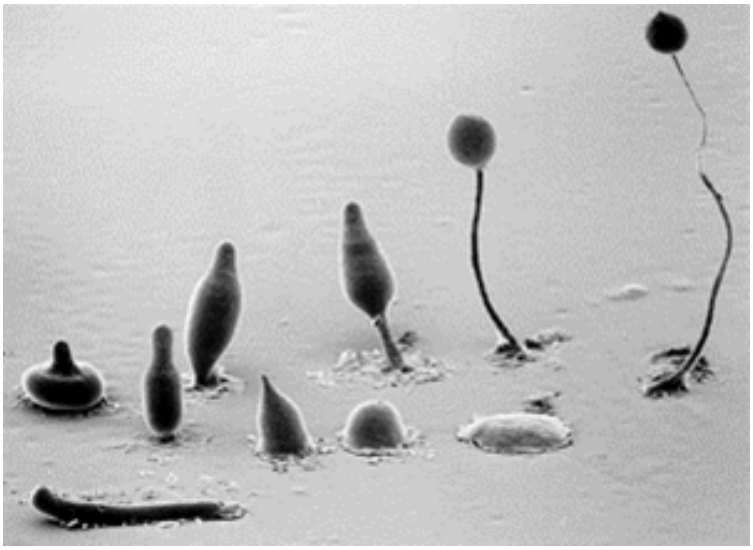

Of the many fascinating aspects of this organism's life cycle, the formation of cAMP waves has been among the most widely studied. Experiments show that they can take the form either of rotating spirals or target patterns, raising general issues of *pattern selection.*

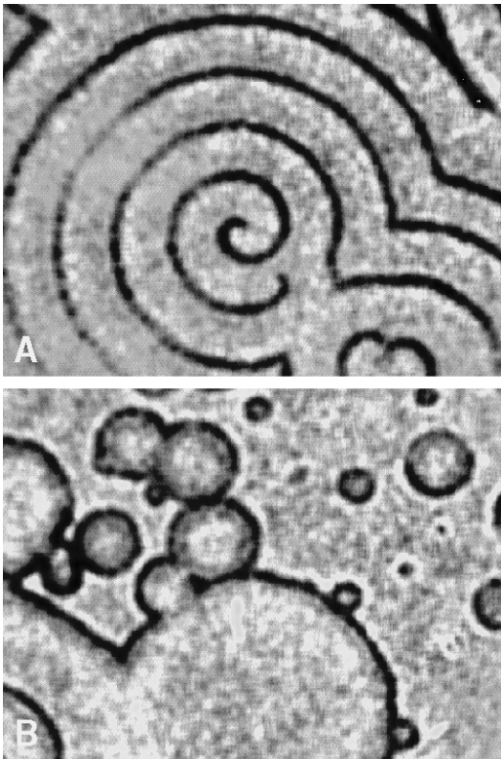

With this as motivation, we study next the simplest model in which cellular motion results from chemical gradients.

5.5 The Keller-Segel Model of Chemotaxis

This is a model with two variables: n, the cell concentration, and c the chemoattractant concentration. In the absence of cell division, n must obey a conservation law of the form

$$n_t = -\boldsymbol{\nabla} \cdot \mathbf{J} \ ,$$

where the cell current has diffusive and chemotactic contributions,

$$\mathbf{J} = -D_n \boldsymbol{\nabla} n + rn \boldsymbol{\nabla} c \ .$$

Here, the response coefficient r might be a function of the chemoattractant concentration c, as in oxygentaxis. For run-and-tumble locomotion, we expect $D_n \sim \ell^2/\tau$, with $\ell \sim u\tau$, where u is the swimming speed. Accounting for release and degredation of c the KS eqns are

$$\begin{aligned} n_t &= D_n \nabla^2 n - \boldsymbol{\nabla} \left(rn \boldsymbol{\nabla} c \right) \\ c_t &= D_c \nabla^2 c + fn - kc \ . \end{aligned}$$

Clearly there is a steady state with $n = n_0$ and $fn_0 = kc_0$, so $c_0 = fn_0/k$.

We perform a linear stability analysis in one spatial dimension by setting

$$n = n_0 + \eta \ , \qquad c = c_0 + \chi \ .$$

which yields

$$\begin{aligned} \eta_t &= D_n \eta_{xx} - r n_0 \chi_{xx} \\ \chi_t &= D_c \chi_{xx} + f\eta - k\chi \ . \end{aligned}$$

The linear stability problem for perturbations of the form $\mathrm{e}^{iqx+\sigma t}$ is just

$$\begin{vmatrix} -D_n q^2 - \sigma & r n_0 q^2 \\ f & -D_c q^2 - k - \sigma \end{vmatrix} = 0 \ .$$

If we write this as $\sigma^2 + b\sigma + c = 0$, with $b = k + (D_n + D_c)q^2$ and $c = D_n q^2 (D_c q^2 + k) - f r n_0 q^2$, then $\sigma_\pm = (-b \pm \sqrt{b^2 - 4c})/2$, and we require $b^2 - 4c > 0$ for real roots. The stability condition is $c > 0$, or

$$D_n \left(D_c q^2 + k \right) > f r n_0 \ .$$

Thus, as $q \to 0$ an instability is possible if

$$\frac{f r n_0}{D_n k} > 1 \ .$$

5.6 Advection and Diffusion

Let us return to the competition between advection and diffusion discussed at the beginning of the course to understand the important concept of *boundary layers*. If a concentration field is subject to transport by a fluid flow field $\mathbf{u}$ in addition to diffusion, then

$$\frac{\partial c}{\partial t} + \mathbf{u} \cdot \boldsymbol{\nabla} c = D \nabla^2 c \ .$$

By the usual scaling arguments we suppose there exists a characteristic speed U and length scale L, implying a time scale L/U. Then if we introduce

$$t' = t/(L/U) \ , \qquad \mathbf{x}' = \mathbf{x}/L \ , \qquad \mathbf{u}' = \mathbf{u}/U \ ,$$

the advection-diffusion equation becomes

$$\frac{U}{L} \frac{\partial c}{\partial t'} + U \mathbf{u} \cdot \frac{1}{L} \boldsymbol{\nabla}' c = D \frac{1}{L^2} \nabla'^2 c \ ,$$

or

$$Pe \left(\frac{\partial c}{\partial t'} + \mathbf{u} \cdot \boldsymbol{\nabla}' c \right) = \nabla'^2 c \ ,$$

Consider now a two-dimensional example in which a uniform fluid velocity field moves from left to right, $\mathbf{u} = (U, 0)$, so

$$\frac{\partial c}{\partial t} + U\frac{\partial c}{\partial x} = D\nabla^2 c \ .$$

This might be flow sweeping past a small pointlike source in the plane or, as we consider here, parallel to a surface at $y = 0$ held at c_0. In the steady state, the only length scale in the problem is D/U, so if we scale space by that we have

$$\frac{\partial c}{\partial x} = \nabla^2 c \ ,$$

with $c = c_0$ at $y = 0$ and $c \to 0$ as $y \to \infty$.

The key point is that if a region in which $c \neq 0$ remains *thin* then

$$\left|\frac{\partial^2 c}{\partial y^2}\right| \gg \left|\frac{\partial^2 c}{\partial x^2}\right|$$

Then,

$$\frac{\partial c}{\partial x} \simeq \frac{\partial^2 c}{\partial y^2}$$

The problem

$$\frac{\partial c}{\partial x} \simeq \frac{\partial^2 c}{\partial y^2}$$

is just a disguised version of the previously-solved time-dependent diffusion equation ($t \to x, x \to y$), so we read off the answer as:

$$c = c_0 \mathrm{erfc}\left[\frac{y}{\sqrt{4x}}\right] = c_0 \mathrm{erfc}\left[\frac{y}{\sqrt{4Dx/U}}\right] = c_0 f(\eta)$$

which we recognize as a similarity solution with a length scale $\delta \sim (Dx/U)^{1/2}$.

Is the original assumption justified?

$$c_x \sim c_0 \frac{\eta f'(\eta)}{x} \ , \qquad c_y \sim c_0 \left(\frac{U}{4Dx}\right)^{1/2} f'(\eta) \ ,$$

so $|c_y| \gg |c_x|$ if

$$\left(\frac{U}{Dx}\right)^{1/2} \gg \frac{1}{x} \ , \qquad \text{or} \qquad x \gg D/U \ .$$

Electrokinetic Phenomena

6

6.1 Some Literature

This chapter is based on the result from the following papers and books. For the general polymer dynamics we used the Rubinstein book, while the Delgado review contains a very good, albeit technical, introduction into electrokinetic effects. Finally we discuss the applicability of the general effects with examples taken from the recent literature discussing single colloid electrophoretic measurements (Semenov et al., 2009)(Otto et al., 2008). The chapter finished with an extensive discussion of the coupling of hydrodynamic and electrokinetic effects for voltage-driven transport through nanopores (Keyser et al., 2010).

- general polymer physics and dynamics: Rubinstein "Polymer Physics", chapters 7-9
- for reptation and relaxation times: Strobl "The Physics of Polymers", Chapter 3,8
- Electrophoresis modern perspective, Viovy, Electrophoresis of DNA and other polyelectrolytes: Physical mechanisms, Rev. Mod. Phys. (2000) (Viovy, 2000)
- concise treatise of all major phenomena: Hunter et al., "Measurement and interpretation of electrokinetic phenomena", J. Coll. Interface Sci. (2007) (Delgado et al., 2007)
- Zimm and Levene, "Problems and prospects in the theory of gel electrophoresis of DNA" Qart. Rev. Biophys (1992)
- technical development paper: Otto, et al. "Optical tweezers with 2.5 kHz bandwidth video detection for single-colloid electrophoresis" Rev. Sci. Instr. (2008) (Otto et al., 2008)
- forces in nanopores 1: Keyser, van Dorp, Lemay, "Tether forces in DNA electrophoresis", Chem. Soc. Rev. (2010) (Keyser et al., 2010)

6.2 Background

We briefly discussed the Poisson-Boltzmann (PB) equation earlier in the course. Here we will no turn to the implications of the PB equation for the motion of charged particles and macromolecules in aqueous solutions subject to an electric fields. As Delgado et al. state in their very nice review article (Delgado et al., 2007):

'Electrokinetic phenomena (EKP) can be loosely defined as all those phenomena involving tangential fluid motion adjacent to a charged surface. They are manifestations of the electrical properties of interfaces under steady-state and isothermal conditions. In practice, they are often the only source of information available on those properties. For this reason, their study constitutes one of the classical branches of colloid science, electrokinetics, which has been developed in close connection with the theories of the electrical double layer and of electrostatic surface forces.'

Electrokinetic phenomena which will be discussed here include electro-osmosis, electrophoresis and streaming currents. While the first two are created by an electric field the latter is due to a mechanical force acting ion charges at the liquid-solid interface. As will become apparent in the following discussion, electro-osmosis and -phoresis are intimately related and a distinction is only possible in the most simple situations. In most realistic situations like during the electrophoretic motion of a DNA molecule in a gel during gel-electrophoresis this will be discussed in detail.

6.3 Definitions

Electrophoresis is the movement of charged particles or macromolecules (these are often called polyelectrolytes in this context), under the influence of an external electric field. The main observables are the electrophoretic velocity, v_e (units ms^{-1}) and electrophoretic mobility, u_e ($\mathrm{m}^2\mathrm{V}^{-1}\mathrm{s}^{-1}$). The latter is defined as $u_e = |v_e|/E$,wheer E is the electric field strength. The mobility is counted positive if the particles move toward lower potential (negative electrode) and negative in the opposite case.

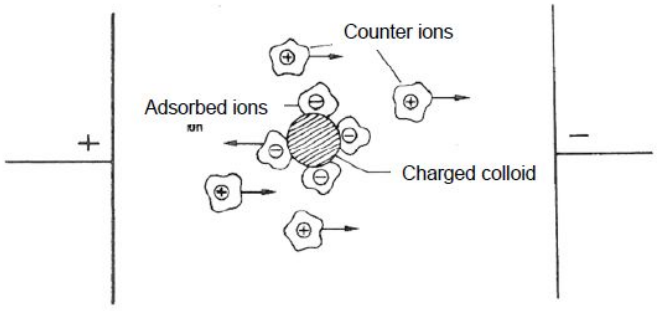

Electro-osmosis is the motion of a liquid over an *immobilized* charged surface with an electric field applied parallel to it. The motion is the result of the force exerted by the electric field on the movable counter-ions. The counter-ions transfer momentum to the liquid thus giving rise to the electro-osmotic flow. The electro-osmotic flow velocity, v_{eof} (units ms^{-1}), is the uniform velocity of the liquid **far** from the charged interface. Far is in relation to the screening length in the liquid. Other important

quantities here are the volume flow rate $Q_{eof,E}$ ($m^4V^{-1}s^{-1}$) divided by electric field strength. Obviously this fluid flow will give rise to an electro-osmotic counter-pressure, Δp_{eof}, which gives the the pressure difference that must be applied across the system to stop any volume flow.

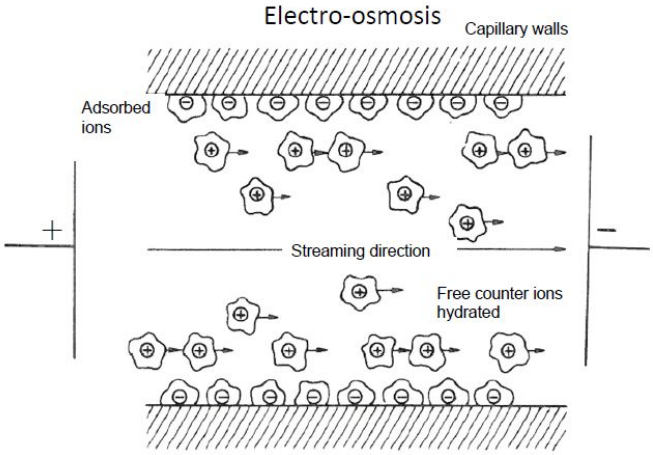

Streaming potential U_{str} and current I_{str} are intimately related to each other. U_{str}, is the potential difference at zero electric current, caused by the flow of liquid over a charged surface. These are usually encountered in fluid flows through charged capillary tubes, micro- or nanofluidic channels. The potential difference is usually measured across the channel. Streaming potentials are due to charge accumulation since the movable counter-ions are displaced by the applied flow. The corresponding streaming current, I_{str} (A), is simply the current when the two sides of the capillary of channel are short-circuited.

In the literature there a number of other phenomena which are closely related but are beyond the scope of this chapter. Delgado et al. give a very good and complete overview of electro-kinetic phenomena (Delgado et al., 2007).

6.4 Fundamental problem and the Zeta-potential

The reason for the still active interest in electrokinetic phenomena stems from the fact that a proper understanding is involved due to the intimate coupling to hydrodynamic phenomena. Thus, very often for a complete understanding it is not enough to just consider the PB equation and its solution for the respective geometry but the (Navier-)Stokes equation has to be solved at the same time. This brings about a very rich behavior with some counter-intuitive results (Keyser et al., 2010). In addition there is the problem of the finite size of ions. As we calculated earlier the screening length can be easily approach dimensions of 0.3 nm in salt concentrations

of e.g. 1M KCl. Even at physiological conditions with an ionic strength of about 150 mM we have to work with a screening length of roughly 1 nm. Compared to the diameter of a water molecule of about 0.2 nm this shows that a description ignoring the finite size of water and counter-ions will probably fail at these short length-scales. Amazingly this is often not the case.

One common approach to keep the interpretation of real systems simple a new parameter is introduced which has achieved wide-spread acceptance. This is the zeta-potential which combines a number of assumptions and (quite amazingly) works quite well for specific experimental conditions. The definition is best explained by considering a more detailed image of the electric double layer on charged surfaces in liquids as shown below (adapted from (Hamann and Vielstich, 2005)).

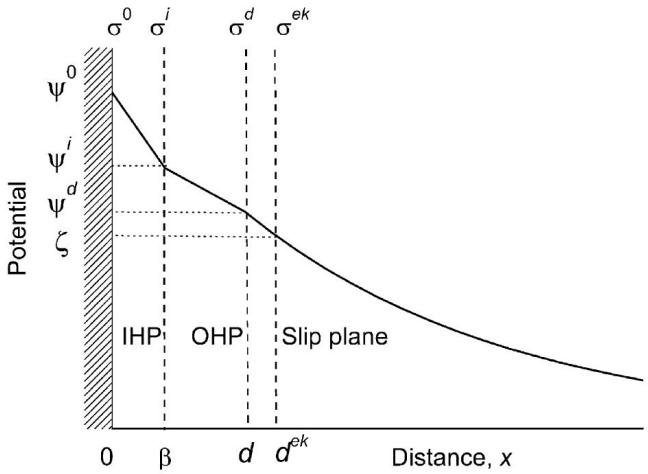

The most important point to remember is, that the zeta-potential denotes the potential at the no-slip plane at distance d^{ek} from the surface with surface charge σ^0 and surface potential Φ^0. The zeta(ζ-potential is always smaller than the bare surface potential and includes a number of simplifications:

- there is a thin layer that does not contain any charges due to an absorbed water layer etc. Thus at the inner Helmholtz plane (IHP) we have potential $\Phi^i < \Phi^0$
- the surface will have a certain potential Φ^0 but this will be reduced by adsorbed (fixed) ions in the outer Helmholtz plane (OHP) with $\Phi^d < \Phi^i$
- these ions are fixed and have another charge free layer thus $zeta < \Phi^d$ which can be significantly smaller than Φ^0 this defines also the no-slip plane
- shear is generated only at the slip plane since only there water and ions can start moving

The IHP and OHP are often referred to as Stern layer. The

Stern layer does not distinguish between the IHP and OHP encompassing everything close to the surface below the no-slip plane.

It is important to emphasize here that the exact position of the slip plane is not known (and under debate). The ζ depends on the type and valency of the counter-ions, the salt concentrations and the geometry of the system complicating the situation. Thus ζ is a very successful fudge-parameter which should always be taken with a grain of salt when you find the claim that somebody measured THE ζ-potential and thus THE surface charge of a polyelectrolyte like DNA.

6.5 Double-layer capacitance

Despite its complications of the electric double layer it is nonetheless a very important concept since most hydrophilic surfaces carry some kind of charge. Of course polar molecules and surfaces are hydrophilic as well without being charged.

The double layer in fact is nothing else than a capacitor and thus the barrier for the transport of charges in salt solutions/electrochemical cells (batteries) as it also exists on any biased metal surface. Measuring the the differential capacitance yields information about rearrangements in the inner and outer Helmholtz planes. Since this technique is useful we just summarize it here.

To access the thickness of IHP and OHP on ecan simply measure the differential capacitance

$$C_{diff} = \frac{dQ}{dV}$$

with Q as the charge on the capacitor and V the applied voltage. With $I_C = dQ/dt$ we get

$$I_C = \frac{dQ}{dt}\frac{dV}{dt} = C_{diff}\frac{dV}{dt}.$$

A typical measurements looks like this (adapted from (Hamann and Vielstich, 2005):

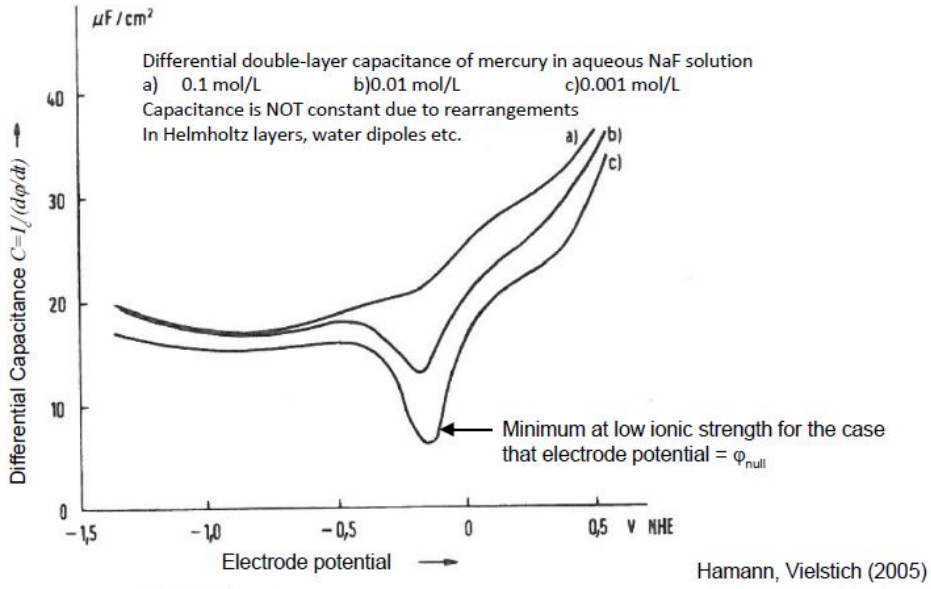

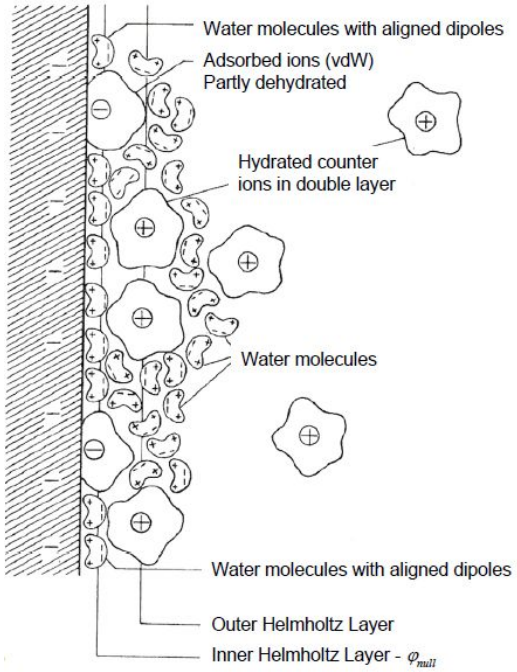

where ϕ_{null} denotes the Galvani potential between liquid and electrode material. The substructure is due to reorientations in the layers.

To get an impression about the order of magnitude we can estimate the capacitance. In strong aqueous electrolytes and assuming that the double layer is a parallel plate capacitor, we can estimate the capacitance per unit area to be $C/A = \epsilon_0\epsilon_r/d$. Here d is around 0.2 nm which is the thickness of the IHP. This yields $C/A \approx 350\ \mu\text{Fcm}^{-2}$. This is a factor of 7 too large compared with the measured values of 5-50 μFcm^{-2}. This discrepancy is due to the reduced ϵ_r of about 6 compared to free water. The water dipoles are fixed and thus ϵ_r is reduced.

In a realistic description, there are two capacitors in series at the IHP and OHP and ϵ_r is a function of distance from the surface. So the capactiance of the Stern layer C_{Stern} is

$$\frac{1}{C_{Stern}} = \frac{1}{C_{dipole}} + \frac{1}{C_{IHP-OHP}} \approx \frac{a_{H2O}}{\epsilon_{dipole}} + \frac{a/2}{\epsilon_{IHP}}$$

where a_{H2O} is the diameter of water and $a/2$ is the radius of the hydrated counter ions. This is valid for short screening length below 1 nm and has to be extended for small salt concentrations taking into account the diffuse layer capacitance beyond the Stern layer.

The details go beyond this course and can be found in any electrochemistry textbook. However, It is important to remember this. It is interesting to note that upon application of a few 100 mV and given the thickness of less than a nm the field strength in the Stern layer can easily reach 10^8 V/m. This is enough to alter the stability of weak molecular bonds near the electrode surface and lead to the dissociation of weak acids.

It is also possible to build ionic transistors and diodes by applying the double layer and either a fixed surface charge or with electrode materials. These systems are under active development at the moment as they could be used for desalting solutions or control of molecular flow.

6.6 Electrophoresis

6.6.1 Helmholtz-Smoluchowski equation

In order to model electrophoretic motion of charged particles with charge ze) in solution we can start by calculating the force an electric field E.

$$F_e = zeE = ze\frac{dV}{dx}$$

where $V(x)$ is the potential distribution (Delgado et al., 2007). However since we are in liquid we have to take the friction coefficient β into account and thus in steady state we have $F_e + v_e\beta = 0$. Using that diffusion current $J_e = cv_e$ we get with the concentration of particles c

$$J_e = -\frac{zec}{\beta}\frac{dV}{dx}$$

. Remember that $1/\beta$ is the mobility of the ions.

Transferring this to macroscopic particles with micrometer dimensions and a double layer as depicted above is straightforward. It can be noted that $\epsilon_r\epsilon_0\zeta\beta/\eta$ has the units of a charge. With this major simplification we can can write

$$J_e = -\frac{\epsilon_r\epsilon_0\beta\zeta c}{\beta\eta}\frac{dV}{dx}$$

It directly follows for the electrophoretic velocity v_e

$$v_e = \frac{\epsilon_r \epsilon_0 \zeta}{eta} \frac{\partial V}{\partial x}$$

and the Helmholtz-Smoluchowski equation for the mobility u_e

$$v_e = \frac{\epsilon_r \epsilon_0 \zeta}{eta}.$$

This is valid when we can ignore any details about the particle namely that the the diameter is much larger than the screening length.

6.6.2 Limitations

As the concept of ζ-potential this is also a simplified approach which neglects several important phenomena:
(i) it does not include the treatment of strongly curved surfaces (i.e., surfaces for which the condition for the screening length does not apply);
(ii) surface conduction in the diffuse and the OHP is not taken into account
(iii) polarization of the electric double layer.

Checking the validity of (i) is straightforward, (ii) will be explained later and is only relevant when $\zeta > 50$ mV. Polarization would account for the accumulation of charge in front and back of the moving particle which would result in a dipole moment and thus an additional field.

6.6.3 Single particle AC electrophoresis

A system which quite nicely allows to test the ζ-potential concept is a single colloid trapped in the focus of an optical trap (Otto et al., 2008)(Semenov et al., 2009). Assuming that the electrical field is constant and just a function of time we can easily measure electrophoretic mobility $u_e = v_e/E$. Since we work with optical trap we also have the optical tweezers restoring force $F = -\kappa \Delta x$ thus we get for the effective speed v_{eff} of the colloid in the optical trap

$$v_{eff}(t) = -\frac{\kappa \Delta x(t)}{6\pi\eta r} + u_e E(t)$$

where $\Delta x(t)$ is the maximum excursion of the colloid from the optical trap center. The following schematic summarizes the basic idea of the setup ((Otto et al., 2008))

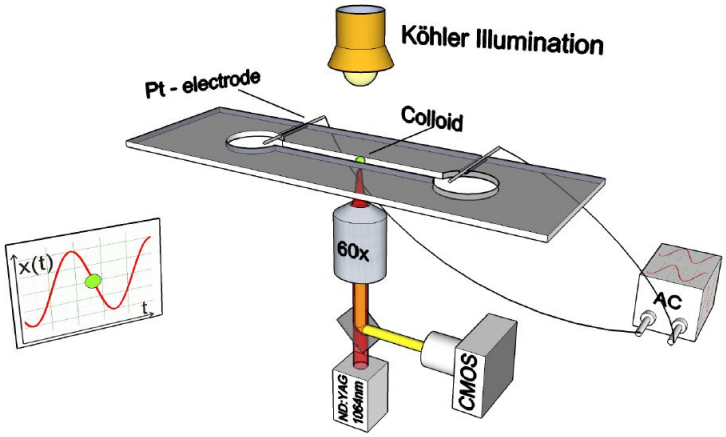

If $E(t)$ oscillates with frequency f, the average velocity over a full period is $v_{eff} = 4\Delta X f$. It follows

$$v_{eff} = 4\Delta x f = -\frac{\kappa \Delta x(t)}{6\pi\eta r} + u_e E$$

and thus we get

$$|u_e| = \frac{4\Delta X f}{E} + \frac{\kappa \Delta X}{6\pi\eta r E}$$

and $\Delta X/E$ can be simply extracted from the data. Assuming that we can use the ζ-potential which is true for frequencies of a few 100 Hz and lower we get

$$\zeta = \frac{\eta}{\epsilon_r}\epsilon_0 u_e.$$

Typical experimental data on colloids with radius $r = 1.11$ μm in 1 mM KCl at pH=8 at $f = 80$ Hz. The electrophoretic mobility is extracted from the gradient of the fit to the experimental data. This measurements can be performed on a single colloid. The amplitude of the motion at lowest field strength is only 1 nm. The data leads to a ζ-potential of 33 mV. A typical result for the linear dependence of the movement as a function of electric field is shown below (Otto et al., 2008)

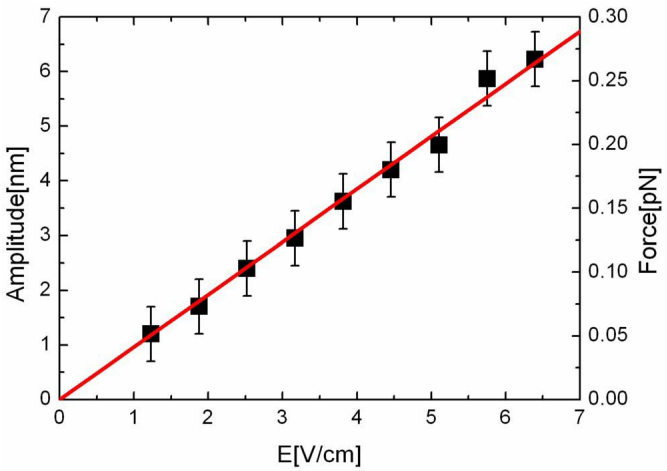

These experiments are performed at a distance of around 50 micron from any surface, to exclude any significant corrections to the drag coefficient of the colloidal particles.

6.6.4 Influence of electroosmosis on single colloid electrophoresis

The data presented in the graph above is almost perfectly linear and shows that this interpretation works. However when investigating the frequency dependence of this effect we find (Semenov et al., 2009)

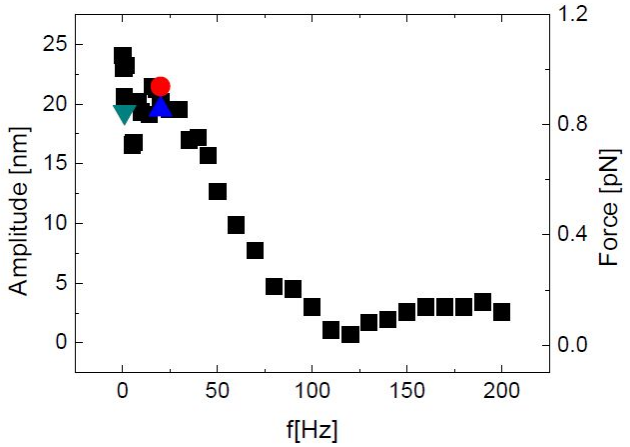

which is non-linear. The reason is that - as any real system - we have to consider the charges on the wall of the measurement chamber which gives rise to an electro-osmotic flow with flow velocity

$$veof = -\frac{\epsilon_r \epsilon_0}{\eta}\zeta$$

which is exactly the same as for the electrophoretic case except the opposite sign. So every fixed charges give rise to an EOF and thus in a real experiment we have charged glass surfaces. However, the frequency dependence shown above already hints that there is a straightforward solution. In order for the EOF to influence the colloid motion the water has to start moving. You can then define a characteristic length scale for the coupling given by

$$l_{eof} = \sqrt{\frac{\eta}{2\pi frho}}$$

where ρ is the electrolyte density. With the numbers from above we can estimate the coupling length to be 90 micron at $f = 20$ Hz and 45 micron at $f = 90$ Hz. Since the colloid is held more than 50 micron above the surface electroosmosis is diminished in this situation as indicated by the flattening of the experimental data. This finding can be further tested when the colloid is held closer to the surface we would expect a stronger influence of the EOF and thus a change in amplitude

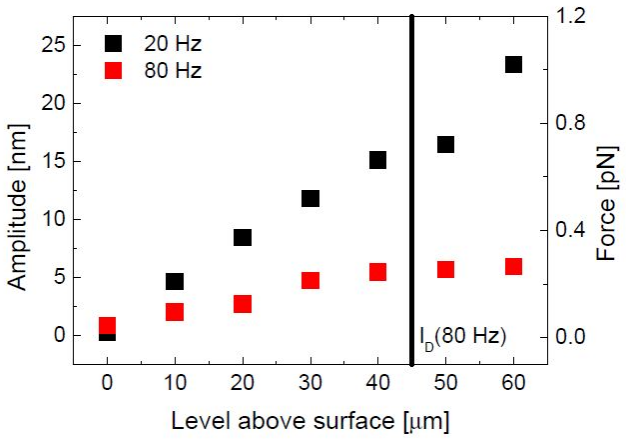

it is obvious that the influence of the EOF is detectable until the end of the measurements range while for the 80 Hz it is only measurable at 30 micron and less.

6.7 Electrophoretic separation of DNA molecules

The separation of DNA molecules by gel electrophoresis the process of driving the molecules through a dense network of cross-linked polymer with an applied electric fieldcounts among the most important techniques in biochemistry and molecular biology (Viovy, 2000)(Zimm and Levene, 1992). Despite the importance of the applications of DNA electrophoresis, however, the fundamental underlying mechanisms responsible for separation have not been fully elucidated, and doing so represents a substantial challenge. Conceptually, it requires understanding the interplay between polymer dynamics, electroosmosis, the topology of the gel and, in many cases, specific interactions between the DNA and the gel matrix. Experimentally, elucidating the role of these different contributions requires probing at or near the molecular scale. In addition to the fundamental interest from the point of view of polymer science and soft matter physics, present attempts to better understand electrophoresis are motivated by our increasing ability to construct sophisticated fluidic systems for manipulating DNA and other macromolecules. Such understanding may provide the insight necessary for developing new separation methods capable of outperforming the traditional gel.

Because of its emphasis on quantitative understanding, the contemporary literature on DNA electrophoresis may be difficult to access for researchers from outside the field. In particular, it is often difficult to separate the well-understood basic ideas from further refinements and details aimed at improving quantitative accuracy. It is the aim of this section of the course to introduce some of the basic ideas while concentrating on conceptual under-

standing rather than quantitative accuracy of gel electrophoresis.

6.7.1 Gel electrophoresis

Gel electrophoresis is one of the most important separation techniques for long charged macromolecules. As you will show in one of the problem sheets, long DNA molecules are behaving as 'free-draining' coils if they are long enough (longer than ∼400 bp). This is a direct consequence that long polymer coils can be described with the ζ-potential and thus mobility is NOT depending on length. Separation can then be achieved by letting the polymer migrate in a gel matrix containing a mesh of polymers. Obviously the interactions between the electrophoretically driven DNA and the mesh will depend on the length of the molecule. Gel electrophoresis was the basis for most sequencing techniques until 10 years ago and was used for the Human Genome Project. Recent advances in sequencing technology have replaced gel electrophoresis as a tool for ultra-fast sequencing but the technique is still of major importance for the separation of macromolecules by length, mass and ζ-potential.

In order to produce a gel one can use molecules extracted from cell walls of agarophyte red algae. The agarose monomer and a typical mesh (SEM image) is shown below

Agarose monomer

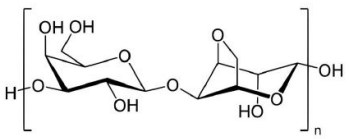

Agarose gel in dried condition

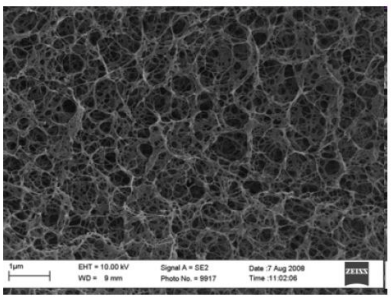

and effectively creates a network of pores. This system is very similar to concentrated polymer solutions. The DNA moves through this gel by driven diffusion. The mobility of the polyelectrolyte is controlled by the effective pore diameters. The pore diameters can be simply controlled by the density of agarose in the water when the gel is formed.

6.7.2 Polymer dynamics - Rouse model

In the simplest approach we can assume that a long polymer can be described as a string of N beads connected by freely jointed chain. The monomers can move through each other. Each bead has a friction coefficient β and thus the diffusion coefficient in the Rouse model of the polymer is just $D_R = k_b T/N\beta$. The Rouse time τ_R can then be defined as the time it takes the chain to diffuse

along its end-to-end distance R_N. For an ideal chain we get

$$\tau_R = \frac{\beta b^2}{6\pi^2 k_B T} N^2.$$

The characteristic time τ_0 for a monomer is roughly given by

$$\tau_0 \approx \frac{\beta b^2}{k_B T} \text{and thus } \tau_R \approx N\tau_0$$

.

There are obvious problems with this model since we assumed an ideal chain, unrealistic hydrodynamics (beads are independent) and there are no knots. So a more realistic approach taking into account the hydrodynamic by defining a no-slip boundary condition on the chain we get the Zimm model. Here$\beta \approx \eta r$ of the monomers and thus the Zimm diffusion coefficient D_Z is

$$D_Z = \frac{k_B T}{\eta R} \approx \frac{k_B T}{\eta b n^\nu}$$

where ν is the Flory-exponent which is depending on the chain characteristic. For $\nu - 0.5$ we have an ideal chain while with $\nu = 0.588 \approx 3/5$ we can describe a self-avoiding chain.

The Zimm relaxation time τ_Z is then

$$\tau_Z \approx \frac{R^2}{D_Z} \approx \frac{\eta}{k_B T} R^3 \approx \frac{\eta b^3}{k_B T} N^{3\nu} \approx \tau_0 N^{3\nu}.$$

The main difference to the Rouse time is the slightly weaker N dependence of the τ_Z compared to τ_R.

The polymer dynamics can also broken down into sub-chains which behave in the same way as the entire chain. There are N modes of the chain depending of the number of monomers $p = 1, 2, ..., N$ we get

$$\tau_p = \tau_0 \left(\frac{N}{p}\right)^2.$$

One can then get the mean square displacement of a segment with p monomers

$$< |\underline{r}_j(t) - \underline{r}_j(0)|^2 > \approx b^2 \frac{N}{p} \approx b^2 \left(\frac{\tau_p}{\tau_0}\right)^{1/2}$$

which is directly related to the relaxation time τ_p of the relaxation modes. At times below the Rouse time ($\tau_0 < t < \tau_R$) this is

$$< |\underline{r}_j(t) - \underline{r}_j(0)|^2 > \approx b^2 \left(\frac{\tau_p}{\tau_0}\right)^{1/2}.$$

For Fickian diffusion one would get

$$< |\underline{r}(t) - \underline{r}(0)|^2 >= 6Dt.$$

Thus in the Rouse regime the mean-square displacement is subdiffusive as for the Zimm modes which by following the same arguments is given by

$$< |\underline{r}_j(t) - \underline{r}_j(0)|^2 > \approx b^2 \left(\frac{\tau_p}{\tau_0}\right)^{2/3} \text{ for } \tau_0 < t < \tau_Z.$$

6.7.3 Reptation

In a gel the Zimm and Rouse models have to be modified since the chain segments cannot move independently from one another. This is very similar to the situation to a polymer melt of entangled chains which can overlap and cannot cross each other. For polymer melts Edwards developed the reptation model which assumes that the chain is moving in a tube defined by the surrounding chains. The tube diameter r_t is given by $r_t \approx b\sqrt{N_e}$ where N_e is the averaged number of monomers between two entanglements. r_t is also known as the entanglement length. Moving from the concept of monomers to a more coarse grained interpretation of the chain one can define the extension of the Edwards tube R_0 as

$$R_0 \approx r_t\sqrt{N}N_e \approx b\sqrt{N}.$$

One can also define a coarse grained contour length of the chain that is closely related to r_t and N_e

$$< L > \approx r_t \frac{N}{N_e} \approx \frac{b^2 N}{r_t} \approx \frac{bN}{\sqrt{N_e}}.$$

The diffusive motion in this tube is called reptation and the diffusion coefficient is the Rouse diffusion coefficient $D_c = k_B T/N\beta$. With this we can define the reptation time $\tau_r ep$ for the chain to diffuse out of its tube of length $< L >$

$$\tau_{rep} \approx \frac{< L >}{D_c} \approx \frac{\beta b^2}{k_B T}\frac{N^3}{N_e} = \frac{\beta b^2}{k_B T} N_e^2 \left(\frac{N}{N_e}\right)^3$$

with the lower limit for the reptation time for $N = N_e$

$$\tau_e \approx \frac{\beta b^2}{k_B T} N_e^2$$

and thus

$$\frac{\tau_{rep}}{\tau_e} \approx \left(\frac{N}{N_e}\right)^3.$$

Now we can write down the mean-square displacements of the entangled case in the same way as in the free Rouse case. At $t < \tau_e$ this is the motion of the monomers:

$$< |\underline{r}_j(t) - \underline{r}_j(0)|^2 > \approx b^2 \left(\frac{t}{\tau_0}\right)^{1/2}.$$

At time $\tau_e < t < \tau_R$ the motion is confined by the reptation tube and thus we get a new coordinate $\underline{s}_j$ along the tube

$$< |\underline{s}_j(t) - \underline{s}_j(0)|^2 > \approx b^2 \left(\frac{t}{\tau_0}\right)^{1/2} \approx r_t^2 \left(\frac{t}{\tau_e}\right)^{1/2}$$

related to the reptaion tube diameter r_t. The reptation tube itself is a random walk with step length r_t

$$< |\underline{r}(t) - \underline{r}(0)|^2 > \approx r_t \sqrt{< |\underline{s}_j(t) - \underline{s}_j(0)|^2 >} \approx r_t^2 \left(\frac{t}{\tau_e}\right)^{1/4}$$

which is even slower than the unrestricted Rouse motion, as expected in entanglement. Finally we for times longer than the rouse time $\tau_R < t < \tau_{rep}$ the whole chain is moving and thus all segments are correlated. Thus the whole chain diffuses in the reptation tube with the curvilinear diffusion coefficient D_c

$$< |\underline{s}(t) - \underline{s}(t)|^2 > \approx D_c t \approx b^2 N \frac{t}{\tau_R} \approx r_t^2 \frac{N}{N_e} \frac{t}{\tau_R}$$

whilce the random walk of the reptation tube is

$$< |\underline{r}(t) - \underline{r}(0)|^2 > \approx r_t \sqrt{< |s_j(t) - s_j(0)|^2 >} \approx r_t^2 \left(\frac{N}{N_e}\right)^{1/2} \left(\frac{t}{\tau_R}\right)^{1/2}.$$

And finally at $t > \tau_{rep}$ the chain motion averages over all tubes and Fickian diffusion has to be recovered $< |\underline{r}(t) - \underline{r}(t)|^2 >= 6 D_{rep} t$ where $D_{rep} \approx \frac{R_0^2}{\tau_{rep}} \approx \frac{k_B T}{\beta} \frac{N_e}{N^2}$.

The four regimes can be summarized into a plot

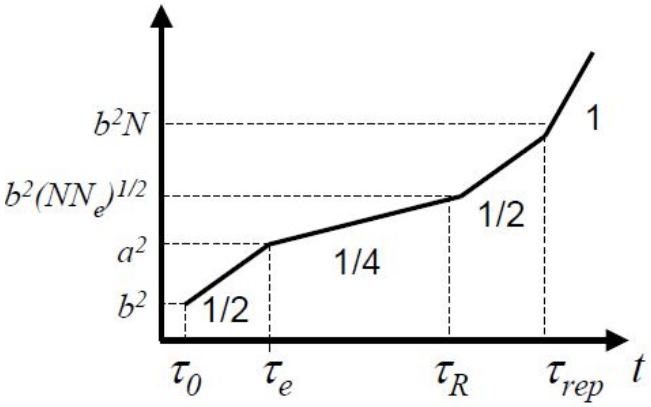

indicating the sub-diffusive motion at small time scales while the scaling with t^1 is recovered for long times. At these long time scales polymers behave as simple liquids while at the shorter time scales dynamics are slowed down due to entanglement, and finally on the monomers the connectivity of the segments described by Rouse and Zimm determines the polymer dynamics.

6.7.4 Gel electrophoresis

Charged polymer diffuses through a gel due to applied potential (Viovy, 2000). The reptation picture describes polymer motion very well if the field strength is low and the polyelectrolyte is long enough compared to the pore size of the gel. DNA moves in the direction of the applied field as expected. In contrast to the free solution electrophoresis we expect a $1/L$ dependence of mobility as well as a dependence on the pore size of the gel. This is experimentally observed

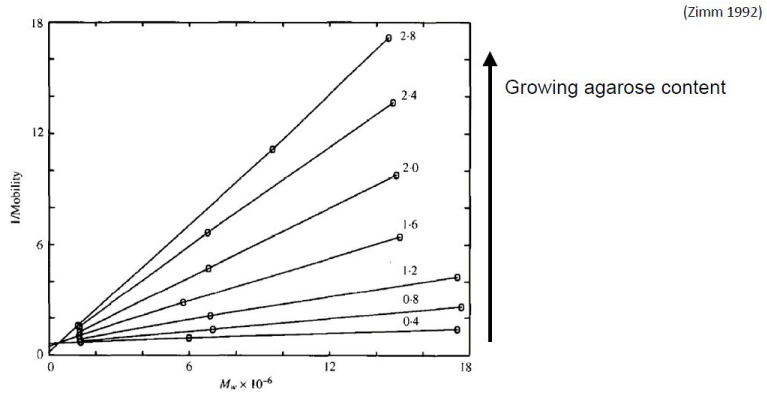

and in general holds for DNA which is much longer than the Debye screening length. At the same time the chains should be longer than the typical pore diameter in the gel. For very long polymers model breaks down as trapping and knots become more and more dominating. As shown in the article by (Zimm and Levene, 1992), the mobility of DNA is depending on length and electric field

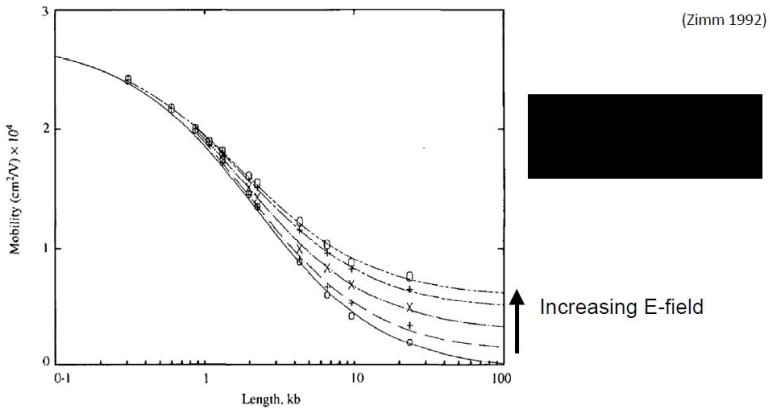

The black arrow on the right denotes the increasing electric field strength. Since for very short DNA the mobility is almost the same for all length the polyelectrolytes have to be separated over long timescales. For separation of DNA with a length of several tens of kilo-basepairs in length there are better methods like pulsed field gel electrophoresis. There are also intensive efforts to replace these gels with artificial gels made by semiconductor nanotechnology.

6.8 Resistive-pulse sensing

Resistive-pulse sensing is a brilliant and simple idea for the label-free detection of single molecules in solution. It is in fact using a single pore not a mesh to detect the presence of a single particle or molecule in solution. The sensing principle is shown below (adapted from (Bezrukov, 2000))

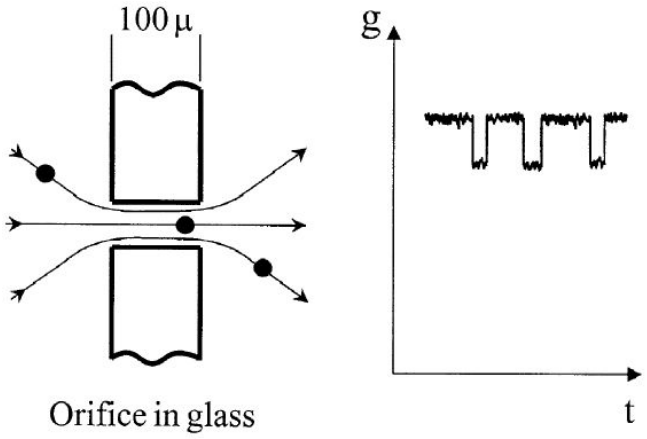

This technique was invented already 60 years ago and the first patent was issued in 1953. This is the basis of the Coulter counter for the detection of counting of small particles in solution.

Recently there is renewed interest in the technique which a result of improvement of the Coulter counter principle down to true molecular scale. This was demonstrated first by sensing single polymers in solution. This first success lead to increased interest and the first detection of RNA and DNA molecules a few years later (Kasianowicz et al., 1996). This latter work, in particular, sparked the imagination of a large number of researchers since it offered a completely new approach to ultra-fast sequencing technology with the possibility of long read lengths. The advancement of the nanopore field was further fueled by the development of solid-state nanopores making use of the powerful arsenal of techniques developed for nanotechnology. In 2010 several groups, almost at the same time, demonstrated graphene nanopores for biosensing both experimentally and theoretically for DNA sequencing (Garaj et al., 2010).

For label-free sensing of single molecules, the availability of suitable nanopores is crucial. Although a number of methods exist to fabricate porous structures and filter membranes, obtaining a single hole in a thin membrane is a significant challenge (Dekker, 2007). There are two main sources for nanoporesbiological protein pores, extracted, for example, from bacteria like Escherichia coli (e.g. outer membrane protein F) or Staphylococcus aureus (e.g.a-haemolysin), and fabricated ones derived from silicon nanotechnology (Dekker, 2007). Despite the abundance of biological nanopores, it was a challenge to find a nanopore that is stable for hours and has large enough inner diameter to enable macromolecules like DNA to pass through them. To date, the most important sensing pore is without doubt a-haemolysin, which owing to its commercial availability is used for sensing in an ever-growing number of laboratories around the world. One striking feature of biological nanopores is their atomic precision in assembly while providing almost perfect repeatability of nanopore structure. Another main

advantage of biological nanopores over man-made structures is the ability to use genetic modification to fine tune the nanopore properties. This enables almost a free choice over their properties down to the single amino acid and even atomic level by mutagenesis. In effect, this was used in one of the earliest demonstrations of control of DNA in a nanopore whereby a single DNA strand in the pore was used to immobilize translocating DNA. A notable disadvantage, however, is most biological nanopores have diameters of less than 2 nm. This is suitable for sensing and sequencing of single-stranded DNA, RNA and unfolded protein chains but impedes the sensing of proteins in their native folded state or even double-stranded DNA. The search for larger diameter biological nanopores that possess tunable diameters is ongoing. Some of the shortcomings of biological nanopores have been addressed by the use of solid-state nanopores, with tunable diameters. Solid-state nanopores can be made in a variety of membrane materials by means of a focused electron or ion beams. The most common as carrier materials for the nanopores are silicon nitride membranes. Diameter, length and shape are only limited by the thickness and robustness of the membrane in salt solutions. For silicon nitride membranes, the thickness was reduced recently to a few nanometres, while with graphene nanopores, the nanopore length could be cut down to a single atomic layer (Garaj et al., 2010). Recently, glass nanocapillaries were shown to be a relatively simple alternative approach for DNA sensing.

The nanopore connects two reservoirs containing aqueous salt salt solution. A voltage is applied by means of silve/silve-chloride electrodes and the ionic current through the nanopore is measured. A schematic of a measurement is shown below (adapted from (Dekker, 2007)

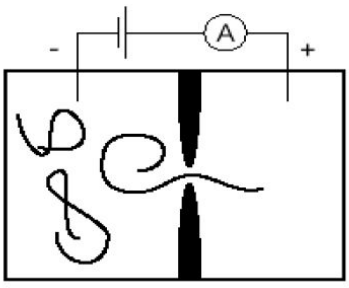

The nanopore can be estimated as a cylindrical channel with length h and radius r in a membrane.

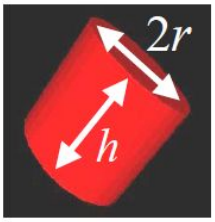

$$R_{\text{pore}} = \frac{1}{\sigma_{KCl}(T)}\left(\frac{h}{\pi r^2}\right)$$

For this system we can easily write down the total resistance R_{cyl}

$$R_{cyl} = \frac{1}{g_{salt}(T)} \left(\frac{h}{\pi r^2} + \frac{1}{2r} \right)$$

where g_{salt} is the temperature-dependent ionic conductivity of the respective aqueous salt solution. The first term is the resistance due to the central part of the channel while the second part describes the so called access resistance $1/2r$ (Hall, 1975). This is due to the finite drop of voltage outside of the nanopores and effectively leads to an increased length. This also increases the sensing length of the nanopore and reduces the spatial resolution of the detection.

This formula ignores the influence of the surface charge of the nanopore material (will be discussed in the lectures). At high salt concentration above 100 mM ionic strength in the solution this is valid as bulk conductance dominates - however at lower salt concentrations surface corrections become important when the Debye layers start to overlap.

When a molecule like DNA is in the nanopore the number of charge carrier is changed and leads to an increase in the resistance of the nanopore - hence the term resistive-pulse technique. The total change in conductance ΔG is given by

$$\Delta G = \frac{1}{L_{pore}} \left(-\pi r_{DNA}^2 (u_K + u_{Cl}) n_{KCl} \right)$$

where u_K and u_{Cl} denote the mobility of the cat- and anions and L_{pore} is a parameter describing the nanopore with an effective length including the access resistance.

6.9 Tether force in electrophoresis

We focus on a single aspect of electrophoresis, the so-called tether force. This is the force that is needed to hold a charged object in place against the action of an externally applied electric field. This situation loosely corresponds to a DNA molecule that is temporarily trapped in a metastable configuration inside a gel (Keyser et al., 2010).

In order to focus on the key concepts, we first introduce a system with the very simple geometry

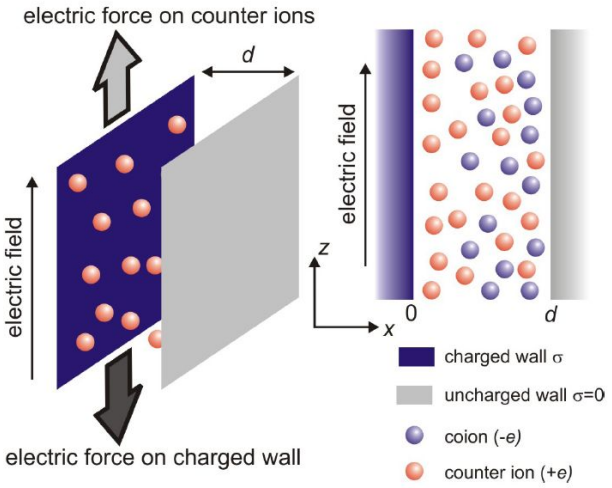

The system consists of a charged surface with a uniform surface charge density s separated from a second, parallel surface that is electrically neutral. For most systems of interest, σ has a negative value; while this is not assumed in our derivation, the plots in the figures correspond to this case. The charged surface has a surface area A, and the surfaces are separated by a distance d. We assume that the lateral dimensions of the charged surface are sufficiently large that edge effects can be neglected; under these conditions all of the relevant equations become one-dimensional. The volume between the two planes is filled with an electrolyte, which is in diffusive equilibrium with a bulk reservoir. We take the electrolyte as consisting of water containing a number density n_0 of a fully dissociated monovalent salt. A good example of the latter is potassium chloride (KCl), which dissociates into K^+ and Cl^- ions in water. This implies that in bulk solution there is a number density n_0 of both positive ions (also known as cations) with charge $+e$ and negative ions (anions) with charge $-e$, where e is the charge of the electron. We treat water as a homogeneous medium with permittivity $\epsilon_w = 80\epsilon_0$. A uniform electric field with magnitude E is applied parallel to the surface and permeates the region between the surfaces. The direction of this electric field is defined as z, while the direction perpendicular to the planes is x (with $x = 0$ corresponding to the position of the charged surface and $x = d$ to that of the neutral surface). We will further assume that s is small and that d is large, as defined more quantitatively below.

The ion distribution in the double layer is most commonly described within the so-called PoissonBoltzmann formalism. At equilibrium, the average concentration of charged molecules at position x is assumed to follow the Boltzmann distribution,

$$n_{\pm}(x) = n_0 e^{\mp e\phi(x)/k_B T}$$

with $\phi(x)$ the local average potential and n_+ and n_- are the local number densities of cations and anions, respectively. We have also

introduced the convention that $\phi(x) = 0$ corresponds to the bulk reservoir far from any charged object, where $n_+ = n_- = n_0$. In this section we will further assume that $\phi(x)$ is much smaller than k_BT so that the Poisson-Boltzmann equation can be linearized. And thus

$$n_\pm(x) = n0(1 \mp \frac{\phi(x)}{k_BT})$$

. (3) In order to determine self-consistently the electrostatic potential $\phi(x)$ we employ the Poisson equation from electrostatics, $\nabla^2\phi(x) = \rho(x)/\epsilon_w$. Here $\rho(x) = e(n_+(x) + n_-(x))$ is the charge density. The result is a differential equation that can be solved for the electrostatic potential $\phi(x)$,

$$\frac{d^2\phi(x)}{dx^2} = \frac{k_BT\epsilon_w}{2e^2n_0}\phi(x) = \frac{\phi(x)}{\lambda^2}$$

. In the last step we introduced the Debye length again, defined as $\lambda = \sqrt{k_RT\epsilon_w/2e^2n_0)}$. The Debye length depends on fundamental constants and the salt concentration of the solution. For pure pH 7 water at room temperature (which contains 10^7 M of H+ and OH^- ions), $\lambda \approx 1$ μm. Under typical physiological conditions (approximately 0.1 M of monovalent salt), $\lambda \approx 1$ nm.

The general solution for this equation you saw now several times already $\phi(x) = Ae^{-x/\lambda} + Be^{+x/\lambda}$. With the boundary conditions at $x = 0$ and $x = d$ $d\phi(0) = -\sigma/\epsilon_w$ and $d\phi(d)/dx = 0$ we can easily write down the solution for the electrostatic potential

$$\phi(x) = \frac{\sigma\lambda}{\epsilon_w}\left(\frac{e^{-x/\lambda} - e^{-2d/\lambda+x/\lambda}}{1 + e^{-2d/\lambda}}.\right)$$

For $d \gg \lambda$ we get

$$\phi(x) = \frac{\sigma\lambda}{e^{-x/\lambda}}.$$

This is the case when the neutral wall is far enough from the charged wall to ensure that there is no influence on the charge distribution. This situation is illustrated below (adapted from (Keyser et al., 2010))

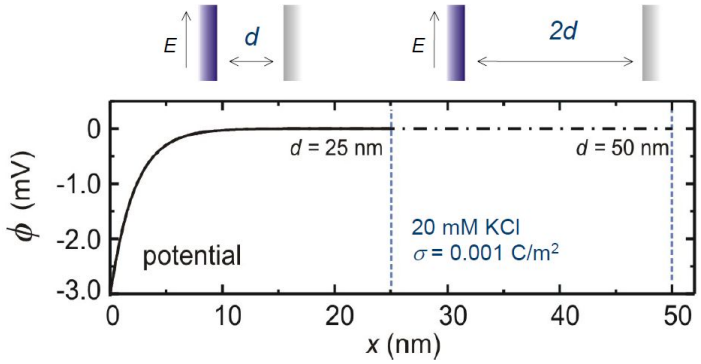

Our result shows that electrostatic interactions decay to zero in electrolytes over a characteristic distance λ.

We already now from our discussion of the electric double layer that both charges can be present in the screening layer especially at low surface charges. Thus in this limit the ions are distributed as Boltzmann factors:

$$n_{\pm}(x) = n_0 \mp \frac{\sigma}{2e\lambda} e^{-x/\lambda}.$$

The net charge density in the diffuse layer is

$$\rho(x) = -\frac{\sigma}{\lambda} e^{-x/\lambda}.$$

Like the potential $\phi(x)$, the charge density $\rho(x)$ drops to zero with increasing distance from the charged surface with a decay length λ. Integration of this equation with respect to x also directly demonstrates that the total charge in the diffuse layer is equal and opposite to that of the surface being screened.

In the presence of an electric field E, each ion moves with an average drift velocity $v_{eof} = u_{eof}E$. u_{eof} has a different value for different species of ions, and it is positive for cations and negative for anions. Ions in a solvent move at constant velocity and do not accelerate like charges in vacuum because they experience drag from the solvent. By Newtons third law, each ion therefore exerts a reaction force on the solvent. Averaged over a microscopic volume of bulk solution large enough to contain several ions, however, the net force averages to zero since the solution is neutral and the reaction forces from cations and anions exactly cancel each other. This cancelation does not occur near a charged surface. As there is an equal and opposite net charge next to it in the double layer. An electric field thus exerts gives rise to the electro-osmotic flow introduced above.

In order to solve the flow problem, we make further approximations. We are interested in describing flows that vary on length scales of microns or less. At these length scales and for typical velocities encountered in electroosmotic flows, the Reynolds number is very small and all flows are expected to be laminar. Furthermore, from symmetry the fluid velocity can only be oriented parallel to the electric field (z-direction) and can only vary perpendicular to the surface (x-direction). Under these conditions the NavierStokes equations that describe fluid motion reduce to the simple form

$$\frac{d^2 v_{eof}}{dx^2} + \frac{\rho(x)E}{\eta} = 0$$

where $\rho(x)E$ is the force per unit volume exerted by the electric field.

Using $\rho(x)$ this simplified Navier-Stokes equation can be directly integrated

$$v_{eof} = \frac{E\sigma\lambda}{\eta} e^{-x/\lambda} + Bx + C.$$

With the susual no-slip boundary conditions at the two walls $v_{eof}(0) = v_{eof}(d) = 0$ the flow profile is

$$v_{eof} = -\frac{E\sigma\lambda}{eta}\left(1 - e^{-x/\lambda} - \frac{x}{d}\right).$$

This is shown below together with the distribution of ionic species for walls separated by $d = 25$ nm and $d = 50$ nm, respectively.

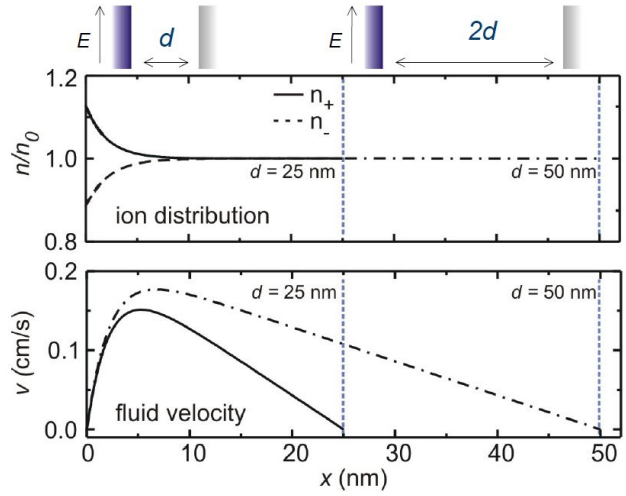

We now have all of the ingredients required to calculate the tether force F_{mech} that must be applied to hold the charged surface in place against the action of the electric field. The relevant forces are

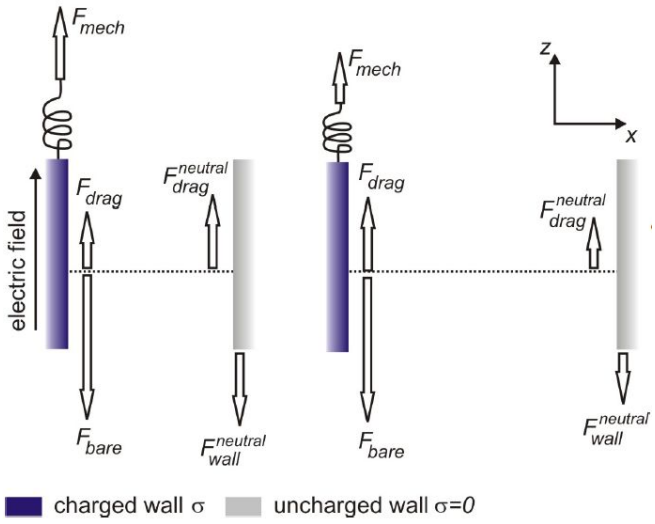

where the superscripts σ and 0 refer to the charged and uncharged surfaces, respectively. The total force applied to the charged surface by the electric field can be decomposed into two components that always act simultaneously. First, the electric field acts directly on the charges of the surface. We refer to this component as the bare force, F^{σ}_{bare}, since this is the force that would

be experienced by the bare surface if it was suspended in vacuum. This force follows simply from Coulombs law and is given by $F^{\sigma}_{bare} = A\sigma E$. The electric field simultaneously acts on the oppositely charged screening cloud and sets up an electroosmotic flow, as discussed in the previous paragraphs. Because this flow causes the fluid to be sheared at the boundary with the charged surface, it exerts a drag force F^{σ}_{drag} on the charged surface whose value is given by Newtons relation as

$$F^{\sigma}_{drag} = a\eta \left| \frac{dv_{eof}(x)}{dx} \right|_{x=0} = -ae\sigma \left(1 - \frac{\lambda}{d}\right) = -\left(1 - \frac{\lambda}{d}\right) F^{\sigma}_{bare}.$$

The mechanical tether force follows directly from the above and is given by

$$F^{\sigma}_{mech} = -F^{\sigma}_{elec} = -(F^{\sigma}_{bare} + F^{\sigma}_{drag}) = -AE\sigma\frac{\lambda}{d}.$$

This result contrasts strongly with what would be expected in the absence of the drag force induced by the screening charge: in that case we would expect $F^{\sigma}_{bare} = -AE\sigma$, which is larger than the correct answer by a large factor, d/λ.

Our calculation thus indicates that drag from the counterions, far from being a minor correction, is in fact a dominant factor in determining the magnitude of electrophoretic forces. Furthermore, its influence does not depend solely on local properties in the vicinity of the charged surface, but instead encompasses all aspects of the environment that modify the electroosmotic flow. This is made explicit by the appearance of d in our equation for F^{σ}_{mech}. It is also manifest in the distribution of ions and potential $\phi(x)$ which are essentially independent of d (so long as $d \gg \lambda$). However the flow profile shown above is strongly affected by the value of d.

Further insight can be gained by considering the uncharged wall. Although the electric field does not act directly on this wall, the electroosmotic flow does exert a drag force on it since the shear stress is non-vanishing at $x = d$. Following the same steps as above we have for this force

$$F^{0}_{mech} = -A\eta \left| \frac{dv_{eof}(x)}{dx} \right|_{x=0} = AE\sigma\frac{\lambda}{d} = -f^{\sigma}_{mech}.$$

The forces on the two walls are thus equal and opposite, which may at first appear surprising. It is however easily understood by considering that the electric field exerts no net force on the system as a whole since the force exerted on the charged wall is exactly compensated by the force on its screening charge. Any external mechanical force on the charged wall must therefore be balanced by a second external force. Equivalently, one can consider that the total force on the screening charge is transmitted to the two surfaces through shear in the fluid. The fraction that reaches

the uncharged surface is λ/d, while the fraction that reaches the charged surface is $(1 - \lambda/d)$. It follows directly that $F^{\sigma}_{mech} = -(F^{\sigma}_{bare} + F^{\sigma}_{drag} = -F^{0}_{mech}$.

Our result predicts that the tether force F^{σ}_{mech} goes to zero as the distance d is increased toward infinity, and therefore that there is no tether force on a charged surface far from any boundary. This counterintuitive result is actually an artefact caused by the approximations that we have made. In particular, we have neglected edge effects and essentially treated the charged surface as infinite. For a finite-sized surface, a small but non-zero force remains due to a back flow of fluid on the size scale of the surface itself. More generally, we have neglected inertial effects by using only the Stokes equation to describe the motion of the fluid. On large enough length scales, however, inertia becomes relevant and this approximation breaks down.

In simple electrostatics, the force on a charged object is proportional to its charge multiplied by the local electric field. As we saw in the previous section, on the other hand, the net tether force on a charged object in an electrolyte is not simply given by its bare surface charge density, and is instead much smaller due to an important contribution from the screening layer. To an observer who is unaware of what is happening in solution and who simply measures the tether force in response to a known electric field, however, it is natural to describe the force as resulting from an effective surface charge density σ_{eff}, such that $F^{\sigma}_{mech} = -A\sigma_{eff}E$, with $|\sigma_{eff}| < |\sigma|$. σ_{seff} is thus also defined by the geometry of the experiment and $\sigma_{eff} = \sigma(\lambda/d)$.

The effective charge, as introduced above, is a well-defined quantity, both experimentally and theoretically. Nevertheless, the use of the concept of effective charge should usually be discouraged or come with a strong disclaimer. There are several reasons for this. First, the effective charge does not correspond to a physical charge, but rather includes factors that depend on the geometry of the hydrodynamic environment around the charged object. Second, because the effective charge is not an intrinsic property of the charged object, instead depending on geometry parameters such as d, its value cannot be compared directly between different experimental configurations. Comparisons between tether force and electrophoretic mobility experiments are even more difficult, as the relation between the effective charges that are commonly defined in these two experimental situations is model-dependent. Third, the concept of effective charge is ineffective as a pedagogical tool: it has been our experience that, upon first encountering it, many readers are left with a vague notion that the effective charge consists of the bare charge of the object, minus some countercharge which is physically immobilized on the object. While this sort of complexation can certainly be an important contribution in real systems, thinking about electrophoresis solely in this manner ob-

scures the fact that the tether force is expected to be smaller than the bare value even if there are *no* immobile countercharges.

6.9.1 More complex situations

The above calculation holds so long as the surface charge density is sufficiently small that the condition $|\sigma| < k_B T \epsilon_w / e\lambda$ is satisfied. At higher surface charge densities, we have to solve the full Poisson-Boltzmann equation

$$\frac{d^2\phi(x)}{dx^2} = \frac{2en_0}{\epsilon_w} \sinh\left(\frac{e\phi(x)}{k_B T}\right).$$

Because of its non-linearity, this equation is considerably more difficult to solve. When $d \gg \lambda$, an analytical solution can nonetheless be obtained for the geometry with the two parallel plates

$$\phi(x) = \frac{2k_B T}{e} \ln\left(\frac{1+\gamma e^{-x/\lambda}}{1-\gamma e^{-x/\lambda}}\right)$$

with $\gamma = -\lambda_{GC}/\lambda + (1 + \lambda_{GC}^2/\lambda^2)^{1/2}$. Here we introduced a new parameter $\lambda_{GC} = 2k_B T \epsilon_w / (e|\sigma|)$ which is known as the GouyChapman length. Qualitatively, lGC is a measure of the strength of the electrostatic interactions between ions and the surface, with a small λ_{GC} corresponding to strong interactions.

This result for $\phi(x)$ is shown below for a range of values of the surface charge σ. From bottom to top, the curves correspond to values of the surface charge density s of 0.001, 0.003, 0.005, 0.01, 0.025, 0.05, 0.1, 0.5 and 1.0 Cm^{-2} in 20 mM KCl at 300 K. For low values of σ, the curves follow the DebyeHückel result. Deviations from this linear behavior are evident at low x for the four topmost curves. The inset shows the counter- and coion distribution for 0.025 Cm^{-2} at 20 mM KCl. The coions are depleted in close proximity to the surface. In contrast, the number density of counterions is ten times higher than in bulk solution.

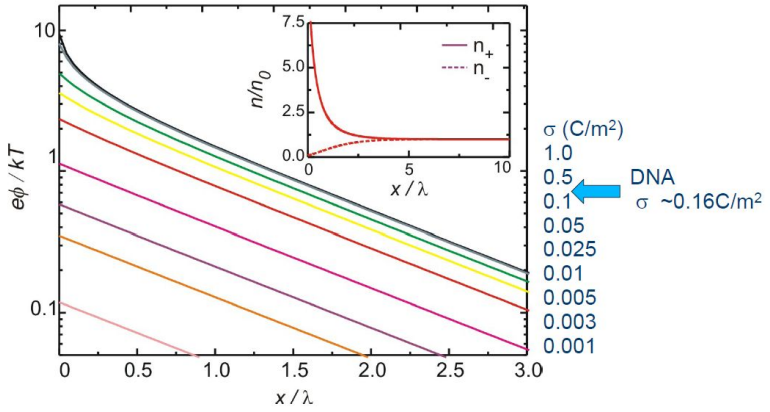

Far from the surface, the potential decays exponentially with a characteristic length λ for all values of σ. For large enough σ, however, the potential far from the surface no longer increases with

increasing σ. Instead, its value becomes independent of the magnitude of σ and takes on the form $\phi(x) = \pm(4k_BT/e)\exp(-x/\lambda)$. Correspondingly, for large enough σ the distribution of counter- and coions far from the surface also becomes independent of the magnitude of σ. In this case all of the additional screening charge is located close to the charged surface, as evidenced by the continued increase of $\phi(x)$ with increasing s in this region. The size of this region is of the order of the GouyChapman length, λ_{GC}. More precisely, at a planar surface and under conditions of low bulk electrolyte concentration ($\lambda_{GC} \ll \lambda$), half of the counterions reside within λ_{GC} from the surface. In water at room temperature, λ_{GC} is only 0.24 nm for a high surface charge density of s = 0.16 Cm^{-2} (corresponding to 1 e nm^{-2}). Although its value scales inversely with σ, λ_{GC} remains a molecular scale length for many charged systems. Qualitatively, the charge screening a highly-charged surface can thus be thought of as consisting of two components: a diffuse layer, which extends a few Debye lengths into the solution, and a more compact layer very close to the surface. The diffuse layer is composed of more-or-less symmetric distributions of excess counterions and missing coions, whereas the more compact layer is composed predominantly of counterions. The latter results from the non-linearity inherent in eqn (1): while the coion concentration cannot be suppressed below zero, the degree of counterion enrichment can be arbitrarily high. Even for a surface with $\sigma = 0.025$ Cm^{-2} (corresponding to $e\phi/k_BT \approx 2$) the ion distributions show an excess of counterions n_+ whereas coions n_- are completely depleted in the screening layer.

In describing the ionic screening of charged, stiff biopolymers such as DNA, a common approximation is to treat the molecule as a charged, solid cylinder. Analogous to the discussion of the infinite plane above, we focus here on a charged cylinder with radius a and surface charge density σ positioned in the center of a larger, uncharged cylindrical cavity with radius R. For such a problem with cylindrical symmetry, the PB equation takes the form

$$\frac{1}{r}\left(r\frac{d\phi(x)}{dr}\right) = \frac{2en_0}{\epsilon_w}\sinh\left(\frac{e\phi(r)}{k_BT}\right) \approx \frac{\phi(r)}{\lambda^2}$$

where the last step corresponds to the DebyeHückel approximation. In this last case and for $R \ll \lambda$, the correspondingsolution for the potential is

$$\phi(x) = \frac{\sigma\lambda}{\epsilon_w}\frac{K_0(r/\lambda)}{K_1(R/\lambda)}$$

where K_0 and K_1 are the 0th and first order modified Bessel functions of the second kind, respectively. Analogous to the planar geometry, the potential decays exponentially away from the charged cylinder.

For a highly-charged surface, the linearization is no longer valid and the full PB equation must be solved. We only note that

the resulting solution exhibits the same qualitative features as for the case of a plane, and once again the screening charge can be broken into a diffuse layer, whose size is given by the Debye length, and a compact layer, characterized by the GouyChapman length. The amount of charge in the diffuse layer also saturates at a constant value with increasing s, while the remaining screening charge resides in the compact layer and consists primarily of counterions.

This separation into two components can be made more precisely in the special case of a line charge (a cylinder with R-0) with linear charge density r and in the absence of supporting salt ($n_0 = 0$). In this case ions accumulate (or condense) on the line charge, partly compensating its charge until its value decreases to a magnitude e/λ_B (where $\lambda_B = e^2/4\pi k_B T \epsilon_w$ is the Bjerrum length). The linear charge density of the condensed ions is thus $(|\rho| - e/\lambda_B)$, while the linear density of charge in the diffuse layer is the remaining e/λ_B. This result, known as Manning condensation, often serves as a first approximation for the composition of the double layer in more realistic cases. Double-stranded DNA, for example, has a charge density of $2e$ per base pair, corresponding to $\rho = 4.2e/\lambda_B$. This is well over the critical threshold for counterion condensation to occur, and as a first estimate a fraction $1 - 1/4.2 = 0.76$ of the charge can be expected to be screened by condensed counterions.

Following our discussion from above with the conclusion how forces are in fact generated and lead to the counter-forces slowing down DNA translocation or measured by a mechanical force transducer. We can make the following scheme for the situation of two concentric cylinders.

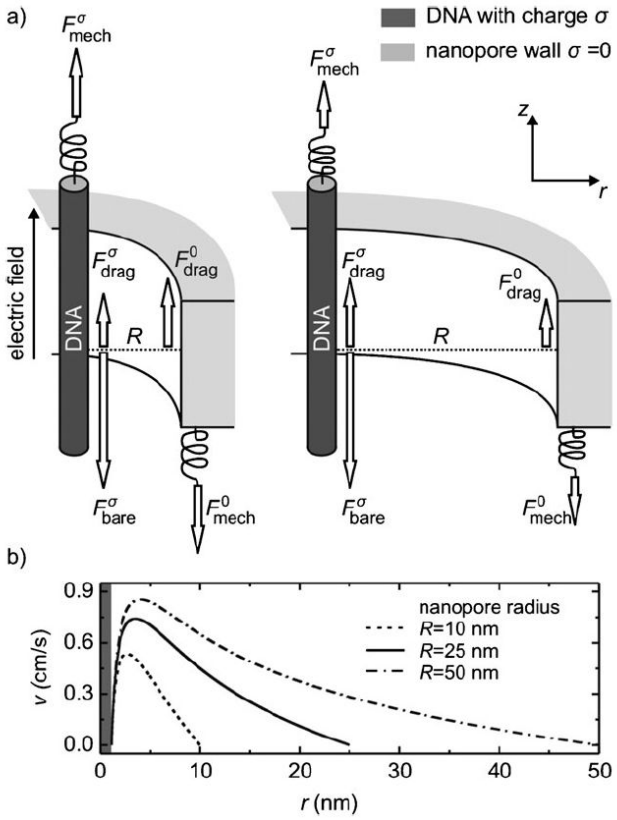

Force balance for DNA in the center of a nanopore with radius R. (a) Left: the balance of forces is qualitatively identical to the case of planar surfaces. Briefly, the electric field pulls the negatively charged DNA towards the bottom with a force $^{\sigma}_{bare}$, whereas the counterions experience a force in the opposite direction. This leads to drag forces F^{σ}_{drag}, acting on the DNA, and $^{0}_{drag}$, acting on the nanopore wall. The latter force is ultimately transferred to the rest of the experimental setup to which the pore is rigidly attached. The DNA is stalled by a tether force F^{σ}_{mech} applied to the DNA, while an equal but opposite force $^{0}_{mech}$ acts on the uncharged nanopore. Right: when the nanopore radius R is increased, the drag force on the DNA also increases. Correspondingly, the drag force on the nanopore F^{0}_{drag} and the tether force F^{σ}_{mech} decrease. (b) The flow velocity $v(r)$, calculated by numerically solving the full PB euqation and combining the result with the Stokes equation. The maximum flow velocity depends on the nanopore radius R.

Because the distribution of screening charge in the vicinity of a charged cylinder is qualitatively very similar to that near a surface, our discussion of electroosmotic flows and tether forces in Section 2 applies directly to the case of a cylinder. In particular, as illustrated above, here also the tether force is due to a combination of bare electrostatic force and a drag force from the counterions,

with the drag force being of comparable magnitude to the bare force. The cylindrical geometry only influences our analysis and conclusions at a quantitative level. For example, the figure above shows the fluid velocity $v(r)$ as a function of radial position r. Far from the charged cylinder, $v(r)$ exhibits a non-linear decay with increasing$r$, unlike our result for planar surfaces, leading to subtle differences in how the drag force is distributed between the two surfaces. However, this does not fundamentally change the interpretation of the tether force.

(Single-Molecule) Techniques

7

7.1 Introduction

In this section we will introduce some of the techniques that are mostly used for single molecule investigations. However, all of the experimental approaches can be employed in a wider range of fields. For instance the atomic force microscope is ideally suited to investigate any (non-conducting) surface with atomic or even sub-atomic resolution. Obviously it is thus suited for imaging applications from hard condensed matter and due to the possibility of operating in liquid environments to biological and soft matter physics. It developed into a main-stream imaging techniques that is used now in all sciences from Medicine to Physics.

There is considerable overlap between the measurement principles employed for the atomic force microscopes and optical tweezers, the second technique that we will discuss in this chapter. However, optical tweezers are ideally suited not for imaging applications but for mechanical measurements on single macro-molecules. They were absolutely essential for establishing that DNA and other polymers can be described by the models for polymers we discussed in this course.

Finally, magnetic tweezers will be discussed, which allow to measure forces in the sub-pN and even low femto-Newton range. This allows to probe entropic forces in detail and allow for an even more accurate assessment of both DNA-protein interactions as well as polymer models.

- Magnetic tweezers, technique: Gosse and Croquette "Magnetic Tweezers: Micromanipulation and Force Measurements at the Molecular Level", Biophys. J. (2002) (Gosse and Croquette, 2002)
- technical recipes: Muller and Engel, "Atomic force microscopy and spectroscopy of native membrane proteins" Nature Methods (2007) (Mueller and Engel, 2007)
- AFM background on trapping on surfaces: Bustamante and Rivetti, "Visualizing protein-nucleic acid interactions on a large scale with the scanning force microscope" Ann. Rev. Biophy. (1996) (Bustamante and Rivetti, 1996)
- comprehensive overview over most state of the art tech-

niques: Neuman, Block, "Optical Trapping", Review of Scientific Instruments (2004) (Neuman and Block, 2004)

- good review about single molecule studies: Bustamante et al. "Ten Years of Tension: Single Molecule DNA mechanics" Nature (2003) (Bustamante et al., 2003)

7.2 Atomic Force Microscopy

One of the most prominent tools for the detection and unraveling of single macromolecules is the atomic force microscope (AFM). The idea is very simply to 'feel' the atoms of a surface by a sharp needle, often manufactured from silicon. The measurement concept is shown below

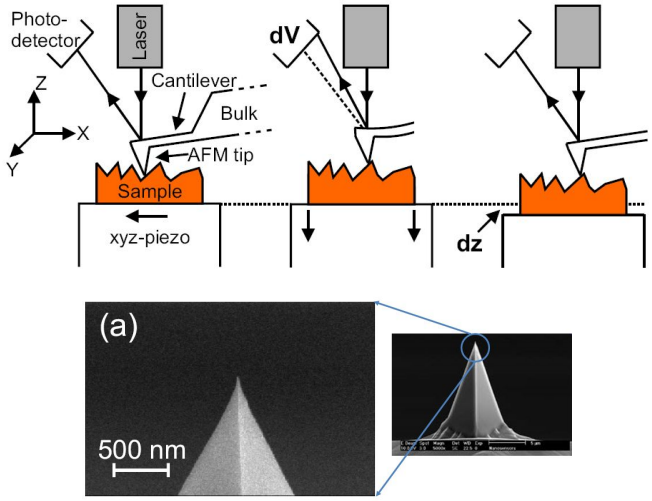

The three essential components are the tip attached to a cantilever, with spring constant k_c a piezoelectric stage with subnanometer positional accuracy and a PID-controller to keep the force constant. The input of the PID controller is the voltage measured due to a reflected laser spot incident on a quadrant-photo detector (QPD). For small extensions, as later for optical tweezers, we can assume that the cantilever behaves as a harmonic spring and thus the force on the surface is given by $F = -k_c x$ where x is the distance of the cantilever from its equilibrium position. The position measurement with a QPD is straightforward and worth to know as it is used in many single-molecule experiments. By comparing the total intensity on the QPD with the intensities on the four quadrants A, B, C, D one can calculate the x and y position of the laser spot on the QPD. Thus it is also easily possible to measure not only forces perpendicular to the sample but also the torsional motion of the cantilever. The spatial resolution of the QPD and thus of the AFM can reach easily below 1 nm.

As the thermal energy equates to 4 pNnm any technique for looking at polymers should be able to reach these forces. The

force resolution obviously depends on k_c. With $k_c = 0.05$ N/m and a QPD resolution of 1 nm we get a force resolution of 50 pN, which is higher than the required resolution of $O(10^{-12}$ N. The minimum force resolution F_{min} can be calculated as

$$F_{min} = \sqrt{\frac{4k_BT}{2\pi}\frac{Bk_c}{f_0Q}}$$

where B is the measurement bandwidth of the QPD, $Q = \frac{2\pi W_0}{\Delta W}$ is the quality factor of the cantilever and f_0 its resonance frequency. f_0 is given by

$$f_0 = \frac{1}{2\pi}\sqrt{\frac{k_c}{m_c}}$$

with m_c the mass of the cantilever. Reducing m_c increases f_0 and thus the force sensitivity.

As an example we can estimate for a typical cantilever stiffness of 0.05 N/m, $f_0 = 10$ kHz and $Q = 2$ in water at room temperature and $B = 20$ kHz, $F_{min} \approx 10^{-12}$ N. Thus the AFM should be useful to study molecular forces as protein unfolding and molecular motors.

The impressive spatial resolution of the AFM on biological are best illustrated by imaging of single protein complexes in aqueous solutions (Engel and Muller, 2000; Mueller and Engel, 2007; Rief et al., 1997). On - atomically -flat- mica surfaces there are impressive examples shown for the example of bacteriorhodopsin at forces around 100 pN. The supported membranes allow for high resolution images even at these high force levels. The illsutration below is taken from (Mueller and Engel, 2007)

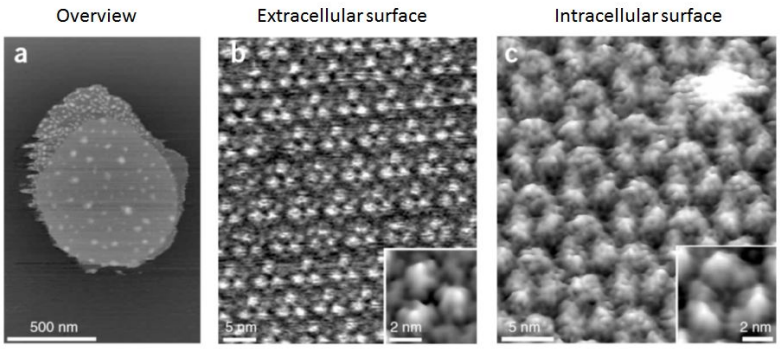

7.3 Optical Tweezers

The ability to mechanically manipulate dielectric particles without any physical contact makes optical tweezers a unique tool in biology, physics and material sciences. Optical tweezers can exert piconewton forces on micrometer-sized objects while measuring the resulting displacements with subnanometer accuracy. Following the pioneering work of Ashkin in the 70s (Ashkin, 1997), optical

trapping is now routinely used to study the mechanical properties of polymers, the physics of colloids and proteins on a single molecule level.

An optical tweezers is established by tightly focusing a laser beam with a high numerical aperture (NA) objective to a diffraction-limited spot, hence providing a steep intensity gradient. For particles with a radius comparable in size to the wavelength of the used trapping laser, quite elaborate electromagnetic theories are needed for an adequate description of the acting optical forces. Still, a complete theory for arbitrarily shaped objects covering all wavelengths does not exist (Neuman and Block, 2004). Unfortunately, in practice most objects considered for trapping belong to this category (0.1λ - 10λ), and so do the colloids used during the experiments described in this master's thesis. However, for the understanding of the basic physical principles the exact mathematical calculations are not needed, and it is more useful to regard the following two limiting cases, which correspond to relatively clear descriptions of the problem.

7.3.1 Ray optics regime for optical trapping

In the ray optics regime, which corresponds to a spherical trapped object that is very large compared to the wavelength ($r \gg \lambda$), optical trapping can be easily understood. In this situation, we can restrict ourselves to simple ray optics, which provides an easy insight in terms of geometrical considerations

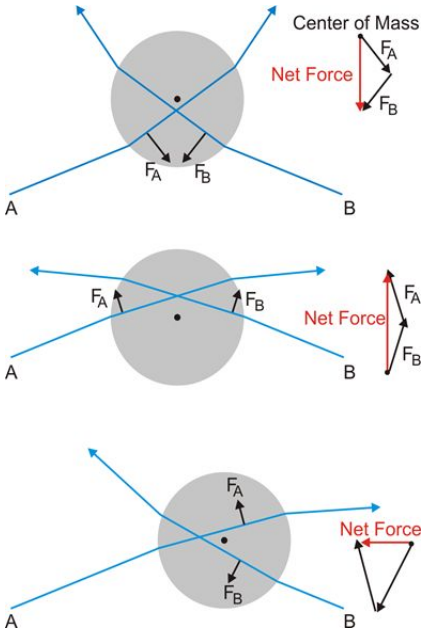

Essentially, as each photon carries a momentum that is proportional to the index of refraction of the medium it travels in, each refraction/reflection event of a light ray at the surface of the dielectric particle causes a momentum change, i.e. a force, always

assuming that absorption effects are not relevant. Summing over all light rays and momenta, we end up with a net force exerted on the particle, as long as it is not situated in its equilibrium position (corresponding to a minimum in the potential energy). With the refractive index of the object being larger than the one of the surrounding medium, e.g. in the case of a polystyrene (PS) bead (n = 1.59) in water (n = 1.33), this force always points towards the trap center. It is also obvious from the figure that - in the ray optics regime - the central beams passing the particle through the center do not contribute to the overall trapping force - however they contribute to the scattering force due to reflections. Thus, for particles which are larger than the wavelength one can realize optical traps also by removing the central part of the beam, essentially creating a donut shaped laser profile as compared to the usual profile assumed for Gaussian beams. This also removes reflections off the particle center and can facilitate on-axis tracking of the particle positions, see e.g. (**?**). Interestingly, the optical traps created with a donut-shaped laser beam are still very well as a harmonic potential - in all three directions.

7.3.2 Rayleigh regime for trapping

If the conditions for Rayleigh scattering are satisfied, i.e. the trapped particle is much smaller than the wavelength ($r \ll \lambda$), it can in first approximation be treated as a Hertzian point dipole in an inhomogeneous electromagnetic field. The resulting overall optical force has to obey the corresponding equations and is conveniently decomposed into two components:

1. the scattering force due to radiation pressure, which is proportional to the intensity of the laser beam and points in its propagation direction, and
2. the gradient force, which is proportional to the intensity gradient and points to the peak of highest intensity, again assuming the herein before mentioned mismatch of refractive indices.

Obviously, it is necessary for stable trapping that the gradient force has to (over-)compensate the scattering force. We discuss the mathematical treatment in more detail in the slides during the lectures.

7.3.3 Calibration of optical tweezers

In order to detect piconewton forces, the position of a trapped particle must be determined with a high temporal and spatial resolution. Traditionally this is done using a quadrant photodiode (QPD) detector (Neuman and Block, 2004), as used for AFM. The techniques discussed in the following can obviously be also used for the calibration of AFM cantilever arms to get quantitative force

measurements. With the help of QPD detectors one can readily achieve nanometer spatial and microsecond temporal resolution, therefore they are a common choice for force measurements with optical tweezers setup. Alternatively, the position of a particle can be tracked with video-based position detection, as we will discuss in the lecture. Employing charged-coupled device (CCD-) or complementary metal oxide semiconductor (CMOS-) cameras (Otto et al., 2008; Otto et al., 2010), video particle tracking is capable of position determination with sub-pixel accuracy. However, video-tracking lack temporal resolution, which is typically in the range of 25120 Hz. Compared to CCDs, CMOS imaging sensors have all the conversion electronics required built into each pixel. Each pixel provides a complete binary value within microseconds, resulting in frame rates of up to 100 kHz (Otto et al., 2008; Otto et al., 2010). The advantage in temporal resolution of the QPD detection compared to video tracking, is directly related to the orders of magnitude lower data bandwidth needed for QPD tracking.

Stokes calibration

So before force measurements can be done, the optical trap needs to be calibrated. There are two straightforward methods for calibration. The drag force method and calibration via analyzing the power spectrum of the Brownian motion of a bead in the trap. The drag force method is based on Stokes law, $F = 6\pi\eta r v$ where F is the viscous force, η is the viscosity of the medium, r the radius of the bead, and v its velocity relative to the surrounding solution. When the stage is moved a trapped colloid will experience a Stokes force and be displaced from its equilibrium position. This leads to a counteracting linear force (according to Hookes law) arising from the harmonic potential at the center of the trap, $F = -k_{trap}x$, where k_{trap} is the force constant or trapping stiffness and x the amplitude of the displacement. In practice, calibration should be done far from any surface as otherwise the Stokes friction coefficient has to be modified. A typical measurement is shown below where a colloid in an optical trap is moved through the solution and the amplitude of the movement is measured (Otto et al., 2008)

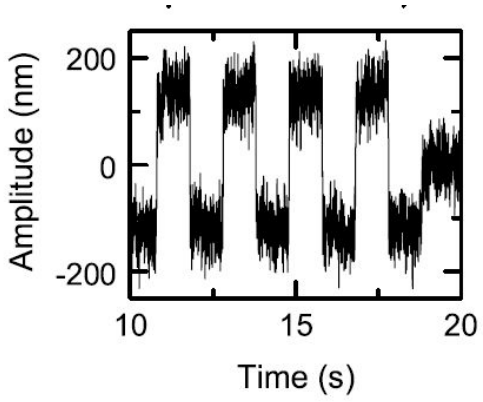

Powerspectrum calibration

For quantitative measurements, accurate calibration of the the optical trap by means of Stokes calibration or - as we discussed in the lectures - detecting the position histogram, can be tedious and contain errors due to drift. Another approach is to change into the frequency domain and thus obtain insight into the relevant processes for a wider range of frequencies (Gittes and Schmidt, 1998). The analysis with the powerspectrum that we will discuss now is used for all the (single-molecule) techniques discussed here and is applicable in almost all measurement systems. A particle has a diffusion coefficient D given by the Stokes-Einstein relation

$$D = \frac{k_B T}{\gamma}$$

where γ denotes its drag coefficient. For a freely diffusiiong particle we the variance Var along the x-axis is

$$Var(x) = \bar{x^2} - \bar{x}^2 = 2Dt$$

In the optical trap we assume that the particle is moving in a harmonic potential with $\phi(x) = \frac{1}{2}\kappa x^2$. We thus know the average position of the partile and assume in the following that $\bar{x}^2 = 0$. As mentioned before, the trap stiffness can be extracted using the equipartition theorem using

$$\langle \frac{1}{2}\kappa x^2 \rangle_t = \frac{1}{2} k_B T$$

which works perfectly fine if we can assume that indeed there is no drift in the system and $\bar{x}^2 = 0$ is valid. However, in almost all real experimental situations this is not the case.

Instead, we can use the Langevin function, where we already assumed that inertia effects can be ignored at our experimental timescales and thus becomes

$$\gamma \frac{dx}{dt} + \kappa x = \xi(t)$$

$\xi(t)$ is an ideal white noise source and by definition $\bar{\xi(t)} = langle\xi(t)\rangle_t = 0$. Although the time average of this function is zero the square is not. Even more importantly for our analysis we will use that

$$|\xi(t)|^2 = S_\xi(f) = 4\gamma k_B T$$

, where $\xi(f)$ is the Fourier transform of $\xi(t)$. In the following we will us only with the frequency and not with the angular frequency $2\pi f$ avoiding prefactors.

We can now define the Fourier transform of our position signal of the particle $x(t)$

$$x(t) = \int_{-\infty}^{+\infty} x(f) \exp(-i2\pi f t) df$$

and thus get that

$$\frac{dx(t)}{dt} = -i2\pi x(f)$$

We can now write down the Langevin euqation for our system in the frequency domain

$$2\pi\gamma(f_c - if)(x(f) = \xi(f)$$

where we introduce the characteritic frequency of the trap as $f_c = \frac{kappa}{2\pi gamma}$. Since, by definition, this equation has to be zero we have to get $S_\xi(f)$ on the RHS and thus

$$4\pi^2\gamma^2(f_c^2 + f^2)|x^2(f)| = S_\xi(f) = 4\gamma k_B T$$

which describes the powerspectrum of the position fluctuations in the frequency domain $S_x(f) = |x^2(f)|$. Thus it follows

$$S_x(f) = \frac{k_B T}{\gamma\pi^2(f_c^2 + f^2)}$$

. In all this discussion we assume that the infinite integrals are indeed converging to finite values. In a themal process, where we know from statistical physics that the value of $S_\xi(f) = 4\gamma k_B T$ this is obviously the case. For real data, one can deal with these issues by windowing (see below). Clearly for $f \gg f_c$ we expect the curve do drop with a slope of 2 in a log-log plot while for $f_c \gg f$ we would expect a plateau in the powerspectrum. Any deviation from this indicates limitations in the measurement process, interference from outside or other problems like non-spherical particles.

A typical trace as a function of time with the corresponding powerspectrum is shown below. The fit takes only frequencies into account that are larger than the boundary for the 1/f noise and stops at high frequencies before the filter cutoff.

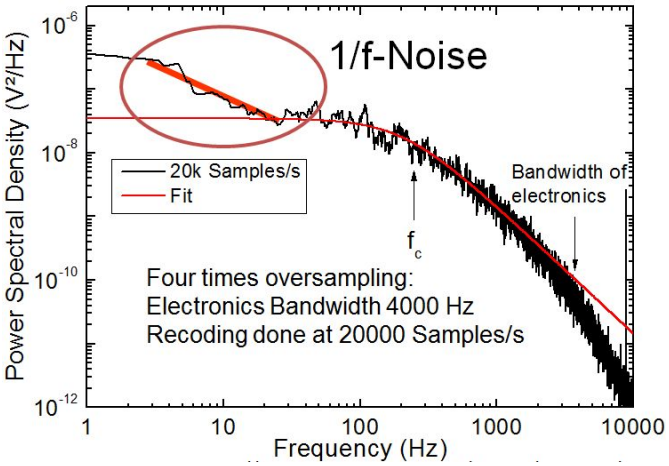

7.3.4 Background on Fourier transforms

Observing the dynamics of single molecules means dealing with time-domain data, e.g. varying voltage signals from a photo detector, corresponding to singular events. Still, as we want to interpret continuous phenomena, like the thermal random noise of our system, we have to go over to the frequency domain. Departing from a set of N discrete data points x_N (positions in one dimension e.g. x) separated by time intervals Δt, one has to perform a discrete Fourier transform (FT). This leads to a set of N complex Fourier components of the form

$$X(f_m) := FTxn = \sum_{n=1} Nx_n exp(-2\pi imn/n)$$

with $f_m = m\delta f$ the m-th frequency with $-N/2 \leq m \leq n/2$ and $\delta = 1/N\delta tf$ the minimum detectable frequency. $\phi_{mn} = -2\pi mn/N$ being the phases of the complex summands. Computing the power spectrum or power spectral density PSD, $S(f_m)$ just means calculating the squared absolute value of the Fourier transform, such that up to normalizing prefactors we have:

$$S(_f m) \propto |X(_f m)|^2$$

This way the phase information is lost, but one obtains again an analyzable set of real numbers. You can interpret this step as passing your time-dependent signal trough a set of band filters and plotting the intensities vs. the center frequencies of these filters. Averaging over many data sets yields the exact spectral characteristics of the process under consideration.

When speaking about a Fourier transform, one should keep in mind that in practice, especially for large data sets, the calculation is usually done by means of a fast Fourier transform (FFT) algorithm. Such an algorithm needs only $O(N \log N)$ operations to calculate the result, whereas evaluating the above sum directly

takes $O(N^2)$ steps. A more detailed - and very useful practical discussion - on FFT can be found in the book 'Numerical recipes in C' (**?**). There you find also a discussion about the issues concerning how to ensure that the FFT is converging. However, we will assumed throughout our discussions here that we are only dealing with finite FFTs. Another issue of real data is that the signals are strictly speaking never truly periodic as the measurement time is limited. This is usually dealt with by windowing functions, which decrease the signal amplitude when approaching the edges of the observation times. Again, a detailed discussion about these issues are beyond the scope here and can be found in the literature (**?**).

7.3.5 Aliasing and other limitations

Two concepts have to be remembered when interpreting a power spectrum:

- Windowing: for a FT one assumes a periodic wrapping of the data points ($x_{N+1} \equiv x1$ implicitly), which may lead to discontinuities and phase shifts when the transform is applied to a finite time interval T. This can cause peak broadenings and other artifacts in the power spectrum. The problem can be overcome by multiplying the data set with a so-called window function, which forces the amplitudes to be zero at both ends of the chosen interval.
- Aliasing (aka 'backfolding') occurs when contributions in the power spectrum of frequencies higher than the so-called Nyquist frequency $f_{Nyq} = 1/2\delta t$ are folded back and added to lower frequency regions. The threshold is defined by the highest frequency unambiguously measurable in the data set and is equal to half the sampling frequency. This effect can be avoided by applying a low-pass filter to the signal BEFORE digital sampling occurs.

An example of the time dependent position signal of a colloidal particle in an optical trap, measured with 20, 4 and 0.6 kilosamples per second, respectively. (b) The corresponding power spectra reveal that aliasing effects (described in the text) become more pronounced for smaller sampling (or Nyquist) frequencies. Therefore, the sampling rate should always be chosen sufficiently large for the corresponding experiment. The drop at ∼5 kHz is due to the limited bandwidth (BW) of the electronics.

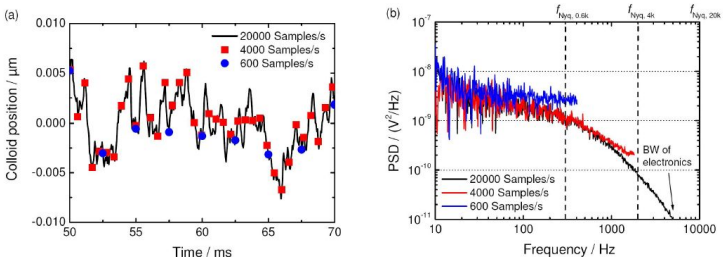

7.4 Magnetic Tweezers

When forces of lower than one pN or even 10^{-15} N have to be detected, magnetic tweezers are the method that should be used (Gosse and Croquette, 2002; Allemand et al., 1998). The usable range of AFM, optical tweezers and magnetic tweezers is covering nN- tens of pN, 100 pN - around 1 pN and 10s of pN to fN range, respectively. Another advantage of magnetic tweezers, which will be explained in the following discussion, is that they can used to apply a constant force. This can be crucial in simulating a constant load on a molecular motor working in a cellular environment. In addition, they can be used to twist polymers and study their rotational stiffness as well. This is almost impossible for AFM and very difficult to achieve with optical tweezers.

Magnetic tweezers are the most simple of the setups that we discussed so far. They do not allow for three-dimensional spatial control as AFM and optical tweezers, insofar is the tweezers perhaps somewhat misleading. In the end one uses two permanent magnets which are mounted on a rotatable stage. If they are mounted close together there will be a gradient in the magnetic field lines between the north and south poles as shown below (**?**)

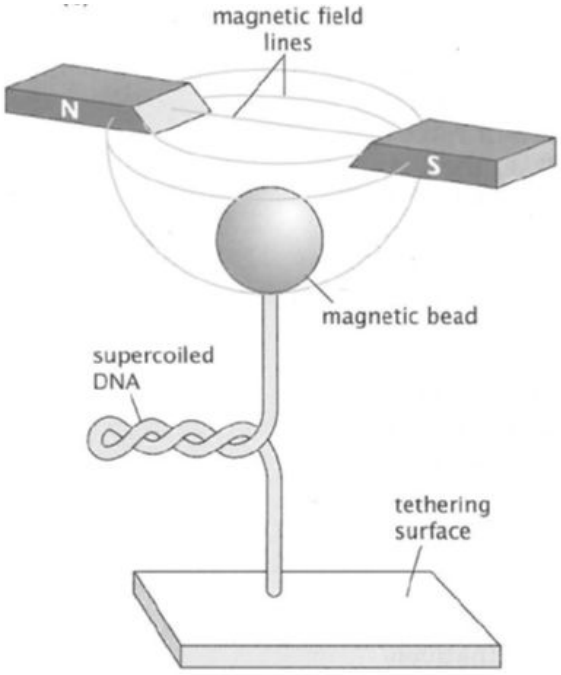

The key components for magnetic tweezers are the magnets - which are usually permanent magnets although electro-magnets can also be employed. The colloidal particle (with diameters of several micrometers) which transmits the force on the (DNA) molecule contains ferromagnetic nanoparticles with typical diameters of less than 50 nm. The nanoparticles are randomly distributed in the larger particle and each of them is superparamagnetic. This

means that the nanoparticles have a preferred direction for their magnetic moments m_i even above the Curie temperature. Each superparamagnetic particle has its own magnetization axis with magnetic moment m_i - however, overall the large colloidal particle will have an overall net magnetic moment (Crut et al., 2007).

Each nanoparticle will feel a force F_i in the gradient of the magnetic field $\underline{B}$

$$\underline{F}_i = (m_i \cdot \nabla)\underline{B}$$

Since we are at finite temperatures there will be some fluctuations of the dipole moment, and thus the time-averaged force is given by

$$\langle \underline{F}_i \rangle = m_i \langle \cos(\theta) \rangle B,$$

where θ describes the angle between the magnetic moment and the electric field. Assuming that this is a temperature activated process we can use a Boltzmann factor $m_i B/k_B T$ and thus show that

$$\langle \underline{F}_i \rangle = m_i \left(\coth(m_i B/k_B T) - \frac{k_B T}{m_i B} \right) \nabla B.$$

The force F on the large colloid can be calculated by summing/averaging the force on all the i smaller nanoparticles:

$$\langle F \rangle = \sum_i \left(\coth(m_i B/k_B T) - \frac{k_B T}{m_i B} \right) \nabla B = m(B) \nabla B,$$

where $m(B)$ is the field-dependent magnetic moment of the large colloidal particle. If $m(B)$ is known one could calculate the force on the particle by measuring the magnetic field gradient with a small Hall-probe at various positions from the permanent magnets.

Bibliography

Allemand, J. F., Bensimon, D., Lavery, R., and Croquette, V. (1998). Stretched and overwound DNA forms a Pauling-like structure with exposed bases. *Proc. National Acad. Sciences United States Am.*, **95**(24), 14152–14157.

Ashkin, A. (1970). Acceleration and trapping of particles by radiation pressure. *Phys. Rev. Lett.*, **24**(4), 156–159.

Ashkin, A. (1997). Optical trapping and manipulation of neutral particles using lasers. *Proc. National Acad. Sciences United States Am.*, **94**(10), 4853–4860.

Bezrukov, S. M. (2000). Ion channels as molecular coulter counters to probe metabolite transport. *J. Membr. Biology*, **174**(1), 1–13.

Bustamante, C., Bryant, Z., and Smith, S. B. (2003). Ten years of tension: single-molecule DNA mechanics. *Nature*, **421**(6921), 423–427.

Bustamante, C. and Rivetti, C. (1996). Visualizing protein-nucleic acid interactions on a large scale with the scanning force microscope. *Ann. Rev. Biophys. Biomolecular Struct.*, **25**, 395–429.

Crut, A., Koster, D. A., Seidel, R., Wiggins, C. H., and Dekker, N. H. (2007). Fast dynamics of supercoiled DNA revealed by single-molecule experiments. *Proc. National Acad. Sciences United States Am.*, **104**(29), 11957–11962.

Dekker, C. (2007). Solid-state nanopores. *Nature Nanotechnology*, **2**(4), 209–215.

Delgado, A. V. ., Gonzalez-Caballero, F., Hunter, R. J., Koopal, L. K., and Lyklema, J. (2007). Measurement and interpretation of electrokinetic phenomena. *J. Colloid Interface Science*, **309**(2), 194–224.

Engel, A. and Muller, D. J. (2000). Observing single biomolecules at work with the atomic force microscope. *Nature Struct. Biol.*, **7**(9), 715–718.

Garaj, S., Hubbard, W., Reina, A., Kong, J., Branton, D., and Golovchenko, J. A. (2010). Graphene as a subnanometre trans-electrode membrane. *Nature*, **467**(7312), 190–U73.

Gittes, F. and Schmidt, C. F. (1998). Signals and noise in micromechanical measurements. *Methods In Cell Biology, Vol 55*, **55**, 129–156.

Gosse, C. and Croquette, V. (2002). Magnetic tweezers: Micromanipulation and force measurement at the molecular level. *Biophys. J.*, **82**(6), 3314–3329.

Hall, J. E. (1975). Access resistance of a small circular pore. *J. General Physiology*, **66**(4), 531–532.

Hamann, C. H. and Vielstich, W. (2005). *Elektrochemie*. Wiley-VCH.

Holstein, B. (2001). The van der Waals interaction. *American Journal of Physics*, **69**, 441.

Kasianowicz, J. J., Brandin, E., Branton, D., and Deamer, D. W. (1996). Characterization of individual polynucleotide molecules using a membrane channel. *Proc. National Acad. Sciences United States Am.*, **93**(24), 13770–13773.

Keyser, U. F., van Dorp, S., and Lemay, S. G. (2010). Tether forces in DNA electrophoresis. *Chem. Soc. Rev.*, **39**(3), 939–947.

Lee, K., McCormick, W., Ouyang, Q., and Swinney, H. (1993). Pattern formation by interacting chemical fronts. *Science*, **261**(5118), 192–194.

Manning, G. (1969). Limiting laws and counterion condensation in polyelectrolyte solutions I. Colligative properties. *The Journal of Chemical Physics*, **51**, 924.

Mueller, D. J. and Engel, A. (2007). Atomic force microscopy and spectroscopy of native membrane proteins. *Nature Protocols*, **2**(9), 2191–2197.

Neuman, K. C. and Block, S. M. (2004). Optical trapping. *Rev. Scientific Instruments*, **75**(9), 2787–2809.

Otto, O., Czerwinski, F., Gornall, J. L., Stober, G., Oddershede, L. B., Seidel, R., and Keyser, U. F. (2010). Real-time particle tracking at 10,000 fps using optical fiber illumination. *Optics Express*, **18**(22), 22722–22733.

Otto, O., Gutsche, C., Kremer, F., and Keyser, U. F. . (2008). Optical tweezers with 2.5 kHz bandwidth video detection for single-colloid electrophoresis. *Rev. Scientific Instruments*, **79**(2), 023710.

Rief, M., Gautel, M., Oesterhelt, F., Fernandez, J. M., and Gaub, H. E. (1997). Reversible unfolding of individual titin immunoglobulin domains by afm. *Science*, **276**(5315), 1109–1112.

Semenov, I., Otto, O., Stober, G., Papadopoulos, P., Keyser, U. F., and Kremer, F. (2009). Single colloid electrophoresis. *J. Colloid Interface Science*, **337**(1), 260–264.

Turing, A. (1990). The chemical basis of morphogenesis. *Bulletin of Mathematical Biology*, **52**(1), 153–197.

Viovy, J. L. (2000). Electrophoresis of DNA and other polyelectrolytes: Physical mechanisms. *Rev. Modern Phys.*, **72**(3), 813–872.

Winterhalter, M. and Helfrich, W. (1988). Effect of surface charge on the curvature elasticity of membranes. *The Journal of Physical Chemistry*, **92**(24), 6865–6867.

Zimm, B. H. and Levene, S. D. (1992). Problems and prospects in the theory of gel-electrophoresis of dna. *Quarterly Rev. Biophys.*, **25**(2), 171–204.